Search for the Decay $B_s^0 \to J/\psi\pi^0$ at Belle Experiment

A thesis submitted for the degree of

Doctor of Philosophy

by

Devender Kumar

under the supervision of

Prof. Bipul Bhuyan

Department of Physics
Indian Institute of Technology Guwahati
Guwahati - 781039, Assam, India

This thesis is dedicated to
my beloved "Maa" and "Papa",
"Nani-Nana" and "Mami-Mama",
"teachers" that shaped me,
and the one—Buddha.

Declaration

Devender Kumar
Roll No. 176121010
Department of Physics
Indian Institute of Technology Guwahati
Guwahati, India
email: deven176121010@iitg.ac.in

I hereby declare that works presented in the thesis entitled **"Search for the Decay $B_s^0 \to J/\psi\pi^0$ at Belle Experiment"** have been carried out by me under the supervision of **Prof. Bipul Bhuyan** at the Department of Physics, Indian Institute of Technology Guwahati, India. The thesis has not been submitted anywhere else for any degree. Works presented in the thesis are all my own unless referenced to the contrary in the thesis.

Devender Kumar

Date: September 14, 2023. Signature

Certificate

Prof. Bipul Bhuyan
Department of Physics
Indian Institute of Technology Guwahati
Guwahati, India
email: bhuyan@iitg.ac.in

This is certified that the work contained in the thesis entitled **"Search for the Decay $B_s^0 \to J/\psi\pi^0$ at Belle Experiment"** by Mr. Devender Kumar (Roll No 176121010), a Ph.D. student in the Department of Physics, Indian Institute of Technology Guwahati, is carried out under my guidance. The results demonstrated in this thesis have not been submitted to any other Institute or University for the award of any other degree or diploma.

Bipul Bhuyan

Date: September 14, 2023. Signature

Acknowledgement

I would like to thank every individual who has played a role, directly or indirectly, in supporting and guiding me during my thesis work. I sincerely apologize in advance if I unintentionally omit any names; your contributions have been invaluable to me and are deeply appreciated.

Foremost, I am grateful to Prof. Bipul Bhuyan for accepting me as his Ph.D. student and introducing me to this unique field of experimental high-energy physics. Prof. Bipul Bhuyan has provided me with a conducive and supportive work environment and always given me room to think freely. I am thankful for his constant guidance, patience, and expertise throughout this course. The mentorship of Prof. Bipul Bhuyan has been phenomenal in shaping the direction of research work and the overall quality of this thesis.

I am thankful to my Ph.D. doctoral committee members, Dr. Udit Raha, Dr. Meduri C Kumar, and Dr. Sovan Chakraborty, for giving their valuable time towards the completion of my academic responsibilities.

I wish to express my heartfelt gratitude to the conveners of the Upsilon(5S) group, Dr. Roman Mizuke and Prof. Kinoshita Kay, for their unwavering support through their valuable suggestions and comments, which have played an instrumental role in making this analysis feasible. I am sincerely grateful to the esteemed members of the review committee at Belle, namely Prof. Chunhui Chen (chairperson), Prof. Martin Sevior, and Dr. Vipin Gaur, for their diligent review of the analysis and publication draft, along with their provision of the invaluable insights, suggestions, and comments. Further, I thank Prof. Gagan Mohanty, Prof. Jim Libby, Prof. Karim Trabelsi, and Dr. Vishal Bhardwaj for their valuable time and comments at the Belle Analysis Workshops and on several other occasions. I am grateful to the Belle Collaboration for providing the platform and every utility needed to complete this analysis.

I thank the University Grant Commission (UGC) for funding my research. This funding has eased the financial burden of pursuing higher education and allowed me to focus on my research wholeheartedly, knowing that I have the necessary resources

to carry out my studies effectively.

I am heartfelt grateful to my beloved parents, grandparents (nana-nani), maternal uncle-aunt, and every cherished family member, whose unwavering support has been the bedrock of my life journey. Their firm encouragement and unconditional love supporting every choice have been the seed of my happiness and the driving force behind my determination to keep moving forward.

I am grateful to my friends Sunderdeep, Ravi, Ojasvi, Vandana, Devabrat, and Subrat for their compassionate and blissful presence, cherishing with me every moment however they have come. I extend my gratitude to my colleagues and friends, to Dr. Atanu Nath, Dr. Nitin Yadav, Dr. Deepanjali Goswami, Dr. Kamal Jyoti Nath, Maharnab Bhattacharjee, Dibyajyoti Kalita, Dr. Jyotirmoi Borah, Shubhangi Krishan Maurya, Shivam, Shailesh Pincha, Arkodip Biswas, and Rajesh Pramanik for creating the delightful and conducive environment in the working lab and the surroundings. I cannot thank Dr. Charudatt Y Kadolkar enough for his badminton teaching and life in general, whose affection has been bliss, and his encouragement has been nothing less than fuel in every situation. I am grateful to my badminton champs, Jegyasu, Kelly, Juhi, Prajna, Akanshu, Anterdipan, Rahul, Somnath, and Himanshu, a booster of the delightful morning.

I am thankful to my batchmates for their joyful companionship and to every holy soul whose mere greeting has brought a smile and peace to my body and mind.

I am grateful to the enlightened one, Budhha, who showed the importance of compassion, mindfulness, and inner peace, and to mystic poet-saint Kabir. This acknowledgement would only be complete by thanking nature for its every resource to have a life and the teaching of flow, kindness, and harmony.

List of Publications

Publication from thesis

- Search for the decay $B_s^0 \to J/\psi\pi^0$ at Belle Experiment, D. Kumar, B. Bhuyan *et al.* (Belle Collaboration), Phys. Rev. D 109, 032007 (2024).
- Search for the decay $B_s^0 \to J/\psi\pi^0$ at $\Upsilon(5S)$ resonance, D. Kumar, B. Bhuyan, conference proceeding paper under review to be published in Springer Nature.
- Search for the decay $B_s^0 \to J/\psi\pi^0$ at $\Upsilon(5S)$ resonance using Belle detector, D. Kumar, B. Bhuyan, the Belle internal note 1643, Version 8.

Other publication

- Performance of the CDC in data collected before LS1, Devender Kumar with CDC group of the Belle II collaboration, the Belle II internal note.

Further publications can be accessed through the link iNSPIRE-HEP.

Abstract

We report the first search for the decay $B_s^0 \to J/\psi\pi^0$ using 121.4 fb^{-1} of data collected at $\Upsilon(5S)$ resonance state by the Belle detector at the KEKB asymmetric energy e^+e^- collider located at the High Energy Accelerator Research Organisation, Japan. We observe no signal and report an upper limit on the branching fraction, $\mathcal{B}(B_s^0 \to J/\psi\pi^0)$ of 1.21×10^{-5} at 90% confidence level. This result is the most stringent, improving the previous bound by two orders of magnitude.

Preface

What do you see at dawn?
A colorful sky and many a star
Reflection of light in water from the far
The trees and ripples in the water
And, so, a breezy air.

One can sit and think.
What are they made of?
Is it really as different as it seems
Or many amazing arrangements
Of a few fundamental blocks?

Devender Kumar

The matter around us comprises of fundamental particles held together by elemental forces. The dynamics of these particles are best understood within the theoretical framework known as the Standard Model (SM), which has been tremendously successful in explaining the thousands of experimental observations. Despite the success, the SM has limitations such as the non-zero mass of the neutrinos as predicted from the neutrino flavor oscillations, the matter and anti-matter asymmetry of the universe, the existence of dark matter and its interactions are the physics beyond SM, etc. Further, the SM is consistently tested at two frontiers: The high-energy and low-energy high-luminosity colliders. The Large Hadron Collider (LHC) experiments (LHCb, CMS, ATLAS, etc.) at CERN are examples of the first kind, whereas the Belle and its successor Belle II, BABAR, etc., are examples of the second kind. The high luminosity experiments enable physicists to accurately measure the SM parameters and the branching fractions of heavy meson's rare decay. The deviation of the experimental observation from theoretical prediction can hint at the new

physics. The decay $B_s^0 \to J/\psi\pi^0$ is rare within the SM. This thesis presents the result of the search for the decay $B_s^0 \to J/\psi\pi^0$ at Belle experiment with the content being organized in the chapters as follows:

Chapter 1 introduces the SM of particle physics, a theoretical framework governing the electroweak and strong interactions of fundamental particles through the exchange of gauge bosons. We discuss the gauge representation of the fermions and scalars, the Lagrangian symmetries as understood today, and the spontaneous symmetry-breaking pattern. We write the most general renormalizable Lagrangian and emphasize its kinetic and Yukawa parts, as they involve gauge interactions and the flavor-changing currents of the quarks and leptons. We elaborate on the mathematical origin of the Cabibbo-Kobayashi-Maskawa (CKM) matrix, responsible for the flavor physics in the quark sector, and its most convenient Wolfenstein parameterization. We also briefly overview the existing approaches that deal with the complexity of computing the hadronic contributions. We conclude the chapter emphasizing the significance of the decay $B_s^0 \to J/\psi\pi^0$ in advancing our understanding of heavy B physics.

Chapter 2 provides an overview of the KEKB accelerator, an asymmetric electron-positron beam collider, the Belle detector, the Belle trigger and data acquisition system, and the Belle analysis framework. We also discuss the physics of $B_s^0\bar{B}_s^0$ production at $\Upsilon(5S)$ resonance.

Chapter 3 discusses the selection criteria for signal $B_s^0 \to J/\psi\pi^0$ events based on the Monte Carlo (MC) simulated data, where J/ψ and π^0 are reconstructed from the lepton (e^+e^- and $\mu^+\mu^-$) and two-photon channels, respectively. We also determine the signal selection efficiency of the algorithm. A random combination of leptons and photons from the background events (e^+e^- cascade that is not the $B_s^0 \to J/\psi\pi^0$) can satisfy the selection criteria. Therefore, a pre-identification of the possible background is discussed in detail based on the MC simulated data.

Chapter 4 discusses the parameterization of the selected candidate distributions from the MC simulated signal and background events data separately. The distributions are fitted using the extended maximum likelihood method. Further, we present the control sample results demonstrating the simulated and collision data agreement and validating the event selection criterion. Followed by this, we illustrate the fitter stability and estimate the fit bias based on the MC toy data. Finally, we present the results from the data at $\Upsilon(5S)$ resonance.

Chaper 5 presents the various sources of systematic uncertainties in detail and categorizes them based on their nature of additive and multiplicative uncertainties. We assign a total systematic uncertainty for each kind.

Chaper 6 reports the first search for the decay $B_s^0 \to J/\psi\pi^0$ at Belle experiment using an entire dataset accumulated at $\Upsilon(5S)$ resonance. This chapter concludes with a brief discussion of the possible implication of the result and further improvement in the near future.

Contents

List of Figures

List of Tables

Chapter 1

Theoretical Framework and the Motivation

1.1 Introduction

This chapter introduces the Standard Model (SM) of particle physics, a theoretical framework governing the electroweak and strong interactions of fundamental particles through the exchange of gauge bosons. We discuss the gauge representation of the fermions and scalars, the Lagrangian symmetries as understood today, and the spontaneous symmetry-breaking pattern. We write the most general renormalizable Lagrangian and emphasize its kinetic and Yukawa parts, as they involve gauge interactions and the flavor-changing currents of the quarks and leptons. We elaborate on the mathematical origin of the Cabibbo-Kobayashi-Maskawa (CKM) matrix, responsible for the flavor physics in the quark sector, and its most convenient Wolfenstein parameterization. Further, we provide an overview of the B-physics and the significance of the decay $B_s^0 \to J/\psi\pi^0$.

1.2 The Fundamental Blocks

To our best knowledge, the matter around us comprises of the spin-$\frac{1}{2}$ fermions at the elementary level. In the SM, the fermions are divided into two sectors, the leptons and the quarks, each with six types, also called the 'flavors'. Further, the leptons and quarks come into three generations. The first generation includes the electron (e) and electron-neutrino (ν_e), a lepton pair, and up (u) and down (d) quarks, forming a quark pair. The second and third generations include the muon (μ) and muon-neutrino (ν_μ), tau (τ) and tau-neutrino (ν_τ) in the lepton sector, whereas the charm (c) and strange (s), top (t) and bottom (b) in the quark sector, respectively. The first generation is the most stable one forming the visible universe around us, followed by the second and third generations. The SM describes the interaction of the fundamental particles via the exchange of gauge bosons, namely the photon (γ), $W^\pm$, Z, and gluons (g). All the particles, except for the neutrinos, γ, and g,

acquire masses under spontaneous symmetry breaking of SM Higgs (H) field. The SM particles are listed in Figure 1.1.

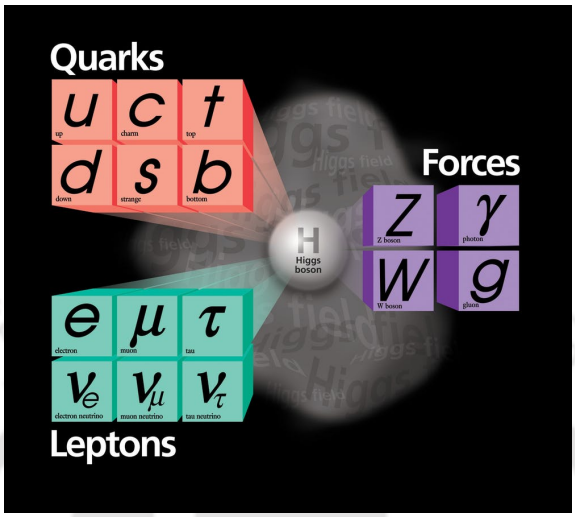

Figure 1.1: The Standard Model particles.

Except for neutrinos, all the fermions are charged particles. Leptons carry a charge of -1 unit of the magnitude of electron (e) charge, while quarks have the fractional charge Qe with Q equal to $+\frac{2}{3}$ for up-type quarks and $-\frac{1}{3}$ for down-type quarks. Because of the electric charge, the fermions interact via photon mediators, and the processes are studied under quantum electrodynamics (QED). In addition to the charge Q, quarks have an additional color charge responsible for the strong interactions. The color exchange among the quarks carried by the gluons is governed by quantum chromodynamics (QCD). The heavy quarks and leptons are unstable, decaying into the light fermions by changing the flavors through weak interactions. In the SM, the flavor changing processes are governed by the $W^{\pm}$ mediators. The Z boson is also a weak force carrier due to its heavy mass but does not change the flavors.

1.3 Theoretical Framework

Let us consider a fermion field ψ decomposed in the left-handed and right-handed chiral states as

$$\begin{aligned} \psi &= \psi_L + \psi_R, \\ &= \hat{P}_L\psi + \hat{P}_R\psi, \end{aligned} \tag{1.1}$$

where $\hat{P}_L = \frac{1}{2}(1-\gamma^5)$ and $\hat{P}_R = \frac{1}{2}(1+\gamma^5)$ are the projection operators, γ^5 is defined as $i\gamma^0\gamma^1\gamma^2\gamma^3$, and $\gamma \in \{\gamma^0, \gamma^1, \gamma^2, \gamma^3\}$ are the four Dirac (γ) matrices. Using the properties of the γ matrices [3], it can be shown that the projection operators satisfy the following relations,

$$\hat{P}_L^2 = \hat{P}_L, \qquad \hat{P}_L^\dagger = \hat{P}_L, \qquad \hat{P}_L\gamma^\mu = \gamma^\mu\hat{P}_R, \tag{1.2}$$

and the same for $\hat{P}_R$ by inter-converting the $L \leftrightarrow R$. The SM Lagrangian governing the dynamics of the fields associated with the elementary particles has embedded local gauge symmetry of $SU(3)_C \times SU(2)_L \times U(1)_Y$, where the subscripts C, L, and Y represent the gauge transformations corresponding to the color mixing of the quarks, left-handed chiral nature of the flavor-changing weak interactions, and weak hypercharge unifying the electromagnetic and the weak interactions in the electroweak model of Glashow-Salam-Weinberg (GSW), respectively [3, 4]. The SM gauge representation of the fermionic fields is given as

$$\begin{aligned}
Q_L(3,2)_{+1/3} &\in \left\{ \begin{pmatrix} u'_L \\ d'_L \end{pmatrix}, \begin{pmatrix} c'_L \\ s'_L \end{pmatrix}, \begin{pmatrix} t'_L \\ b'_L \end{pmatrix} \right\}, \\
U_R(3,1)_{+4/3} &\in \{u'_R, c'_R, t'_R\}, \\
D_R(3,1)_{-2/3} &\in \{d'_R, s'_R, b'_R\}, \\
L_L(1,2)_{-1} &\in \left\{ \begin{pmatrix} \nu_{e_L} \\ e^-_L \end{pmatrix}, \begin{pmatrix} \nu_{\mu_L} \\ \mu^-_L \end{pmatrix}, \begin{pmatrix} \nu_{\tau_L} \\ \tau^-_L \end{pmatrix} \right\}, \\
E_R(1,1)_{-2} &\in \left\{ e^-_R, \mu^-_R, \tau^-_R \right\},
\end{aligned} \tag{1.3}$$

where the subscripts L and R represent the left-handed and right-handed chiral states of the fermions, and the first and second arguments in the parentheses correspond to the gauge transformation properties of the fields under $SU(3)$ and $SU(2)$, respectively. The left-handed quark and lepton doublets construct a weak isospin space so that the upper and lower members of the doublets have a total weak isospin ($I_{\rm W}$) of 1/2 with the third components ($I^{(3)}_{\rm W}$) of the weak isospin being $+1/2$ and $-1/2$, respectively. $I_{\rm W}$ follows the algebra similar to the spin-1/2 angular momentum. The parenthesis subscripts are the quantum numbers associated with the weak hypercharge identified as $Y = 2(Q_{\rm EM} - I^{(3)}_{\rm W})$ in the electroweak model of GSW, where $Q_{\rm EM}$ is the quantum number associated with the electromagnetic charge of the fields. The factor of two for Y is purely conventional. The only scalar field in the SM is represented as

$$\phi(1,2)_{+1} = \frac{1}{\sqrt{2}} \begin{pmatrix} \phi^+ \\ \phi^0 \end{pmatrix}, \tag{1.4}$$

where ϕ^+ and ϕ^0 are the complex scalar field components of the Higgs doublet.

The Lagrangian (referring to Lagrangian density throughout this thesis) for a massless Dirac fermion $\psi(x)$ is given by

$$\mathcal{L} = i\bar{\psi}\gamma^\mu \partial_\mu \psi, \tag{1.5}$$

where $\bar{\psi}$ is the adjoint spinor defined as $\psi^\dagger\gamma^0$, and x is the space-time four-vector. Under the local $U(1)_Y$ gauge transformation of the field,

$$\psi \rightarrow \psi' = e^{ig'\frac{\hat{Y}}{2}\xi(x)}\psi, \tag{1.6}$$

the $\mathcal{L}$ is not invariant as additional term of $-g'\frac{\hat{Y}}{2}\bar{\psi}\gamma^\mu(\partial_\mu\xi)\psi$ appears upon substitution of the transformed field in equation 1.5, where g' and $\xi(x)$ are the dimensionless

parameters determining the coupling strength of the new gauge field and the local phase of the $U(1)_Y$ gauge transformation, respectively. The weak hypercharge $\hat{Y}$ is the generator of local $U(1)_Y$ gauge transformation and considers the quantum numbers determined from the electroweak model. The invariance of $\mathcal{L}$ under local gauge transformation can be preserved by replacing the ∂_μ with covariant derivative defined as

$$D_\mu = \partial_\mu + ig'\frac{\hat{Y}}{2}B_\mu, \tag{1.7}$$

given that the new gauge boson B_μ transform as

$$B_\mu \to B'_\mu = B_\mu - \partial_\mu \xi. \tag{1.8}$$

Thus, the imposition of the $U(1)_Y$ symmetry on $\mathcal{L}$ requires an additional gauge field B_μ, as a consequence of which the free field ψ has an interaction term of $-g'\frac{\hat{Y}}{2}\bar{\psi}\gamma^\mu B_\mu\psi$ in the Lagrangian. The weak and strong interactions are associated with the invariance of the Lagrangian under $SU(2)$ and $SU(3)$ local gauge transformations, given respectively as

$$\varphi \to \varphi' = e^{ig\boldsymbol{\alpha}(\boldsymbol{x}).\hat{\boldsymbol{T}}}\varphi, \tag{1.9}$$

$$\Phi \to \Phi' = e^{ig_s\boldsymbol{\beta}(\boldsymbol{x}).\hat{\boldsymbol{L}}}\Phi, \tag{1.10}$$

where $\boldsymbol{\alpha} = \{\alpha_i\}$ and $\boldsymbol{\beta} = \{\beta_j\}$ are the local phases, $\hat{\boldsymbol{T}} = \{\frac{\sigma_i}{2}\}$ are three generators of the $SU(2)$ group, $\hat{\boldsymbol{L}} = \{\frac{\lambda_i}{2}\}$ are eight generators of the $SU(3)$ group, g and g_s are the corresponding dimensionless coupling parameters similar to the $U(1)_Y$ transformation, φ is the doublet representation of the fields given in equations 1.3 and 1.4, and Φ is a column vector with elements corresponding to three color wave-functions of the quarks. σ_i and λ_j are the Pauli and Gell-Mann matrices [3]. Following the mechanism developed for the $U(1)_Y$ local gauge transformation, the covariant derivative (equation 1.7) is redefined as

$$D^\mu = \partial^\mu + ig'\frac{\hat{Y}}{2}B^\mu + ig\boldsymbol{W}^\mu.\hat{\boldsymbol{T}} + ig_s\boldsymbol{G}^\mu.\hat{\boldsymbol{L}}, \tag{1.11}$$

where $\boldsymbol{W}^\mu = \{W_1^\mu, W_2^\mu, W_3^\mu\}$ and $\boldsymbol{G}^\mu = \{G_1^\mu, \ldots, G_8^\mu\}$ are the spin-1 gauge fields corresponding to the generators of $SU(2)$ and $SU(3)$ gauge symmetries. The gauge invariance can be restored if the gauge fields transform as

$$W_k^\mu \to W_k'^\mu = W_k^\mu - \partial^\mu\alpha_k - g\epsilon_{ijk}\alpha_i W_j^\mu, \tag{1.12}$$

$$G_k^\mu \to G_k'^\mu = G_k^\mu - \partial^\mu\beta_k - gf_{ijk}\beta_i G_j^\mu, \tag{1.13}$$

where ϵ_{ijk} (Levi-Civita indices) and f_{ijk} are the structure constants inferring the non-abelian nature of the $SU(2)$ and $SU(3)$ groups, and indices i and j are summed over the corresponding gauge fields. The field strength tensors associated with the gauge bosons B^μ, W_i^μ, and G_j^μ are given by

$$B^{\mu\nu} = \partial^\mu B^\nu - \partial^\nu B^\mu, \tag{1.14}$$

$$W_k^{\mu\nu} = \partial^\mu W_k^\nu - \partial^\nu W_k^\mu - g\epsilon_{ijk}W_i^\mu W_j^\nu, \tag{1.15}$$

$$G_k^{\mu\nu} = \partial^\mu G_k^\nu - \partial^\nu G_k^\mu - g_s f_{ijk}G_i^\mu G_j^\nu, \tag{1.16}$$

where the field strength tensor terms $g\epsilon_{ijk}W_i^\mu W_j^\nu$ and $g_s f_{ijk}G_i^\mu G_j^\nu$ indicate the presence of self-interaction terms of the corresponding gauge bosons in the Lagrangian.

The Higgs and lepton fields have no associated color charge, therefore, are untouched by the $SU(3)_C$ local gauge transformations, i.e., the covariant derivatives for the corresponding fields are given by

$$D^\mu \phi = \left(\partial^\mu + \frac{i}{2}gW_i^\mu \sigma_i + \frac{i}{2}g'B^\mu\right)\phi, \tag{1.17}$$

$$D^\mu L_L = \left(\partial^\mu + \frac{i}{2}gW_i^\mu \sigma_i - \frac{i}{2}g'B^\mu\right)L_L, \tag{1.18}$$

where the weak hypercharges are substituted by the associated quantum numbers given in equations 1.3 and 1.4. Further, the right-handed fermions do not participate in weak interactions; therefore, the terms with the generator $\hat{\boldsymbol{T}}$ are omitted for the right-handed chiral fields,

$$D^\mu E_R = \left(\partial^\mu - ig'B^\mu\right)E_R. \tag{1.19}$$

As mentioned, quarks have an associated color charge respecting the local gauge transformations of $SU(3)_C \times U(1)_Y$ for the right-handed chiral states and $SU(3)_C \times SU(2)_L \times U(1)_Y$ for the doublets of left-handed chiral states. The covariant derivatives for the corresponding fields are given by

$$D^\mu U_R = \left(\partial^\mu + \frac{i}{2}g_s G_i^\mu \lambda_i + \frac{2i}{3}g'B^\mu\right)U_R, \tag{1.20}$$

$$D^\mu D_R = \left(\partial^\mu + \frac{i}{2}g_s G_i^\mu \lambda_i - \frac{i}{3}g'B^\mu\right)D_R, \tag{1.21}$$

$$D^\mu Q_L = \left(\partial^\mu + \frac{i}{2}gW_i^\mu \sigma_i + \frac{i}{2}g_s G_j^\mu \lambda_j + \frac{i}{6}g'B^\mu\right)Q_L. \tag{1.22}$$

The kinetic part of the SM Lagrangian describing the space-time propagation of the fermionic fields and the gauge bosons is given by

$$\begin{aligned}\mathcal{L}_{\text{Kinetic}} = &-\frac{1}{4}G_a^{\mu\nu}G_{a\mu\nu} - \frac{1}{4}W_b^{\mu\nu}W_{b\mu\nu} - \frac{1}{4}B^{\mu\nu}B_{\mu\nu} + i\overline{Q}_{L_i}\not{D}Q_{L_i} + i\overline{U}_{R_i}\not{D}U_{R_i} \\ &+ i\overline{D}_{R_i}\not{D}D_{R_i} + i\overline{L}_{L_i}\not{D}L_{L_i} + i\overline{E}_{R_i}\not{D}E_{R_i},\end{aligned} \tag{1.23}$$

where the terms of the form $-\frac{1}{4}F^{\mu\nu}F_{\mu\nu}$ are kinetic energies of the gauge fields [3, 4], and the slashed D is $\gamma_\mu D^\mu$.

Since the left-handed and right-handed chiral states of the fermions respond differently to the $SU(2)$ local gauge transformations, the mass terms of the form $m\overline{\psi}\psi = m\overline{\psi}_L\psi_R + m\overline{\psi}_R\psi_L$ (using the properties of the projection operators given in equation 1.2) cannot be included explicitly as in the Dirac Lagrangian. Therefore, the masses of the fermions and gauge fields are assigned through a different procedure known as the Higgs mechanism. In the SM, the Higgs field at the lowest order is

considered to have the quadratic and quartic terms of the self-interactions, i.e., the Higgs potential has the form of [3, 4]

$$V(\phi) = \mu^2 \phi^\dagger \phi + \lambda \left(\phi^\dagger \phi\right)^2, \tag{1.24}$$

where $\mu^2 < 0$ and $\lambda > 0$ are the free parameters, and ϕ is a doublet of the complex scalar fields given in equation 1.4. The Higgs potential respects the local gauge symmetries of the SM. Under the spontaneous symmetry breaking (SSB), the field ϕ is chosen to acquire the following form,

$$\phi = \frac{1}{\sqrt{2}} \begin{pmatrix} 0 \\ v + h \end{pmatrix}, \tag{1.25}$$

where $\frac{v}{\sqrt{2}} = \sqrt{-\frac{\mu^2}{2\lambda}}$ is the neutral component of the vacuum expectation value of ϕ, and h is the Higgs field expanded perturbatively around the minima of the Higgs potential. The Lagrangian for the field ϕ is defined as

$$\mathcal{L}_\phi = (D^\mu \phi)^\dagger (D_\mu \phi) - V(\phi). \tag{1.26}$$

Substituting the $D^\mu \phi$ from equations 1.17 and 1.25, the physical fields of the electromagnetic (A^μ) and weak interactions (Z, W^μ) are identified as a function of the gauge fields of electroweak GSW model,

$$A^\mu = \frac{g' W_3^\mu + g B^\mu}{\sqrt{g^2 + g'^2}} \qquad \text{with} \quad m_A = 0, \tag{1.27}$$

$$Z^\mu = \frac{g W_3^\mu - g' B^\mu}{\sqrt{g^2 + g'^2}} \qquad \text{with} \quad m_Z = \frac{1}{2} v \sqrt{g^2 + g'^2}, \tag{1.28}$$

$$W^{\pm\mu} = \frac{1}{\sqrt{2}} (W_1^\mu \mp i W_2^\mu) \quad \text{with} \quad m_W = \frac{1}{2} v g, \tag{1.29}$$

where m_A, m_Z, and m_W are the corresponding masses. The Higgs mass is identified to be $m_H = \sqrt{2\lambda} v$. In this mechanism, three degrees of freedom of the Higgs doublet in equation 1.4 are absorbed by the massless Goldston bosons, providing the additional degrees of freedom of the longitudinal polarization to the massive gauge bosons [3, 4].

The fermion masses are introduced in the SM Lagrangian through the Yukawa interactions given as

$$-\mathcal{L}_{\text{Yukawa}} = Y_{ij}^d \overline{Q}_{L_i} \phi D_{R_j} + Y_{ij}^u \overline{Q}_{L_i} \tilde{\phi} U_{R_j} + Y_{ij}^e \overline{L}_{L_i} \phi E_{R_j} + h.c., \tag{1.30}$$

where $Y_{ij}^{(u,d,e)}$ are dimensionless Yukawa couplings with the indices i and j running over three generations of the quarks and leptons, i.e., are the elements of general 3×3 matrices, and $\tilde{\phi}$ is given by $i\sigma_2 \phi^*$. $h.c.$ represents the Hermitian conjugation of the explicit terms. The renormalizable SM Lagrangian invariant under the local gauge transformations of $SU(3)_C \times SU(2)_L \times U(1)_Y$ is given by

$$\mathcal{L}_{\text{SM}} = \mathcal{L}_{\text{Kinetic}} + \mathcal{L}_{\text{Yukawa}} + \mathcal{L}_\phi. \tag{1.31}$$

Substituting the Higgs field by the vacuum expectation value,

$$\langle 0|\,\phi\,|0\rangle = \frac{1}{\sqrt{2}}\begin{pmatrix}0\\ v\end{pmatrix}, \tag{1.32}$$

the $\mathcal{L}_{\text{Yukawa}}$ is given as

$$-\mathcal{L}_{\text{Yukawa}} = \overline{u'}_{L_i}(vY^u/\sqrt{2})_{ij}u'_{R_j} + \overline{d'}_{L_i}(vY^d/\sqrt{2})_{ij}d'_{R_j} + \bar{l}_{L_i}(vY^l/\sqrt{2})_{ij}l_{R_j}, \tag{1.33}$$

where l stands for three generations of the charged leptons and $M^{(u,d,l)} = \frac{v}{\sqrt{2}}Y^{(u,d,l)}$ are the general 3×3 mass matrices. The mass matrix for the lepton sector is diagonal, as no flavor-violating interactions have been observed so far. Therefore, the charged lepton masses are identified to be,

$$m_l = \frac{1}{\sqrt{2}}vg_l, \tag{1.34}$$

where g_l (Yukawa couplings) are the diagonal elements of the Yukawa matrix in the lepton sector. However, the mass matrices in the quark sector are non-diagonal. The diagonalized matrices ($\hat{M}^q$) are obtained by using the bi-unitary transformations,

$$\hat{M}^q = V_L^q M^q V_R^{q^\dagger}, \tag{1.35}$$

where $q = \{u, d\}$ is a notion representing the up and down type quarks, and $V^q_{(L,R)}$ are the 3×3 unitary matrices. The mass eigenstates ($q_{(L,R)}$) of the quark fields are given by

$$q_L = V_L^q q'_L, \tag{1.36}$$
$$q_R = V_R^q q'_R, \tag{1.37}$$

where the states on the right-hand side are identified to be the interaction basis. Therefore, the $\mathcal{L}_{\text{Yukawa}}$ in mass basis is as,

$$-\mathcal{L}_{\text{Yukawa}} = m_i^u \overline{u}_{L_i} u_{R_i} + m_i^d \overline{d}_{L_i} d_{R_i} + m_i^l \bar{l}_{L_i} l_{R_i}, \tag{1.38}$$

where $m_i^q = \frac{1}{\sqrt{2}}vg_i^q$ are the masses of the quarks with g_i^q being the Yukawa couplings in the mass basis and i runs over three generations of the quarks and leptons. Since the left-handed and right-handed fermions have different weak hypercharge, the inbuilt $SU(3)_C \times SU(2)_L \times U(1)_Y$ local gauge symmetry of the $\mathcal{L}_{\text{Yukawa}}$ in equation 1.30 has spontaneously broken to $SU(3)_C \times U(1)_{\text{EM}}$ due to the introduction of the mass terms in the Lagrangian. The symmetry survival is possible because the left-handed and right-handed chiral states of the fermions have the equal Q_{EM}, and their color wave functions bear the same phases under $SU(3)_C$ transformation. An interpretation of the resultant gauge symmetry is that the corresponding gauge bosons A^μ and G_i^μ are still massless as found in nature. Thus, the Higgs mechanism provides the masses to the fermions through the SSB of the electroweak gauge group.

1.4 Charged and Neutral Current Interactions

The charged current interactions in the quark sector are identified from the gauge field interaction terms embedded in the kinetic part of the SM Lagrangian corresponding to the local $SU(2)_L$ symmetry, i.e., from the

$$\overline{Q}_L \frac{g}{2} \gamma_\mu \sigma_1 Q_L W_1^\mu + \overline{Q}_L \frac{g}{2} \gamma_\mu \sigma_2 Q_L W_2^\mu + \overline{Q}_L \frac{g}{2} \gamma_\mu \sigma_3 Q_L W_3^\mu \tag{1.39}$$

terms of the $i\overline{Q}_L \not{D} Q_L$. Defining the isospin raising and lowering operators as $\sigma_\pm = \frac{1}{2}(\sigma_1 \pm i\sigma_2)$, which raises and lowers the third component of the weak isospin of the doublet members by one unit, and the $W^{\pm\mu}$ from the equation 1.29, the equation 1.39 can be written as

$$j_+^\mu W_\mu^+ + j_-^\mu W_\mu^- + j_3^\mu W_\mu^3, \tag{1.40}$$

where the currents

$$\begin{aligned} j_+^\mu &= \frac{g}{\sqrt{2}} \overline{Q}_L \gamma^\mu \sigma_+ Q_L \\ &= \frac{g}{\sqrt{2}} \begin{pmatrix} \overline{u'}_L & \overline{d'}_L \end{pmatrix} \gamma^\mu \begin{pmatrix} 0 & 1 \\ 0 & 0 \end{pmatrix} \begin{pmatrix} u'_L \\ d'_L \end{pmatrix} \\ &= \frac{g}{\sqrt{2}} \overline{u'}_L \gamma^\mu d'_L \end{aligned} \tag{1.41}$$

and

$$\begin{aligned} j_-^\mu &= \frac{g}{\sqrt{2}} \overline{Q}_L \gamma^\mu \sigma_- Q_L \\ &= \frac{g}{\sqrt{2}} \begin{pmatrix} \overline{u'}_L & \overline{d'}_L \end{pmatrix} \gamma^\mu \begin{pmatrix} 0 & 0 \\ 1 & 0 \end{pmatrix} \begin{pmatrix} u'_L \\ d'_L \end{pmatrix} \\ &= \frac{g}{\sqrt{2}} \overline{d'}_L \gamma^\mu u'_L \end{aligned} \tag{1.42}$$

are the charged currents with a difference of $\pm e$ charge at the vertices, whereas the current given by

$$\begin{aligned} j_3^\mu &= \frac{g}{2} \overline{Q}_L \gamma^\mu \sigma_3 Q_L \\ &= \frac{g}{2} \begin{pmatrix} \overline{u'}_L & \overline{d'}_L \end{pmatrix} \gamma^\mu \begin{pmatrix} 1 & 0 \\ 0 & -1 \end{pmatrix} \begin{pmatrix} u'_L \\ d'_L \end{pmatrix} \\ &= \frac{g}{2} \left(\overline{u'}_L \gamma^\mu u'_L - \overline{d'}_L \gamma^\mu d'_L \right) \end{aligned} \tag{1.43}$$

is a neutral current. The Lagrangian for the charged current in the quark sector is identified to be,

$$\mathcal{L}_q^{\text{charged}} = \frac{g}{\sqrt{2}} \left(\overline{u'}_{L_i} \gamma^\mu d'_{L_i} W_\mu^+ + \overline{d'}_{L_i} \gamma^\mu u'_{L_i} W_\mu^- \right), \tag{1.44}$$

where i is summed over three generations of the quarks. The second term in the Lagrangian is a Hermitian conjugate of the first and vice-versa. The Lagrangian can be written in the matrix form as

$$\begin{aligned}
\mathcal{L}_q^{\text{charged}} &= \frac{g}{\sqrt{2}} \begin{pmatrix} \overline{u'}_L & \overline{c'}_L & \overline{t'}_L \end{pmatrix} \gamma^\mu \begin{pmatrix} d'_L \\ s'_L \\ b'_L \end{pmatrix} W_\mu^+ + h.c. \\
&= \frac{g}{\sqrt{2}} \begin{pmatrix} \overline{u'}_L & \overline{c'}_L & \overline{t'}_L \end{pmatrix} V_L^{u\dagger} V_L^u \gamma^\mu V_L^{d\dagger} V_L^d \begin{pmatrix} d'_L \\ s'_L \\ b'_L \end{pmatrix} W_\mu^+ + h.c. \\
&= \frac{g}{\sqrt{2}} \begin{pmatrix} \overline{u}_L & \overline{c}_L & \overline{t}_L \end{pmatrix} \gamma^\mu V_L^u V_L^{d\dagger} \begin{pmatrix} d_L \\ s_L \\ b_L \end{pmatrix} W_\mu^+ + h.c. \\
&= \frac{g}{\sqrt{2}} \begin{pmatrix} \overline{u}_L & \overline{c}_L & \overline{t}_L \end{pmatrix} \gamma^\mu V_{\text{CKM}} \begin{pmatrix} d_L \\ s_L \\ b_L \end{pmatrix} W_\mu^+ + h.c., \qquad (1.45)
\end{aligned}$$

where the unitary matrices of equations 1.36 and 1.37 are used to transform the interaction basis into the mass basis and V_{CKM} is the unitary Cabibbo–Kobayashi–Maskawa (CKM) matrix. The non-diagonal nature of the CKM matrix induces the mixing of the quarks and the flavor-changing process, as evident from the experimental results. More on the CKM matrix will be discussed in the next section.

The Lagrangian for the charged current interactions in the quark sector (equation 1.45) can be written in the non-chiral states using the projection operators (equations 1.1 and 1.2), as

$$\mathcal{L}_q^{\text{charged}} = \frac{g}{\sqrt{2}} \begin{pmatrix} \overline{u} & \overline{c} & \overline{t} \end{pmatrix} \gamma^\mu \frac{1}{2}(1-\gamma^5) V_{\text{CKM}} \begin{pmatrix} d \\ s \\ b \end{pmatrix} W_\mu^+ + h.c., \qquad (1.46)$$

exhibiting the V-A nature of the weak interactions. Following a similar procedure in the lepton sector, the Lagrangian for the charged current interaction interactions is given as

$$\mathcal{L}_l^{\text{charged}} = \frac{g}{\sqrt{2}} \begin{pmatrix} \overline{\nu}_e & \overline{\nu}_\mu & \overline{\nu}_\tau \end{pmatrix} \gamma^\mu \frac{1}{2}(1-\gamma^5) \begin{pmatrix} e \\ \mu \\ \tau \end{pmatrix} W_\mu^+ + h.c.. \qquad (1.47)$$

The absence of the CKM-like non-diagonal matrix in the lepton sector represents the non-mixing of the leptons mass-eigen states. Further, the Lagrangian in equation 1.47 demonstrates the lepton universality of the charged-current weak interactions in the lepton sector.

The neutral current mediated by the Z boson has the interaction terms from both the left-handed and right-handed chiral states, contrary to the prediction of the equation 1.43. The neutral current associated with the third component of the W gauge boson can also be written as

$$j_3^\mu = \frac{g}{2} I_W^{(3)} \overline{f'}_L \gamma^\mu f'_L,$$

where f represents the fermionic fields with the corresponding third component of the weak isospin, $I_W^{(3)} = \pm\frac{1}{2}$. Further, the basis can be chosen to be mass basis without the loss of generality as the spinor and adjoint-spinor correspond to the same fermion, i.e.,

$$j_3^\mu = \frac{g}{2} I_W^{(3)} \overline{f}_L \gamma^\mu f_L. \tag{1.48}$$

By writing the ratio of the gauge coupling of the $U(1)_Y$ and $SU(2)_L$ symmetries as,

$$\tan\theta_W = \frac{g'}{g}, \tag{1.49}$$

fields for the physical bosons given in equations 1.27 and 1.28 can be written as

$$A^\mu = \cos\theta_W B^\mu + \sin\theta_W W_3^\mu, \tag{1.50}$$
$$Z^\mu = -\sin\theta_W B^\mu + \cos\theta_W W_3^\mu, \tag{1.51}$$

where θ_W is the weak mixing angle of the GSW electroweak model [3, 4]. In this model, the currents corresponding to the electromagnetic and Z mediated interactions have contributions from currents associated with the exchange of B^μ and W_3^μ gauge fields,

$$j_{\text{em}}^\mu = \cos\theta_W j_Y^\mu + \sin\theta_W j_3^\mu, \tag{1.52}$$
$$j_Z^\mu = -\sin\theta_W j_Y^\mu + \cos\theta_W j_3^\mu. \tag{1.53}$$

The current j_Y^μ associated with the preservation of the local $U(1)_Y$ gauge symmetry is dictated by $ig'\frac{\hat{Y}}{2}B^\mu$ term of the covariant derivative and is the same for the left-handed and right-handed chiral states, except the dependence on the respective weak hypercharge quantum numbers Y_L^f and Y_R^f,

$$j_Y^\mu = \frac{g'}{2}\left(Y_L^f \overline{f}_L \gamma^\mu f_L + Y_R^f \overline{f}_R \gamma^\mu f_R\right). \tag{1.54}$$

Using the weak hypercharge $Y_f = 2(Q_f^{\text{EM}} - I_W^{(3)})$ of the electroweak model, and given that $I_W^{(3)} = 0$ for the right-handed fermions and $\pm\frac{1}{2}$ for the left-handed fermions; the current associated with the exchange of physical Z boson can be obtained by substituting the currents given in equations 1.48 and 1.54, as

$$\begin{aligned} j_Z^\mu &= \frac{g}{\cos\theta_W}\left[\left(I_W^{(3)} - Q_f \sin^2\theta_W\right)\overline{f}_L\gamma^\mu f_L - \left(Q_f \sin^2\theta_W\right)\overline{f}_R\gamma^\mu f_R\right], \\ &= g_Z\left(c_L^f \overline{f}_L \gamma^\mu f_L + c_R^f \overline{f}_R \gamma^\mu f_R\right), \end{aligned} \tag{1.55}$$

where $g_Z = \frac{g}{\cos\theta_W}$ is the coupling of the physical Z boson and $c_L^f = \left(I_W^{(3)} - Q_f \sin^2\theta_W\right)$ and $c_R^f = -Q_f \sin^2\theta_W$ are the coefficients corresponding to the left-handed and right-handed currents. Contrary to the $W^\pm$ bosons, which couple only to the left-handed chiral states, the Z-boson couples with both chiral states but with different strengths. The Lagrangian for the Z mediated interactions is given as

$$\mathcal{L}_Z^{\text{neutral}} = g_Z\left(c_L^f \overline{f}_L \gamma^\mu f_L + c_R^f \overline{f}_R \gamma^\mu f_R\right) Z_\mu, \tag{1.56}$$

where f is summed over all the fermions. It is worth emphasizing that the fermion flavor remains unchanged at the Z-exchange vertices.

1.5 The CKM Matrix

From equation 1.46, the flavor-changing charged current in the quark sector can be written in the matrix form as

$$j_+^\mu = \frac{g}{\sqrt{2}} \begin{pmatrix} \overline{u} & \overline{c} & \overline{t} \end{pmatrix} \gamma^\mu \frac{1}{2}(1-\gamma^5) V_{\text{CKM}} \begin{pmatrix} d \\ s \\ b \end{pmatrix}. \tag{1.57}$$

However, there is nothing particular about an interaction basis that can be re-defined, i.e. the new interaction basis are

$$\begin{pmatrix} d' \\ s' \\ b' \end{pmatrix} = \begin{pmatrix} V_{ud} & V_{us} & V_{ub} \\ V_{cd} & V_{cs} & V_{cb} \\ V_{td} & V_{ts} & V_{tb} \end{pmatrix} \begin{pmatrix} d \\ s \\ b \end{pmatrix}, \tag{1.58}$$

where the transformation matrix is the CKM matrix. Using equation 1.58, the flavor-changing charged current for the quarks sector can be written as

$$j_+^\mu = \frac{g}{\sqrt{2}} \begin{pmatrix} \overline{u} & \overline{c} & \overline{t} \end{pmatrix} \gamma^\mu \frac{1}{2}(1-\gamma^5) \begin{pmatrix} d' \\ s' \\ b' \end{pmatrix}, \tag{1.59}$$

which is diagonal with equal couplings for all three generations, similar to the lepton-sector predicted in equation 1.47. The result can be interpreted as the existence of quark doublets with upper and lower members being the mass and interaction basis or vice-versa in a different choice,

$$\begin{pmatrix} u \\ d' \end{pmatrix}, \begin{pmatrix} c \\ s' \end{pmatrix}, \begin{pmatrix} t \\ b' \end{pmatrix} \tag{1.60}$$

in which the $W^\pm$ mediated flavor-changing charged current interactions are diagonal, i.e., interchanges among themselves, and are universal. The interaction basis written in the explicit form

$$\begin{aligned} d' &= V_{ud}d + V_{us}s + V_{ub}b, \\ s' &= V_{cd}d + V_{cs}s + V_{cb}b, \\ b' &= V_{td}d + V_{bs}s + V_{cb}b, \end{aligned} \tag{1.61}$$

are the superposition of the mass eigenstates with coefficients equal to the CKM matrix elements. The coefficients determine the couplings of the up-type quarks with the down-type quarks in the flavor-changing charged current interactions. Using equation 1.61, the quarks doublets can be written as

$$\begin{pmatrix} u \\ \\ V_{ud}d + V_{us}s + V_{ub}b \end{pmatrix}, \begin{pmatrix} c \\ \\ V_{cd}d + V_{cs}s + V_{cb}b \end{pmatrix}, \begin{pmatrix} t \\ \\ V_{td}d + V_{bs}s + V_{cb}b \end{pmatrix}. \tag{1.62}$$

The CKM matrix is a 3×3 unitary matrix with 18 (nine real and nine imaginary) quantities. Three of the imaginary phases associated with the d quark field can be extracted out of the doublets and can be absorbed by redefining the fields for u, c, and t quarks. Phases for any of the two matrix elements associated with the s and b quarks can be absorbed in the corresponding quark fields. The introduction of the new phases in the mass basis of the charged current interaction does not affect the currents for other interactions because of their diagonal nature. Of the thirteen remaining parameters, the normality and orthogonality conditions of the quarks doublets impose nine (three and six, respectively) constraints. Therefore, the CKM matrix can be parameterized using four independent parameters with three real parameters and one imaginary phase. An explicit treatment of the CKM matrix can be found in [5]. In the SM, the CKM matrix is parameterized using three Euler angles mixing the generations and one complex phase as [6]

$$V_{\rm CKM} = \begin{pmatrix} c_{12}c_{13} & s_{12}c_{13} & s_{13}e^{-i\delta} \\ -s_{12}c_{23} - c_{12}s_{23}s_{13}e^{i\delta} & c_{12}c_{23} - c_{12}s_{23}s_{13}e^{i\delta} & s_{23}c_{13} \\ s_{12}s_{23} - c_{12}s_{23}s_{13}e^{i\delta} & -c_{12}s_{23} - s_{12}c_{23}s_{13}e^{i\delta} & c_{23}c_{13} \end{pmatrix}, \tag{1.63}$$

where c_{ij} and s_{ij} are the cosine and sine of the mixing angles θ_{ij}, and δ is the complex phase responsible for the CP-violation in flavor changing processes of the quark sector. The CKM matrix best known from the experimental measurements is [1]

$$\begin{aligned} V_{\rm CKM} &= \begin{pmatrix} |V_{ud}| & |V_{us}| & |V_{ub}| \\ |V_{cd}| & |V_{cs}| & |V_{cb}| \\ |V_{td}| & |V_{ts}| & |V_{tb}| \end{pmatrix} \\ &= \begin{pmatrix} 0.97446 \pm 0.00010 & 0.22452 \pm 0.00044 & 0.00365 \pm 0.00012 \\ 0.22438 \pm 0.00044 & 0.97359^{+0.00010}_{-0.00011} & 0.04214 \pm 0.00076 \\ 0.00896^{+0.00024}_{-0.00023} & 0.04133 \pm 0.00074 & 0.999105 \pm 0.000032 \end{pmatrix}. \end{aligned} \tag{1.64}$$

As can be seen from equation 1.64, the experimental values of the CKM elements $|V_{ud}|$, $|V_{cs}|$, and $|V_{tb}|$ are approximately equal to 1, whereas the elements away from the diagonals are significantly small following a hierarchy, for example, $|V_{ud}| >> |V_{us}| >> |V_{ub}|$. Consequently, the CKM matrix is expanded around the identity matrix in terms of the relatively small parameter $\lambda = \sin\theta_c = 0.225$, where $\theta_c \equiv \theta_{12}$ is the Cabibo angle. The CKM matrix with unitarity condition to the order of $\mathcal{O}(\lambda^4)$ is given as

$$V_{\rm CKM} = \begin{bmatrix} 1 - \lambda^2/2 & \lambda & A\lambda^3(\rho - i\eta) \\ -\lambda & 1 - \lambda^2/2 & A\lambda^2 \\ A\lambda^3(1 - \rho - i\eta) & -A\lambda^2 & 1 \end{bmatrix} + \mathcal{O}(\lambda^4), \tag{1.65}$$

where ρ, η, and A are the real parameters. This matrix is known as the Wolfenstein parameterization of the CKM matrix [7]. In terms of the standard choice of the CKM

matrix given in equation 1.63, the Wolfenstein parameters are defined as [1, 7, 8, 9],

$$s_{12} = \lambda, \qquad s_{23} = A\lambda^2, \qquad s_{13}e^{i\delta} = A\lambda^3(\rho + i\eta)$$
$$\rho = \frac{s_{13}e^{i\delta}}{s_{12}s_{23}}\cos\delta \qquad \eta = \frac{s_{13}e^{i\delta}}{s_{12}s_{23}}\sin\delta. \tag{1.66}$$

The unitarity condition of the CKM matrix follows that

$$\sum_i V_{ij}V_{ik}^* = \delta_{jk} \qquad \text{and} \qquad \sum_j V_{ij}V_{kj}^* = \delta_{ik}. \tag{1.67}$$

One of the six non-diagonal equations, most relevant to the flavor physics in B-mesons, is

$$V_{ud}V_{ub}^* + V_{cd}V_{cb}^* + V_{td}V_{tb}^* = 0,$$

which can be written as

$$\frac{V_{ud}V_{ub}^*}{V_{cd}V_{cb}^*} + 1 + \frac{V_{td}V_{tb}^*}{V_{cd}V_{cb}^*} = 0, \tag{1.68}$$

by dividing each term by $V_{cd}V_{cb}^*$. Defining the [8, 9]

$$\overline{\rho} + i\overline{\eta} = -\frac{V_{ud}V_{ub}^*}{V_{cd}V_{cb}^*} \quad \text{and} \quad 1 - (\overline{\rho} + i\overline{\eta}) = \frac{V_{td}V_{tb}^*}{V_{cd}V_{cb}^*}, \tag{1.69}$$

the unitarity condition in equation 1.68 can be expressed as a triangle with vertices at $(0,0)$, $(1,0)$, and $(\overline{\rho},\overline{\eta})$ in the $\overline{\rho}-\overline{\eta}$ complex plane, known as the unitarity triangle (UT). The UT corresponding to the above equation is shown in Figure 1.2. The parameters $\overline{\rho}$ and $\overline{\eta}$ are related to the original parameters as

$$\rho + i\eta = \frac{\sqrt{1 - A^2\lambda^4}(\overline{\rho} + i\overline{\eta})}{\sqrt{1 - \lambda^2[1 - A^2\lambda^4(\overline{\rho} + i\overline{\eta})]}}. \tag{1.70}$$

The angles of the UT are

$$\beta \quad \text{or} \quad \phi_1 = \arg\left[-\frac{V_{cd}V_{cb}^*}{V_{td}V_{tb}^*}\right],$$
$$\alpha \quad \text{or} \quad \phi_2 = \arg\left[-\frac{V_{td}V_{tb}^*}{V_{ud}V_{ub}^*}\right],$$
$$\gamma \quad \text{or} \quad \phi_3 = \arg\left[-\frac{V_{ud}V_{ub}^*}{V_{cd}V_{cb}^*}\right]. \tag{1.71}$$

Precise measuring of the angles and sides of the UTs using the flavor-changing processes provide the test of CKM matrix unitarity. Further, the precise measurements of UT parameters help in constraining various beyond the SM physics models. The fit of the numerous independent studies in flavor physics yields the Wolfenstein parameters to be [1],

$$\lambda = 0.22650 \pm 0.00048 \qquad A = 0.790^{+0.017}_{-0.012}$$
$$\overline{\rho} = 0.141^{+0.016}_{-0.017} \qquad \overline{\eta} = 0.357 \pm 0.011. \tag{1.72}$$

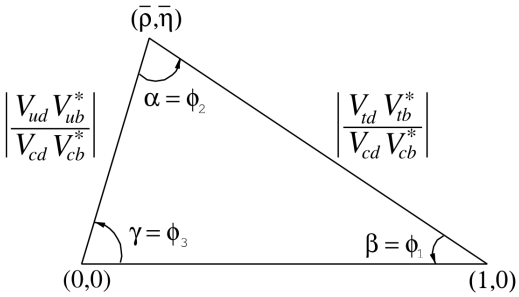

Figure 1.2: The unitarity triangle [1].

Despite the tremendous success of the SM in explaining the thousands of experimental data, it is considered only an effective theory of a more general theory at a higher energy scale. This is evident because the SM fails to address the issues, such as the non-zero mass of the neutrinos, as known from the observed phenomenon of the neutrino oscillations. Further, the known matter-antimatter asymmetry of the universe can not be explained with the CP-phase δ alone. The presence of dark matter and its interactions with ordinary matter is untouched within the framework of the SM.

Historically, the predictions of the c and t quarks were led by flavor physics investigations. Therefore, the possibility of new fundamental particles or the interactions at high energy scales can be explored indirectly in flavor physics at a low energy scale, which is currently accessible in high luminosity machines, such as the Belle and Belle II, LHCb, etc.

1.6 An Overview of the B-meson Physics

B-mesons are the bound states of the bottom anti-quarks and a quark q, where q can be u, d, s, and c, compositing the configurations of B^+, B^0_d, B^0_s, and B^+_c mesons, respectively. The charge conjugation of these states corresponds to B^-, $\bar{B}^0_d$, $\bar{B}^0_s$, and B^-_c mesons. This thesis focuses on the dynamics of the B^0_s meson, also known as the strange-B meson.

From the CKM matrix elements discussed in the previous section, the transitions of the b (third-generation) quark to lighter quarks, the charm (second-generation) and up (first-generation) quarks via the mediation of W^--boson, are Cabibo suppressed by order of $\mathcal{O}(10^{-2})$ and $\mathcal{O}(10^{-3})$, respectively. Contrary to this, the direct transition of $b \to s$ or d is forbidden by the GIM mechanism [10]. Due to the known couplings, the computation of the weak currents is more straightforward relative to the incorporation of strong interactions of the quarks via gluon exchange. The QCD Lagrangian determining the strong interactions can be extracted from the kinetic part of the SM Lagrangian in equation 1.23 and the covariant derivatives of the quark fields,

$$L_{\text{QCD}} = \bar{q}_j i\gamma^\mu \left(\partial_\mu + i\frac{g_s}{2}G^a_\mu \lambda^a\right) g_j - \frac{1}{4}G^{\mu\nu}_a G^a_{\mu\nu}, \tag{1.73}$$

where the indices j and a are summed over the quark fields and the gauge boson fields corresponding to the $SU(3)_C$ symmetry, respectively. $G^a_{\mu\nu}$ is the field strength tensor given in equation 1.16. As stated earlier, the non-abelian nature of the $SU(3)$ group requires the introduction of terms responsible for the self-interaction of the gauge bosons. As a result, the gluons interact with the quarks and among themselves, making the computation formidable in hadron formation.

Further, the sum of rest mass energies of the bottom ($m_b \sim 4.18$ GeV/c^2) and strange ($m_s \sim 93.4$ MeV/c^2) quarks is of the order of 1 GeV less than the typical rest mass energy of B^0_s meson ($m_{B^0_s} \sim 5.37$ GeV/c^2) [1], which is mainly stored as the binding energy of the B^0_s mesons. The computation of the B meson decay amplitudes is complexed by the involvement of different energy scales, i.e., the scale of order $\mathcal{O}(M_W \sim 80$ GeV/$c^2)$ for weak interaction, the mass scale of the bottom quark, the hadronic energy scale of order $\mathcal{O}(1$ GeV), and the strong interaction scale λ_{QCD} of order $\mathcal{O}(200$ MeV). Therefore, an effective field theory of energy scales from weak interaction down to hadronic energy is required. This is achieved in a framework of writing the weak Hamiltonian in terms of the Operator Product Expansion [11, 12, 13],

$$H_{\text{eff}} = \frac{G_f}{\sqrt{2}} \sum_{q=u,c} v_q \Bigg\{ C_1(\mu) Q^q_1(\mu) + C_2(\mu) Q^q_2(\mu) + \sum_{k=3}^{10} C_k(\mu) Q^q_k(\mu) + C_{7\gamma}(\mu) Q^q_{7\gamma}(\mu) + C_{8g}(\mu) Q^q_{8g}(\mu) \Bigg\}, \quad (1.74)$$

where G_f is Fermi constant, $v_q = V_{qb} V^*_{q(d,s)}$ are the CKM matrix elements incorporating the couplings of W bosons at the flavor changing vertices, $Q_i(\mu)$ are the four-fermion local operators representing the QCD and electroweak interactions, and $C_i(\mu)$ are the Wilson coefficients. Interactions above the scale μ, which correspond to the short distance interactions, are integrated out to contain in coefficients $C_i(\mu)$. In contrast, the long distance non-perturbative interactions with the scale less than μ are contained in operators Q_i. In general, the amplitude for an exclusive $B \to M_1 M_2$ decay,

$$A(B \to M_1 M_2) = \frac{G_f}{\sqrt{2}} \sum_i v C_i(\mu) \langle M_1 M_2 | Q_i(\mu) | B \rangle , \quad (1.75)$$

have to be independent of the scale μ. The exact cancellation of the oppositely scale dependence of the two factors is made to possible by renormalization group running of the effective field theory. The values for coefficients $C_i(\mu)$ are reliably computed at the various scales in reference [11].

The first two operators, i.e., $Q_{1,2}$, are current-current operators specifying the flavor-changing processes. An example of such is tree level $b \to c\bar{c}s$ transition in the $\bar{B}^0_s \to J/\psi\eta$ decay,

$$Q_1 = \left[\bar{c}_\alpha \gamma^\mu \left(1 - \gamma^5\right) b_\alpha\right] \left[\bar{s}_\beta \gamma_\mu \left(1 - \gamma^5\right) c_\beta\right] ,$$
$$Q_2 = \left[\bar{c}_\alpha \gamma^\mu \left(1 - \gamma^5\right) b_\beta\right] \left[\bar{s}_\beta \gamma_\mu \left(1 - \gamma^5\right) c_\alpha\right] ,$$

where α and β represent the QCD interactions of the weak currents via gluon exchange, the gluons exchanged among the parting mesons are the ones responsible for the long-distance interactions. Since these gluons are low-momenta, hence are also termed as 'soft' in literature. At higher order, the amplitude A has contribution from loop level $b \to s$ transition. In this regard, the operators Q_{3-6} and Q_{7-10} incorporate the desired QCD and electroweak penguins contributions, respectively. Higher order operators with γ and g labels represent the contribution to the hadronic matrix elements from magnetic penguins. An explicit form of such operators can be found somewhere else in reference [11]. The rest of the task is computing the hadronic matrix elements.

There are several theoretical approaches dealing with the complexity of the hadronic-matrix element calculation, such as perturbative QCD (pQCD) [14, 15, 16], QCD-factorization [17, 18, 19, 20], and the soft collinear effective field theory [21]. These approaches utilize the scale hierarchy of $m_b >> \lambda_{\rm QCD}$ and expand the hadronic matrix elements in the powers of $\frac{\lambda_{\rm QCD}}{m_b}$ and or α_s at higher orders. However, the scales at which the Wilson coefficients are computed differ among the approaches; such as, the pQCD has low scales of order 1-2 GeV compared to the QCDF, which evaluates the coefficients at a scale of order $\mathcal{O}(m_b)$. The pQCD considers the transverse momentum of the valence quarks in the hadrons resulting in the decay amplitudes as a function of the light-cone wave functions of the mesons, hard scattering function, harder Wilson coefficients, and the Sudokov factors [14, 15, 16]. The QCDF factorizes the hadronic matrix elements as a function of the $B \to M$ form factors, the light-cone distribution functions of the mesons, and perturbative calculable hard-scattering functions [22]. These approaches incorporates the non-perturbatively effects in form factors and light-cone wave functions. As a result, the long-distance non-perturbative contributions of the $\langle M_1 M_2 | \, Q_i(\mu) \, | B \rangle$ are factorized into simpler objects, such as the single state of mesons (light-cone distribution functions) and form factors, which ideally should be extracted from the experimental measurements. Further detailed information on the approaches can be found in corresponding references.

1.7 Significance of the Decay $B_s^0 \to J/\psi\pi^0$

The heavy-flavored B-meson dynamics have attracted the theoretical and experimental high-energy physics communities for the last few decades. Understanding the dynamics governing the rare decay of heavy mesons is an excellent platform to test the SM up to the scales that the particle accelerators cannot currently access. Further, the development of effective field theories has allowed us to predict the partial decay widths correctly to a large extent. Any deviation of the experimental measurement from the SM prediction would hint at the new physics (NP).

The branching fraction $\mathcal{B}(B_s^0 \to J/\psi\pi^0)$ can be predicted at the leading order from the measurement of branching fraction $\mathcal{B}(B_s^0 \to J/\psi\eta)$ [1] with a suppression factor of order $\mathcal{O}(10^{-2})$ due to strong-isospin violation in the $\eta - \pi^0$ transition [23, 24]. The factor is naively predicted from the measured ratio of the decay widths

for $\psi' \to J/\psi\pi^0$ and $\psi' \to J/\psi\eta$ transitions [25] and corresponding theoretical prediction for $\Upsilon(2S) \to \Upsilon(1S)\pi^0$ and $\Upsilon(2S) \to \Upsilon(1S)\eta$ transitions. Thus, we expect the branching fraction $\mathcal{B}(B_s \to J/\psi\pi^0)$ of the order of 4×10^{-6} due to $\eta - \pi^0$ transition.

At the sub-leading orders, the $B_s^0 \to J/\psi\pi^0$ decay proceeds through the W-boson exchange or penguin-annihilation processes, as shown in Fig. 1.3. Despite the general progress in the field, the amplitudes for these so-called weak annihilation transitions have resisted attempts, and the corresponding contributions are either completely ignored or roughly estimated in the calculations. The QCDF [17, 18] approach suffers significant uncertainties due to the endpoint singularities, whereas the pQCD does not differentiate among exchange and annihilation topologies [16]. Similarly, not much progress for such transitions has been seen in the SCET. For example, the results from $B_d^0 \to J/\psi\pi^0$ indicate that the penguin contribution in which d quark participates as a spectator is small compared to the "tree-level" $b \to c\bar{c}d$ transition [26], whereas the contributions from the penguin-annihilation and exchange amplitudes are not considered in the theoretical calculation [27]. Recent measurements of the branching fractions of $B_d^0 \to K^+K^-$ and $B_s^0 \to \pi^+\pi^-$ have shown that the involvement of weak annihilation transitions are significantly small [28]. A measurement of the branching fraction less than the expectation will discard the possibility of $\eta - \pi^0$ transition favouring the annihilation mechanism. Therefore, an experimental investigation of the decay $B_s^0 \to J/\psi\pi^0$ is desirable.

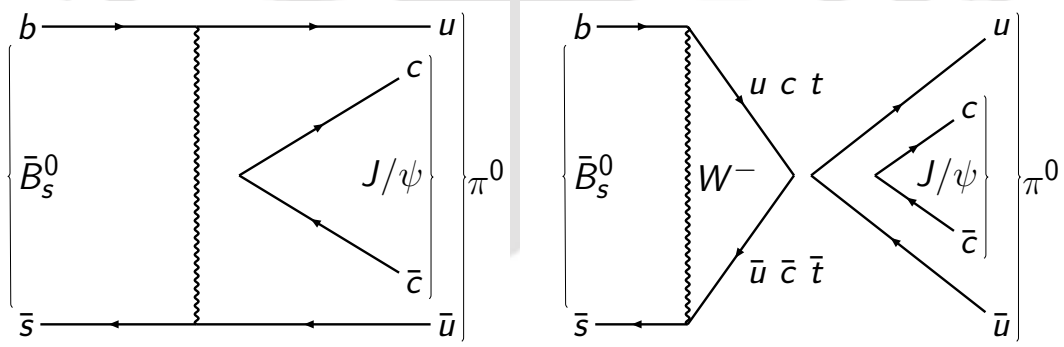

(a) (b)

Figure 1.3: Dominant Feynman diagrams for $B_s^0 \to J/\psi\pi^0$: (a) W-exchange and (b) penguin-annihilation topologies.

The decay $B_s^0 \to J/\psi\pi^0$ was first studied by the L3 collaboration in 1997. In the absence of any signal using 3.5 million hadronic decay of Z-boson, the L3 collaboration set an upper limit on the branching fraction $\mathcal{B}(B_s^0 \to J/\psi\pi^0)$ of 1.2×10^{-3} at 90% confidence level (CL).

1.8 Summary

In this chapter, we discussed the theoretical framework describing the interactions of elementary particles through the most general SM Lagrangian and corresponding gauge transformations. We have briefly introduced the Higgs mechanism responsible for the masses of the elementary particles. We emphasized the flavor-changing charged current interactions and the quark mixing via the CKM matrix. Further, the neutral current interactions and the universality of the weak interactions in interaction bases are thoroughly discussed in this chapter. In the last sections, we briefly review the physics of B mesons and provide the significance of the study of $B_s^0 \to J/\psi\pi^0$.

Chapter 2

The Belle Experiment at KEKB

2.1 Introduction

KEKB is an asymmetric-energy, electron-positron collider designed to copiously produce the $B\bar{B}$ mesons at the High Energy Research Organization, KEK, in Tsukuba, Japan. The Belle collaboration with scientist from around 20 countries, and over 60 institutions have collected the experimental physics data using the Belle detector from 1999 to 2010, accounting for a total integrated luminosity of ~ 1 ab^{-1}. This chapter discusses the experimental facility, mainly comprised of the KEKB accelerator and the Belle detector. A detailed description is given elsewhere [29] and [2].

2.2 The KEKB Accelerator

The KEKB [29] is an asymmetric energy electron-positron collider located 11 m below the ground level in a tunnel of approximately 3 km in circumference, used earlier for the TRISTAN experiment [30]. The tunnel consists of high and low energy rings, known as 'HER' and 'LER', to circulate the e^- and e^+ beams in opposite directions. HER and LER can store the currents up to 1.1 A and 2.6 A using the 508.9 MHz radio frequency (RF) accelerator systems [31, 32]. The rings cross at two points, at the interaction point (IP), where the Belle detector tracks the produced cascade in collisions, and at different heights just opposite the IP, where the e^+e^- does not collide. The e^- and e^+ beams are injected directly in bunches into the storage rings with energy of 8.0 and 3.5 GeV using a J-shaped complex-LINAC, respectively [33]. The beams are circulated in precise paths with the help of dipole, quadrupole, and sextupole magnets. Figure 2.1 shows the schematic layout of the KEKB accelerator. The e^- beam is generated by evaporating electrons off the filament. An offshoot of the e^- beam with an energy of 3.7 GeV impinges on the tungsten target (replaced by a tungsten crystal in September 2006) to produce the electron-positron pairs. Generated e^+ are captured by employing the solenoidal magnetic field, the so-called quarter-wave transformer, and accelerated to 3.5 GeV by the succeeding LINAC before injecting into the LER. The e^+e^- separator filters

the electrons from the tungsten target and stops them using a beam stopper.

The e^+e^- beams collide at the IP in Tsukuba Hall at a finite crossing angle of ± 11 mrad to avoid the parasitic collisions due to closely spaced multiple bunches [34]. In contrast to the head-on collision, it does not require separation magnets, which further suppress the background from synchrotron radiations. Two superconducting radio frequency cavities known as crab cavities, first proposed in 1989 [35, 36], were installed in January 2007 to overcome the loss in instantaneous luminosity due to the finite crossing angle. The crab cavities kick the electron-positron bunches in the horizontal plane to overlap at the IP head-on. KEKB surpassed the designed instantaneous luminosity of 1×10^{34} cm^{-2}s^{-1} in 2003, and set a world record of 2.11×10^{34} cm^{-2}s^{-1} in 2009.

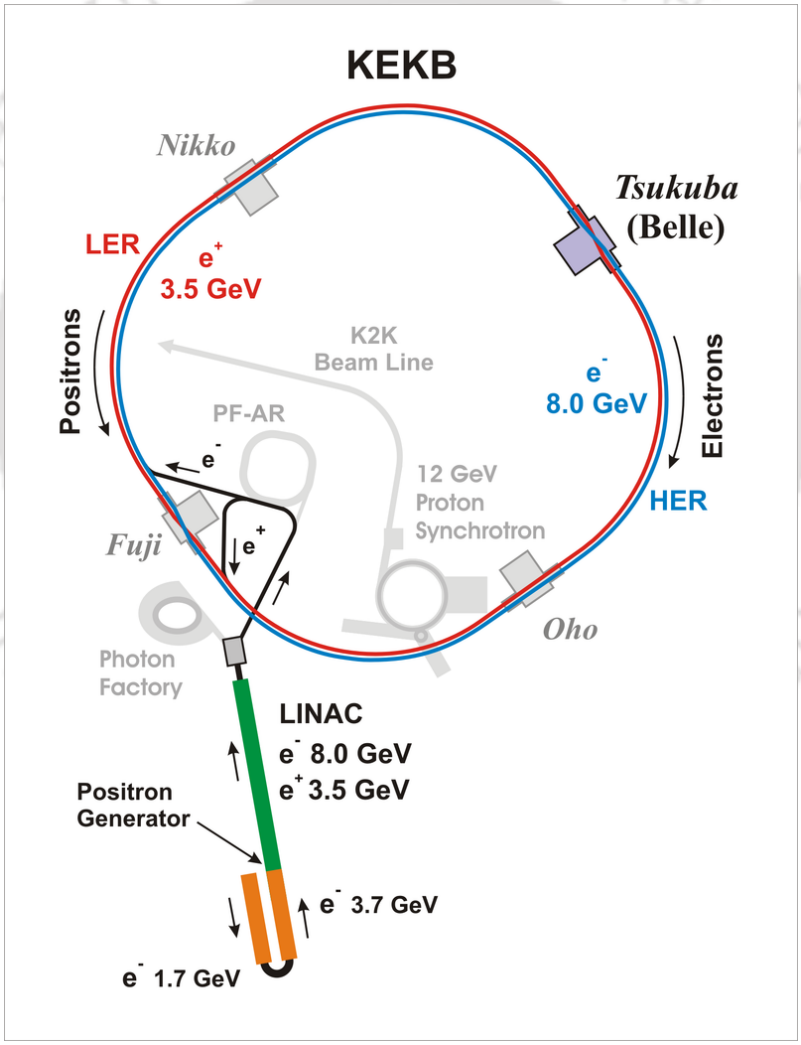

Figure 2.1: Schematic layout of KEKB accelerator.

The center of mass (CM) energy of the beams at the IP is given by

$$\begin{aligned} \sqrt{s} &= \sqrt{2E_{\mathrm{H}}E_{\mathrm{L}}(1+\cos\phi)} \\ &\approx 2\sqrt{E_{\mathrm{H}}E_{\mathrm{L}}} \end{aligned}, \tag{2.1}$$

where, ϕ is the finite crossing-angle of the beams at the IP, and $E_{\rm H}$ and $E_{\rm L}$ are the lab-frame beam energies of the HER and LER. The CM energy is scanned through the various $\Upsilon(nS)$ resonances (with n = = 1, 2, 3, 4, and 5) having masses in the range of 9-11 GeV/c^2, where the first three (next two) states are bound (quasi-bound) states of $b\bar{b}$ system with the mean lifetime of order $10^{-21}(10^{-24})$ seconds. Figure 2.2 shows the hadronic cross-section of e^+e^- as a CM energy function. The top right figure shows the cross-section normalized to the $\sigma(e^+e^- \to \mu^+\mu^-)$ above the CM energy of 10.5 GeV, where three more resonances known as $\Upsilon(4S), \Upsilon(5S),$ and $\Upsilon(6S)$ can be seen.

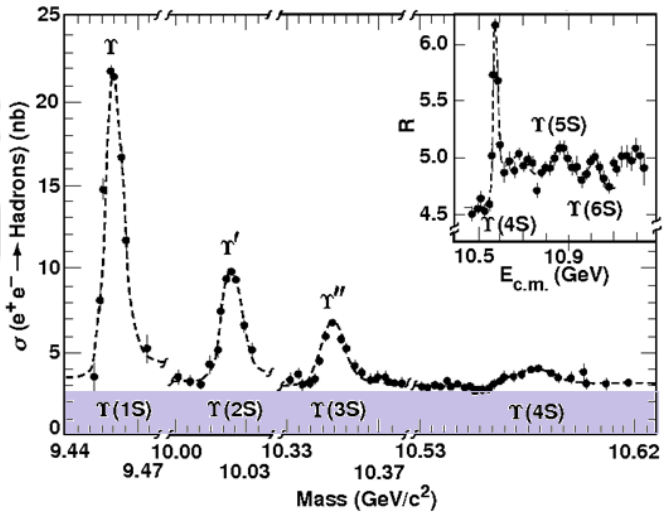

Figure 2.2: The hadronic cross-section of the $\Upsilon(nS)$ resonances as a function of the e^+e^- CM energy; Top right box shows the cross-section ratio of hadronic to the theoretical $e^+e^- \to \mu^+\mu^-$ above the $\Upsilon(3S)$ resonance.

Belle experiment has collected the total integrated luminosities of 711 fb^{-1} and 121.4 fb^{-1} data at $\Upsilon(4S)$ and $\Upsilon(5S)$ resonances, respectively. The CM energy of 10.579 GeV at $\Upsilon(4S)$ resonance is a few MeV above the $B\bar{B}$ ($m_B = 5.279$ GeV/c^2) production threshold; $B\bar{B}$ mesons are produced at rest in the CM frame. Asymmetric energy in the HER and LER boosts the CM in the forward (electron beam) direction by the Lorentz boost of

$$\beta\gamma = \frac{E_{\rm L} - E_{\rm H}}{E_{\rm CM}} = 0.425. \tag{2.2}$$

The mean lifetime of a B meson is of order 1.5 ps. Lorentz boost increases the mean distance between two B decay vertices to 200 μm, which is large enough to be resolved using the silicon vertex detector of resolution 100 μm. Thus, the boost in the forward direction infers the time difference between the two decay vertices as:

$$\Delta t = \frac{\Delta z}{\beta\gamma c}, \tag{2.3}$$

allowing us to perform the time-dependent CP violation measurements.

$\Upsilon(5S)$ resonance is the 4$^{\text{th}}$ excited state of the $b\bar{b}$ system with a J^{PC} value of 1^{--} and rest mass energy of 10.885 GeV/c^2. Figure 2.3 shows the classification of hadronic events from the e^+e^- collisions at a CM energy of $\Upsilon(5S)$ resonance, which is categorized into types: (a) $u\bar{u}$, $d\bar{d}$, $s\bar{s}$, $c\bar{c}$ continuum, (b) $b\bar{b}$ continuum, and (c) $\Upsilon(5S)$ resonance. The events from the $b\bar{b}$ continuum and $\Upsilon(5S)$ are treated together as $b\bar{b}$ since the source of B and B_s^0 mesons in the final state cannot be topologically separated. The cross-section $\sigma_{b\bar{b}}^{\Upsilon(5S)}$ for the $e^+e^- \to b\bar{b}$ events at $\Upsilon(5S)$ resonance is measured to be 0.340 ± 0.016 nb using 121.4 fb^{-1} of data [37]. The CM energy at $\Upsilon(5S)$ resonance is marginally above the threshold production of $B_s^0\bar{B}_s^0$ ($m_{B_s^0} = 5.367$ GeV/c^2) mesons and can produce the B_s^0 meson pairs in three kinematical combinations: $B_s^0\bar{B}_s^0$, $B_s^0\bar{B}_s^{0*}$ or $B_s^{0*}\bar{B}_s^0$, and $B_s^{0*}\bar{B}_s^{0*}$. Figure 2.4 shows the leading order Feynman diagram for the production of $B_{(s)}\bar{B}_{(s)}$ mesons from the e^+e^- annihilation at $\Upsilon(5S)$ resonance. The fraction $\left(f_s = \frac{\sigma(e^+e^- \to B_s^{0(*)}\bar{B}_s^{0(*)})}{\sigma(e^+e^- \to b\bar{b})}\right)$ of $b\bar{b}$ events decaying into $B_s^{0(*)}\bar{B}_s^{0(*)}$ is measured using the inclusive $D_s^{\pm}$ production to be $\left(22.0^{+2.0}_{-2.1}\right)$ % [38]. Non-hadronic processes with large cross-sections such as $e^+e^- \to e^+e^-$, $\mu^+\mu^-$, $\tau^+\tau^-$, $e^+e^+e^-e^-$, $\gamma\gamma$, and $\gamma\gamma X$ are not shown in the classification.

The relative abundance of the three $B_s^{0(*)}\bar{B}_s^{0(*)}$ states measured using $B_s^0 \to D_s\pi$ decays [37] are as follows:

$$f_{B_s^{0*}\bar{B}_s^{0*}} = \frac{\sigma(e^+e^- \to B_s^{0*}\bar{B}_s^{0*})}{\sigma(e^+e^- \to B_s^{0(*)}\bar{B}_s^{0(*)})} = (87.0 \pm 1.7)\,\% \tag{2.4}$$

$$f_{B_s^0\bar{B}_s^{0*}} = \frac{\sigma(e^+e^- \to B_s^0\bar{B}_s^{0*})}{\sigma(e^+e^- \to B_s^{0(*)}\bar{B}_s^{0(*)})} = (7.3 \pm 1.4)\,\% \tag{2.5}$$

$$f_{B_s^0\bar{B}_s^0} = 1 - f_{B_s^{0*}\bar{B}_s^{0*}} - f_{B_s^0\bar{B}_s^{0*}}. \tag{2.6}$$

Exotic B_s^0 meson decays via $B_s^{0*} \to B_s^0\gamma$ approximately 100% of the times. The number of B_s^0 or $\bar{B}_s^0$ events can be computed from the equation:

$$N(B_s^0) = 2 \times \mathcal{L}_{\text{int}}^{\Upsilon(5S)} \times \sigma_{b\bar{b}}^{\Upsilon(5S)} \times f_s, \tag{2.7}$$

where, $\mathcal{L}_{\text{int}}^{\Upsilon(5S)} = 121.4 \pm 1.6$ fb^{-1} is the total integrated luminosity; $\sigma_{b\bar{b}}^{\Upsilon(5S)}$ is the $b\bar{b}$ production cross-section at $\Upsilon(5S)$ resonance; and f_s is the $B_s^{0(*)}\bar{B}_s^{0(*)}$ production fraction of $b\bar{b}$ events. The Belle detector, discussed in the next section, has accumulated $(18.16^{+1.87}_{-1.95}) \times 10^6$ number of $B_s^0\bar{B}_s^0$ events using the total integrated luminosity at $\Upsilon(5S)$ resonance.

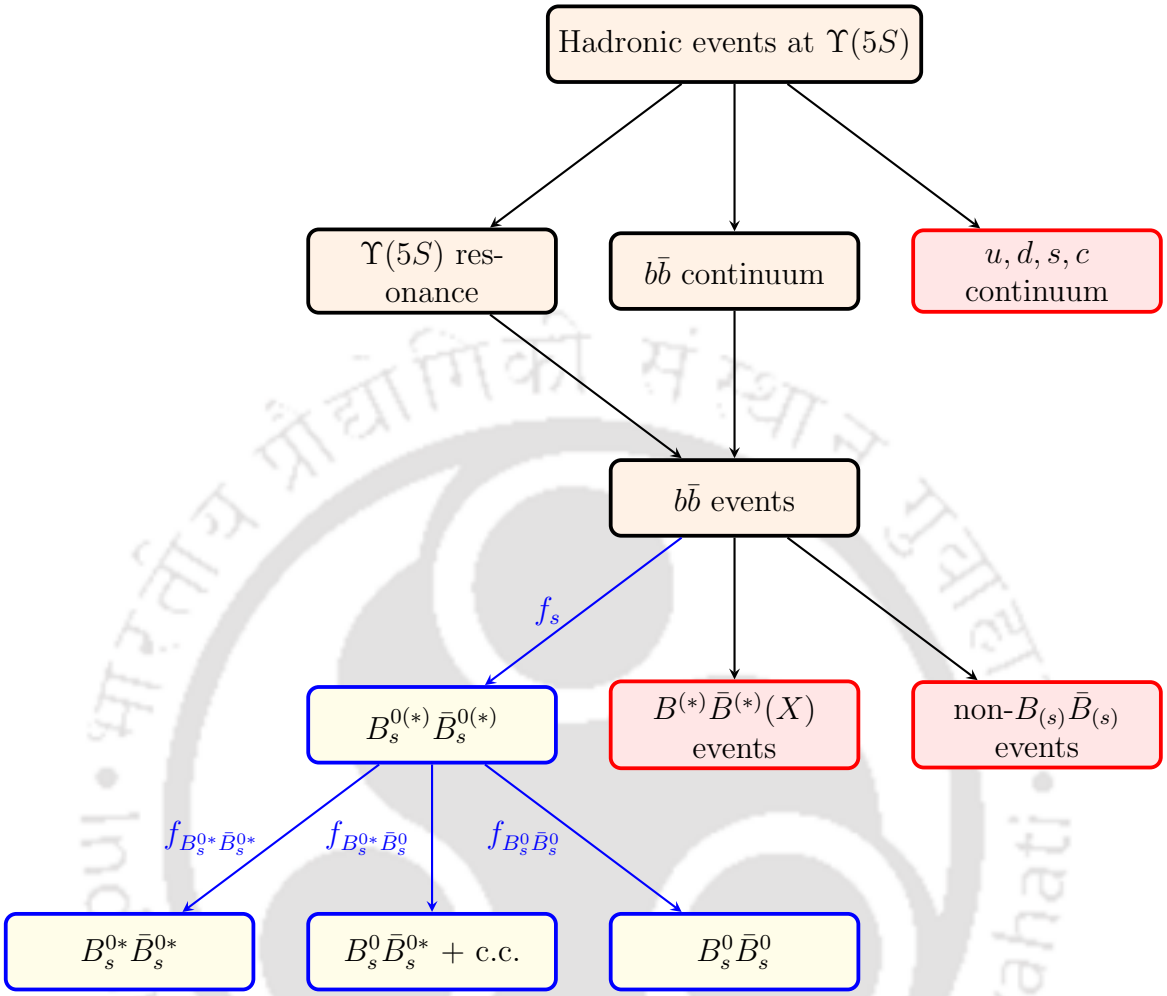

Figure 2.3: Classification of the hadronic events produced in the e^+e^- collisions at the CM energy close to the $\Upsilon(5S)$ peak position.

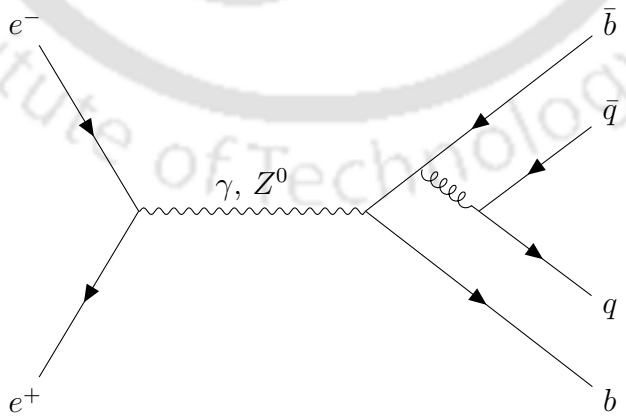

Figure 2.4: Leading order Feynman diagram for $e^+e^- \to B_{(s)}\bar{B}_{(s)}$ at $\Upsilon(5S)$ resonance.

2.3 The Belle Detector

Belle detector is a cylindrical large-solid-angle magnetic spectrometer located in Tsukuba Hall. The geometrical center of the detector is displaced from the IP in the forward direction to match the CM boost of the electron-positron collider. B-mesons, τ-leptons, and other short-lived particles produced in e^+e^- collisions decay into relatively stable particles in the final states, for example, charged pions, kaons, protons, muons, electrons, γ, etc., which induce signals through the excitation and loss energy in the various sub-detectors. The Belle detector measures the momentum and energy deposition and provides the particle ID (PID) to identify the final state particles. Figure 2.5 shows an overview of the Belle detector, which is a schematic arrangement of the following sub-detectors:

1. Silicon Vertex Detector (SVD)
2. Central Drift Chamber (CDC)
3. Aerogel Cherenkov Counter (ACC)
4. Time-of-Flight scintillation counter (TOF)
5. Electromagnetic Calorimeter (ECL)
6. K_L^0 and μ detector (KLM)
7. Extreme Forward Calorimeter (EFC)

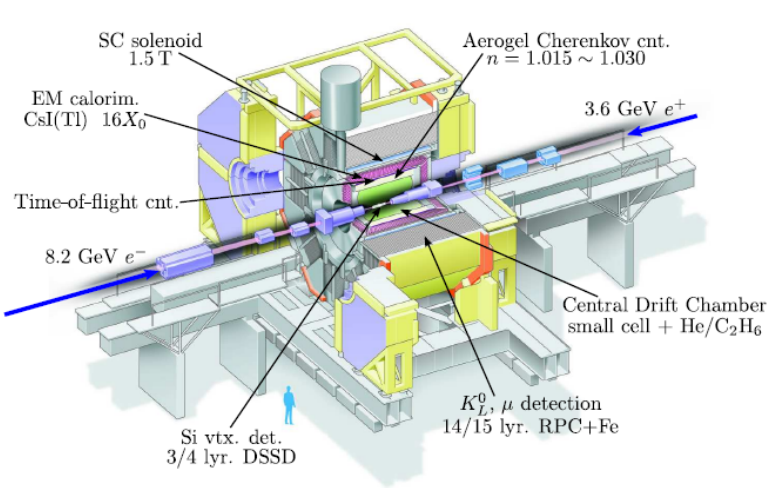

Figure 2.5: An overview of the Belle Detector.

Sub-detectors are supported by a supper-conducting hexagonal shaped iron structure which acts as a solenoid and provides a uniform magnetic field of strength 1.5 T. Detectors except the KLM are housed inside the solenoid. SVD provides the decay vertices and can also track the low-momentum charged particles. CDC is a tracking

detector for charged particles. ACC and TOF, situated radially outward of the CDC, provide the PID for the charged particles. An array of Thalium doped CsI(Th) crystals in the ECL detects the electromagnetic showers. Muons and K_L-mesons are detected outside the solenoid coil using an array of glass-resistive plate counters interspersed with iron sheets. An array of bismuth germanate oxide (BGO) crystals in the extreme forward and backward of the beam directions shields the detector from the beam-related radiations and measures the online luminosity.

The Belle experiment uses the Cartesian coordinate system with an origin at the IP. The z-axis points in the direction opposite to the positron beam, the x-axis radially outward to the storage ring, and the y-axis vertically upward. For the spherical coordinate system, θ and ϕ are the conventional polar and azimuthal angles.

The detector is divided into three sections: barrel region parallel to the beam axis with a polar angle coverage of $34° < \theta < 127°$; forward and backward endcaps, extended radially from $17° < \theta < 34°$ and $127° < \theta < 150°$, respectively. Following subsections briefly discuss the Belle detector components, where a detailed description is given somewhere else in [2].

2.3.1 Beam Pipe

The beam pipe is the innermost component of the Belle detector enclosing the IP. The resolution for the charged tracks vertex measurements improves inversely with the distance of SVD's first layer from the IP; therefore, the beam pipe is made of two thin (of thickness 5 mm) beryllium cylinders having small inner radii of 20 mm and 23 mm. Cylinders are placed coaxially with an annular gap of 2.5 mm. Figure 2.6 shows the schematic for the beryllium beam pipe cross-section at the IP. The first layer of SVD is installed very close to the beam pipe. A low Z material (Be) is used for the pipe as the coulomb scattering of the charged particles limits the B-decay vertices measurement. Helium (He) is passed through the gap between the inner and outer walls to shield the SVD from beam-induced heating. A 20 μm thick gold sheet covered the outer cylinder to block the low-energy X-rays from the high-

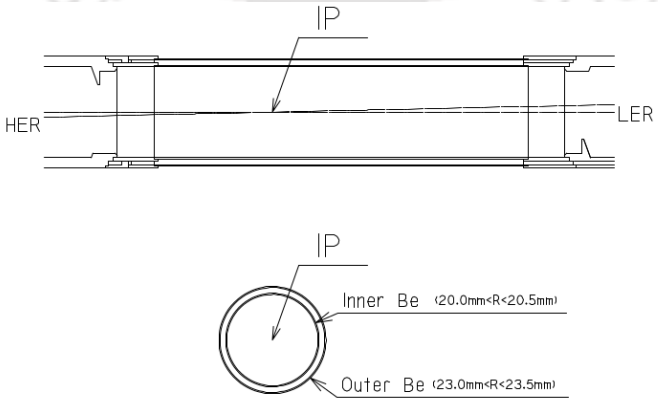

Figure 2.6: The cross-section of the beryllium beam pipe at the IP [2].

energy ring. The beam pipe replacement in 2003 [39] to install another SVD (SVD2) configuration reduced the inner radii of concentric Be cylinders. SVD2 uses the Be cylinders of 15 mm (0.6 mm thick) and 16.1 mm (0.35 mm thick) inner radii. The thickness of the coated gold foil to the outer cylinder is reduced to 10 μm. Liquid paraffin is circulated as a coolant through the 0.5 mm gap between the cylinders.

2.3.2 Silicon Vertex Detector

The silicon vertex detector is the innermost sub-detector dedicated to determining the origin of the charged particle tracks. To perform the time-dependent CP-violation study, the Belle experiment requires precisely measuring the $B\bar{B}$ decay z-positions separated by an average flight length of 200 μm. SVD can measure the z-position of B-decays with a precision of 100 μm. Further, SVD improves the momentum resolution for the low-momentum charged particles.

Belle's experiment used two SVD configurations during the entire run period: three (SVD1) and four (SVD2 installed in the summer of 2003 alongside the new beam pipe) layers of concentric cylindrical structures along the beam axis. Each layer is constructed from independent ladders comprised of double-sided silicon strip detectors (DSSDs). A DSSD is essentially a reverse-biased PN junction diode. A passing charged particle generates the electron-hole pairs in the depletion region, collected separately at the orthogonal p^+ and n^+ sense strips. p^+ and n^+ strips are aligned along the z-axis and ϕ-axis to measure the ϕ and z-positions of the SVD hits. The layer number of the charged track hit infers the radial distance from the beam axis. This analysis uses the data collected with the SVD2 detector [40, 41], shown in Figure 2.7. The radii of the four concentric cylindrical layers are 20, 43.5, 70, and 88 mm. Four layers have 6, 12, 18, and 18 ladders, consisting of 2, 3, 5, and 6 DSSDs, respectively. Each DSSD has 1280 sense strips of size 57.5×33.5 mm^2 and 640 read-out pads on each side. SVD2 covers the polar angle $17° < \theta < 150°$, which matches the geometrical acceptance of the tracking detector discussed in the next section. In contrast, three layers of SVD1 of radii 30.0, 45.5, and 60.5 mm covered relatively small polar angler $23° < \theta < 139°$.

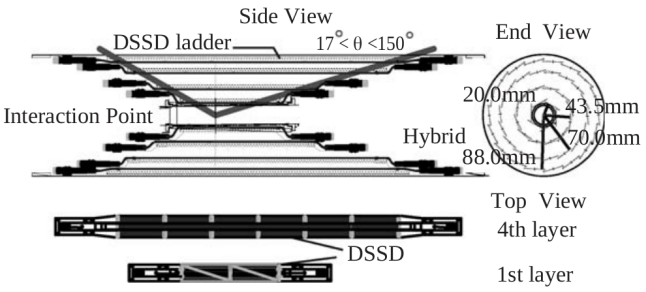

Figure 2.7: Schematic layout of the SVD2 [2].

2.3.3 Central Drift Chamber

Charged particles tracking detector, central drift chamber (CDC), is an asymmetric cylindrical drift wire chamber around the beam pipe covering the polar angle $17° < \theta < 150°$. The chamber has 50 cylindrical layers of anode wires, consisting of 32 axial layers aligned along the z-axis and 18 stereo layers with wires slanted by a slight angle of approximately 50 mrad. Eight aluminum field wires of 126 μm diameter surround a 30 μm in diameter gold-plated tungsten (sense) wire forming a drift cell. The field and sense wires are applied with negative and positive potentials. The cells provide a typical drift distance of 8-10 mm, where the cell structure is shown in Figure 2.8 (left). The chamber is filled with a mixture of low Z (equal proportion of ethane (C_2H_6) and helium) gas to minimize the impact of Coulomb scattering on momentum resolution. A passing charged particle ionizes the gas by freeing the electron and loses its energy. Primary electrons accelerate under the influence of an electric field, producing an avalanche of charges as a signal pulse at the sense wire. However, the pulse height is directly proportional to the number of primary electrons, which in turn to the energy loss by the charged particle. Thus, by measuring the pulse heights, the energy loss of a charged particle is deduced. A combination of axial and stereo-layer signals infer the z-coordinates of the hits. In contrast, the z-position measuring for the inner layer is improved using cathode strips because of the small drift cell size. The cathode strips are divided into eight segments of width 7.4 mm in the ϕ-direction and have an 8.2 mm pitch in the z-direction. Figure 2.8 (right) shows the cathode strip and wire configuration of the inner layers. An overview of the CDC structure is shown in Figure 2.9. CDC is housed in a solenoidal magnetic field of strength 1.5 T to bend the charged particles in a helical trajectory. Tracks are reconstructed from the induced signals (hits) in the cathode

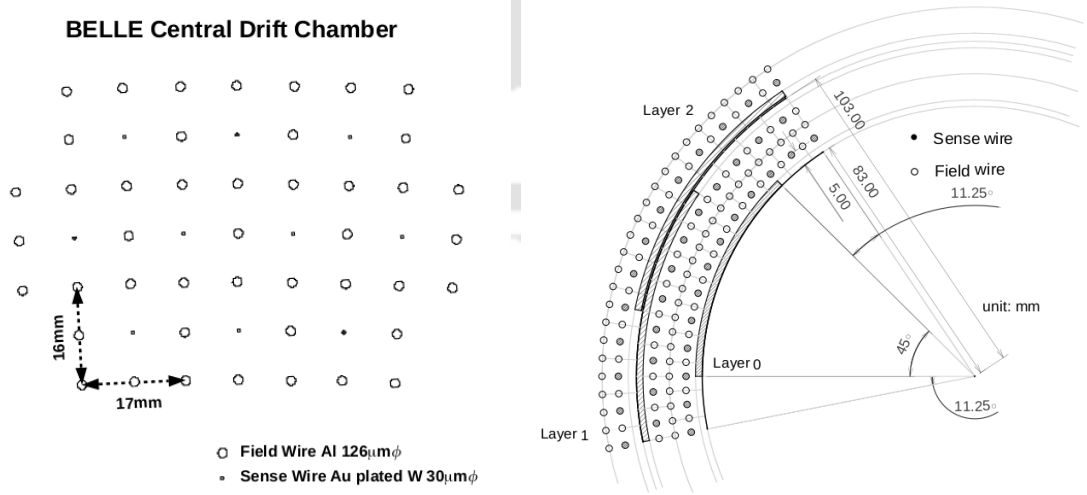

(a) (b)

Figure 2.8: (a) Cell structure of CDC and (b) cathode sector and wire configuration for the inner layers [2].

strip and anode wire layers to determine the signed curvature and pitch of the helix. The pivot point is assumed to be the hit in the innermost cathode strip. Signed-curvature provides charge and transverse momentum ($p_t = \sqrt{p_x^2 + p_y^2}$), whereas the longitudinal momentum (p_z) of the particle is proportional to the pitch. CDC has achieved the momentum resolution required for the physics goal of the experiment of $\frac{p_t}{\sigma_{p_t}} \sim 0.005\sqrt{1+p_t^2}$ for all the charged tracks having $p_t > 100$ MeV/c^2.

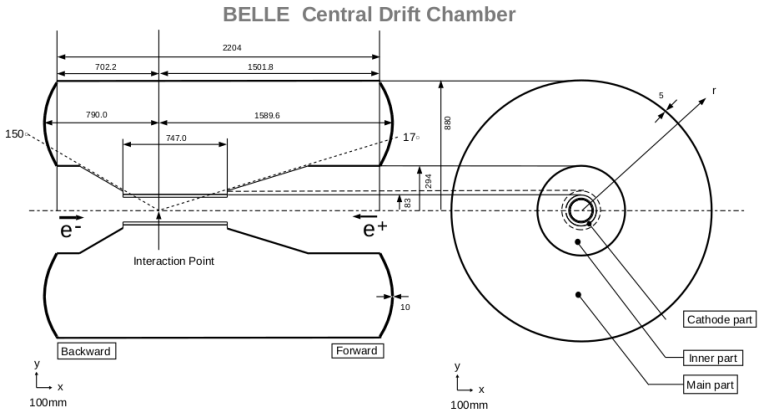

Figure 2.9: Overview of the CDC structure with lengths in units of mm.

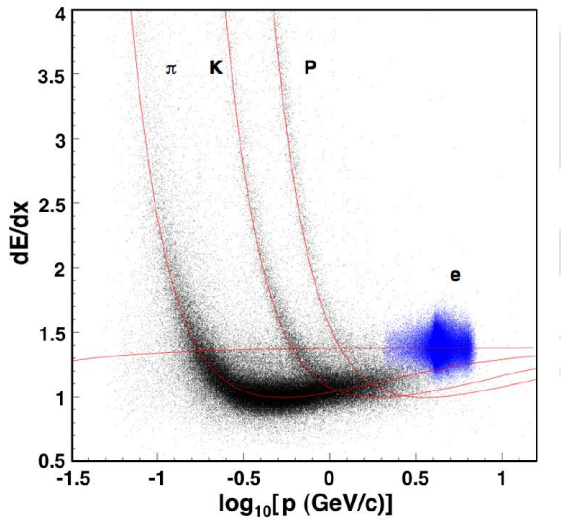

Figure 2.10: Scattered plot of the $\langle dE/dx \rangle$ (keV/cm) versus $\log_{10}[p(\text{GeV}/c)]$ of the charged particles observed in the collision data.

A charged particle's energy loss per unit length (dE/dx) is crucial for the PID. Bethe-Bloch equation gives the ionization energy loss per unit length for a charged particle traversing a medium with velocity $v = \beta c$, as [3]:

$$\frac{dE}{dx} \approx -4\pi\hbar^2 c^2 \alpha^2 \frac{nZ}{m_e v^2} \left\{ \ln\left[\frac{2\beta^2\gamma^2 c^2 m_e}{I_e}\right] - \beta^2 \right\}, \tag{2.8}$$

where Z and n are the atomic number and number density of the medium, $\hbar$ is the reduced Planck's constant, α is the fine-structure constant, m_e is the mass of the electron, c is the speed of the light, $\gamma = \frac{1}{\sqrt{1-\beta^2}}$ is the Lorentz factor, and I_e is the effective ionization potential of the material averaged over all atomic electrons. The energy loss for a given medium of specific number density depends on the velocity of the traversing charged particle. Therefore, the charged particles of different masses have distinctive dE/dx for the given momentum, as shown in the scattered plot of measured $\langle dE/dx \rangle$ versus momentum of the charged particle in figure 2.10. CDC provides a good separation ID based on $\langle dE/dx \rangle$ for the charged π and K of momentum less than 0.8 GeV/c.

2.3.4 Aerogel Cherenkov Counter

Aerogel Cherenkov Counter (ACC), comprised of the silica aerogel arrays, is a scintillation counter. A passing charged particle's electric field polarises the dielectric medium. For the velocity of charged particle greater than the speed of light in that medium, $\beta > 1/n$ where n is the refractive index, the spherical wavefronts originated from the unpolarization of the medium interfere constructively producing a light cone, known as the Cherenkov radiations [42]. The requirement on the threshold velocity imposes an applicable condition on the mass of the charged particle of momentum p,

$$mc < (n^2 - 1)^{\frac{1}{2}} p. \tag{2.9}$$

ACC utilizes this condition to separate the charged K and π tracks.

The barrel part of the ACC consists of 960 silica aerogel modules segmented in 60×16 cells in the $\phi - z$ directions. At the same time, the forward end-cap of the detector has 228 modules arranged in 5 concentric layers. ACC covers a polar angle $17° < \theta < 127°$, as shown in Figure 2.11. The refractive index (n) of the aerogels ranges from 1.010 to 1.030 to cover the momentum dependency of the charged particle on the polar angle. Charged pions but not the kaons emit the Cherenkov radiations for the given configuration in the momentum range of $1.2 < p < 3.5$ GeV/c.

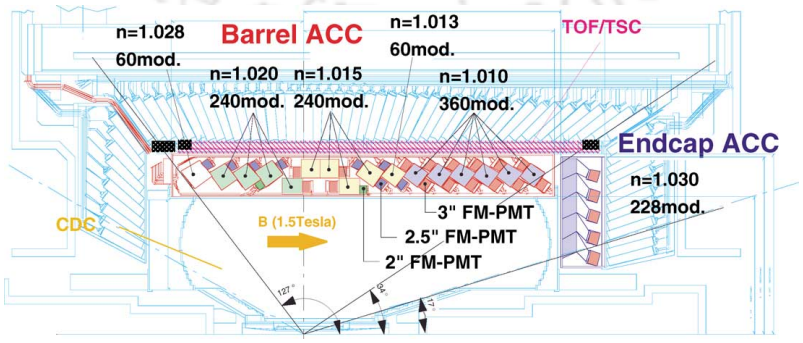

Figure 2.11: A schematic layout of the ACC

ACC modules have dimensions of $12 \times 12 \times 12$ cm^3. The counter modules consist of five layers of silica aerogel tiles stacked in a thin aluminum box in the barrel part and carbon-fiber-reinforced polymer (CFRP) in the forward end-cap of ACC. The inner surface of the boxes is lined with diffusive reflector (Gerotex) sheets for a better collection of light. Emitted Cherenkov light in the module is fed to light guides and detected by one or two fine-mesh photomultiplier tubes (FM-PMTs) attached to the boxes. Figure 2.12 shows the typical ACC module design in the barrel and forward end-cap of the detector.

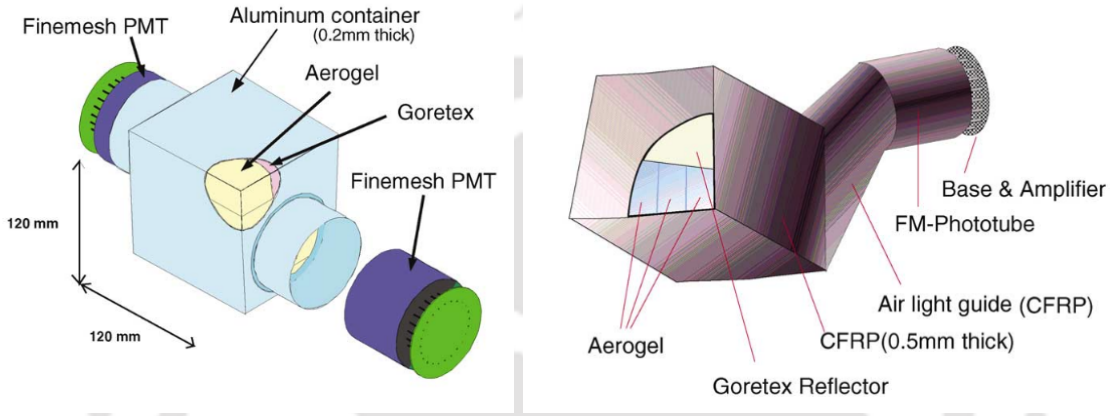

(a) (b)

Figure 2.12: Counter module design in the (a) barrel and (b) forward end-cap of the ACC.

2.3.5 Time-of-Flight Counter

The Time-of-flight detector (TOF) is a plastic scintillation detector providing the arrival timing information of a charged particle with a time resolution of 100 ps. It consists of 64 modules segmented in the ϕ-direction at 1.2 m radial distance from the IP and covers a polar angle range $34° < \theta < 120°$. Each module has two trapezoidal-shaped TOF counters and one thin trigger scintillation counter (TSC), where TSC provides the fast trigger signals at a manageable rate of below 70 kHz. TSC and TOF counters are placed radially outward with a 1.5 cm gap to block the created electron-positrons in the TSC layer from entering the TOF counters under a 1.5 T magnetic field. Each TOF and TSC are read out by an FM-PMT attached at the end and sides of the plastic scintillators. Figure 2.13 shows the schematic of the TOF module.

Measuring the flight length L and momentum (p) from CDC and SVD, and flight time T from IP to TOF, charged particle mass is calculated from the special relativity as:

$$m = \frac{p}{c}\sqrt{\frac{c^2\mathrm{T}^2}{\mathrm{L}^2} - 1}. \tag{2.10}$$

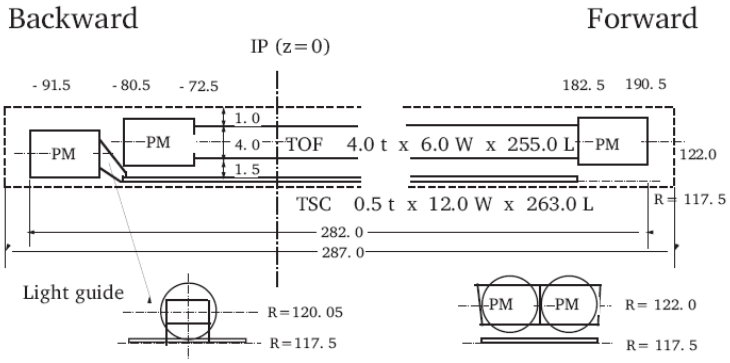

Figure 2.13: Schematic layout of the TOF module.

Figure 2.14 shows the mass distribution with distinctive peaks of hadronic tracks for $p < 1.2$ GeV/c from the TOF measurements. Black points represent the collision data in agreement with Monte Carlo (MC) predictions (histogram), assuming a time resolution of 100 ps for the MC data. TOF provides a good separation ID for π, K, and p ID in the momentum range $0.8 < p < 1.2$ GeV/c. TOF is discussed in further detail in [2].

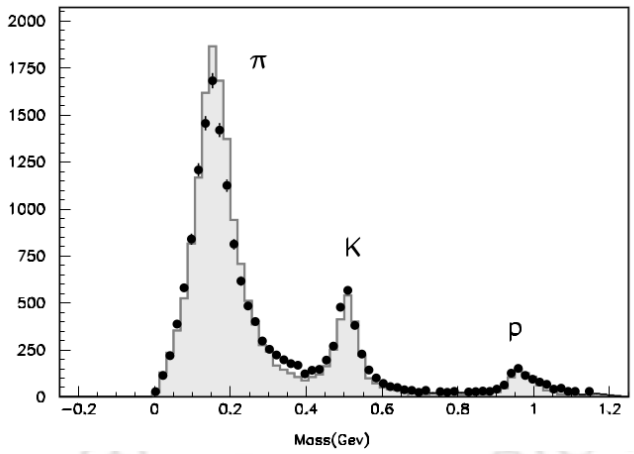

Figure 2.14: Mass distribution from the TOF measurements of the charged particles of momentum $p < 1.2$ GeV/c.

2.3.6 Electromagnetic Calorimeter

An electromagnetic calorimeter (ECL) measures the energy deposition of charged particles and photons through their electromagnetic interactions with the material. Photon produces the electron-positron pair under the influence of nuclear charge, which emits the bremsstrahlung (German for braking radiation) through electromagnetic interactions followed by the pair production. Thus, subsequent processes produce a cascade of electron-positron pairs (electromagnetic shower), depositing

the energy through excitation and ionization in the ECL. The photon yield, proportional to the deposited energy of the electromagnetic shower, is measured using silicon photo-diodes.

Final state particles in e^+e^- collision at KEKB cover a wide energy spectrum; photons from the end products of cascade decay have energy less than 500 MeV, important two body B-meson decays, e.g., $B \to K^*\gamma$ and $B \to \pi^0\pi^0$, produce photons up to an energy of 4 GeV, and Bhabha scattering has end products of energy up to 8 GeV. Further, neutral pion decaying in two photons has no traces in tracking detectors. Therefore, measuring the opening angle for highly energetic pion decay requires a good spatial and energy resolution for a long energy range. For that, thallium doped CsI tower-shaped crystals are arranged around the beam axes in three sections of ECL: forward endcap consisted of 1152 crystals covers the polar angle $12.4° < \theta < 31.4°$, 6624 crystals in the barrel section covers polar angle $32.2° < 128.7°$, and backward endcap section has 960 crystals extending the polar range to $130.7° < \theta < 155.1°$. The cross-section of the crystal varies with the polar angle. A typical crystal in the barrel region have front and rear face of dimensions 55×55 mm^2 and 65×65 mm^2, and of 30 cm in length (approximately 16.2 radiation length) to avoid the energy resolution degradation due to the shower leakage fluctuations out of counter rear at high energies. The barrel section has a length of 3m placed asymmetrically with forward and backward endcap sections at 2m and -1m from the IP. Figure 2.15 shows the ECL configuration. Each crystal has a pair of silicon PIN photodiodes and a preamplifier mounted at the end to read out the scintillation light.

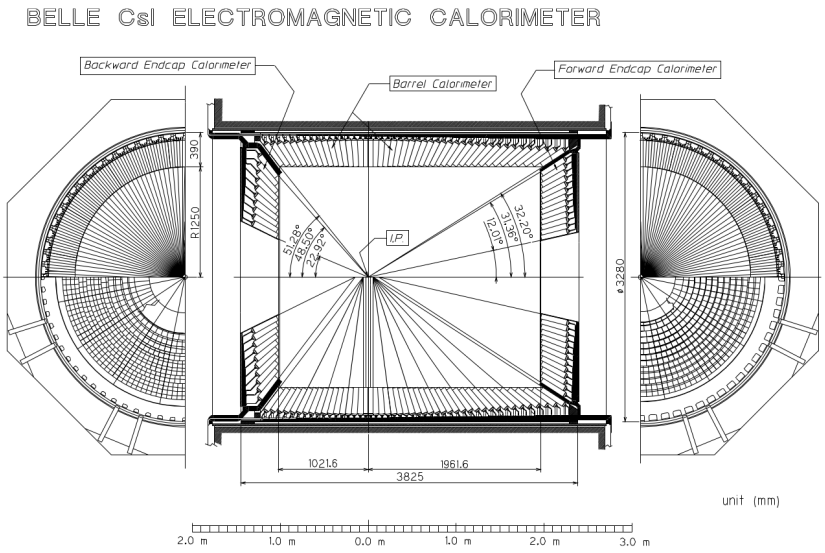

Figure 2.15: A schematic showing the ECL configuration [2]

ECL covers the angular region similar to CDC; the electromagnetic showers of charged particles can be distinguished from an associated track in CDC. In contrast, a photon has no tracking information. Bremsstrahlung energy loss depends inversely

proportional to the mass of the charged particle; energy loss for muons is suppressed by $(m_e/m_\mu)^2$; therefore, they can lose energy through ionization. Charged pions and kaons produce a widely spread cascade of particles through strong interactions with the ECL material. Therefore, electromagnetic showers from the electrons and photons are identified from other charged particles based on the tracking information from CDC, E/p ratio where E is the measured energy in ECL and p is the momentum of the charged particle, the transverse spread of the shower, and the light yield in ACC. Energy resolution using 3×3 arrays of ECL crystal as a function of incident photon energy is given by

$$\frac{\sigma_E}{E}(\%) = \left(\frac{0.066}{E}\right)^2 + \left(\frac{0.81^{\,2}}{\sqrt[4]{E}}\right) + 1.34^2, \tag{2.11}$$

where E is the measured energy in GeV. The first term corresponds to the electronic noise, whereas the second and third terms incorporate the shower leakage fluctuations and systematic effects, such as uncertainty from the crystal calibration. The spatial resolution of the ECL is given by

$$\sigma_{\text{position}} = \left(0.27 + \frac{3.4}{\sqrt{E}} + \frac{1.8}{\sqrt[4]{E}}\right) \text{ mm}. \tag{2.12}$$

The ECL is described in detail somewhere else in [2] and [43].

2.3.7 Extreme Forward Calorimeter

Few physics studies, for example, $B \to \tau\nu$, requires the extended calorimeter for the e/γ detection in addition to ECL, $12.4° < \theta < 155.1°$. Further, beam radiation background exposure of the detector can deteriorate the CDC and other components. Therefore, an extreme-forward calorimeter (EFC) consisting of bismuth germanate ($Bi_4Ge_3O_{12}$ or BGO) crystals is installed in the forward ($6.4° < \theta < 11.5°$) and backward ($163.3° < \theta < 171.2°$) sections. BGO crystals are chosen due to their high radiation tolerance of Mrad, short radiation length (1.12 cm), and excellent energy resolution of $\frac{(0.3-1.0)\%}{\sqrt{E(\text{GeV})}}$. BGO crystals are housed in a bucket-shaped 1 mm thick stainless steel container. Each section of EFC is segmented into 32 (azimuthal) and 5 (polar) divisions for a better position resolution of the electromagnetic showers. An isometric view of the EFC sections is shown in Figure 2.16.

EFC provides the KEKB luminosity measurement and beam monitoring in addition to the beam radiation mask for the CDC detector. Further details of the EFC can be found in [2] and [44].

2.3.8 Superconducting solenoid

Sub-detectors discussed so far are housed in a superconducting solenoid providing a magnetic field of strength 1.5 T along the z-axis. It helps CDC in determining the momenta and sign of the charged particles. Solenoid is constructed from a

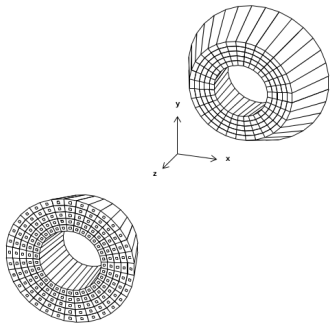

Figure 2.16: BGO crystal arrangement in the forward and backward EFC [2]

single layer of Niobium-Titanium-copper around a highly pure (99.99%) aluminium cylinder of 4.4 m in length and 3.4 m in diameter. The solenoid is cooled to 4.5 K by liquid helium circulation through the cooling tube on the inner surface of the aluminium cylinder. The coil is surrounded by a thick iron structure serving as the return path of the magnetic flux and an absorbent for the neutral K_L and muons to be identified in the next detector.

2.3.9 K_{L} and Muon Detector

The K_{L} and muon (KLM) detector situated outside the superconducting solenoid detects the relatively long-lived neutral K_{L} and muons with high efficiency for a momentum range greater than 600 MeV/c. It uses the superlayers of two glass-resistive plate chambers (RPCs) surrounded by orthogonal cathode strips in θ and ϕ directions, determining the traversing charged particle(s) space points, as shown in Figure 2.17. Each RPC consists of two parallel plate electrodes with high bulk resistivity ($\geq 10^{10}\Omega$ cm) separated by a gas-filled gap. A non-flammable gaseous mixture of argon (30%), butane-silver (8%), and hydrofluorocarbon (HFC-134a (62%)) is used for a stable operation of the RPC. A passing charged particle ionizes the gas initiating a stream of local discharge, which induces a signal on the pick-up strips. The discharge is limited by the high resistivity of the plates and quenching properties of the gas.

KLM has two sections: barrel section covering the polar angle $45^\circ < \theta < 125^\circ$ and forward-backward endcaps extending the angular region to $20^\circ < \theta < 155^\circ$. Alternatively, 15 RPC layers and 4.7 cm thick 14 iron sheets construct the octagonal-shaped barrel section, whereas 14 RPC layers comprise the forward and backward endcaps. Iron sheets in the barrel section provide a total of 3.9 nuclear interaction lengths normal to the detector planes for K_{L}'s converting through the strong interaction, where a nuclear interaction length is the mean distance traveled by a hadron before inelastic nuclear interaction. Interaction of the hadrons with ECL material is another source of 0.8 interaction length. Charged cascade from the nuclear interaction of K_{L} ionizes the gas in the particle detector and gets absorbed in the consequent iron sheets. In contrast, muon does not participate in strong interactions and penetrates deeper with small deflections by losing energy via ionization. Therefore,

transverse spread due to the nuclear scattering of hadrons and shower depth of the charged particle distinguish the muon and K_L hits. A further detailed description of the KLM detector is given in [2] and [45].

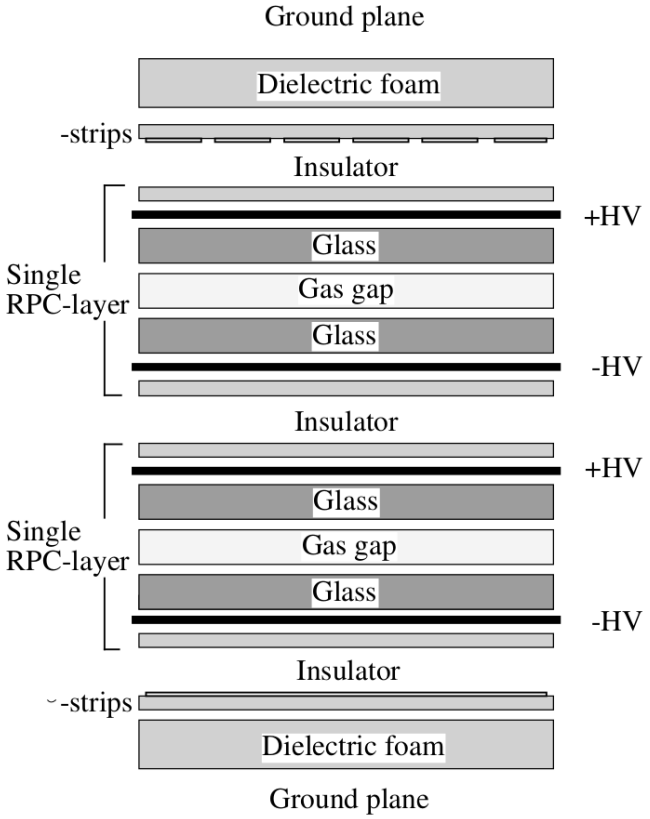

Figure 2.17: A schematic of KLM superlayer

2.4 Trigger Level and Data Acquisition System

Electron-positron collisions in the KEKB collider result in various physics processes, for example, $e^+e^- \to B\bar{B}$, $e^+e^- \to q\bar{q}$, $e^+e^- \to \tau^+\tau^-$, $e^+e^- \to \mu^+\mu^-$, $e^+e^- \to e^+e^-$ (Bhabha), $e^+e^- \to \gamma\gamma$ (di-photon), etc. Hadronic and τ events are essential for the physics analyses, whereas di-muon, Bhabha, and di-photon events have importance in the detector calibration and luminosity measurements. Apart from this, the cross-section for the beam-induced background, for example, synchrotron radiations and interaction of the beam with the residual gas in the beam pipe and with the material of the beam pipe, is significantly large. This type of background to be handled at goal luminosity of 10^{34} cm^{-2} sec^{-1} unnecessarily utilizes the data flow rate and increases the size of the data storage tapes. Therefore, hardware and software level triggers are used to reject the uninteresting events and forward the ones of physics interest with very high efficiency to the data acquisition system (DAQ) within a very short decision time. The Belle trigger system, consisting of the Level-1 (L1) hardware

trigger, Level-3 (L3) software trigger, and Level-4 (L4) software trigger, is discussed in the following sub-sections. Detail of the trigger system is given in [46]. The DAQ collects raw signal data from the sub-detectors after the L3 trigger implementation and stores them in the data storage system for offline event reconstruction and analysis.

2.4.1 Level-1 Trigger

The L1 hardware trigger system takes input from sub-detectors, excluding the SVD, based on which the Global Decision Logic (GDL), a central trigger system, decides the further processing of the raw data. Sub-detector triggers are categorized into two parts: track triggers and energy triggers. The track triggers provide information based on the CDC's $r-\phi$ and $r-z$ signal triggers. TOF/TSC trigger inputs the event timing, information on the hit multiplicity, and back-to-back event topology of the charged tracks. ECL provides the triggers based on the total energy deposition, the number of ECL clusters, and the timing of a cluster. RPC hits in KLM provide the additional trigger information for the μ tracks. Bhabha and $e^+e^- \to \gamma\gamma$ events are tagged based on the trigger information from EFC. The latency of the trigger system, defined as the time taken from the event collision to the decision-making by GDL, is set to 2.2μs to match the SVD readout system. For that, trigger information for each sub-detector is required at the input of GDL by a maximum delay of 1.85 μs. Therefore, GDL is left with a fixed time of 350 ns to process the input triggers and form the final trigger signal for each event. The L1 trigger system efficiently passes the hadronic events by more than 99%. The hardware trigger system is described in more detail in [46].

The SVD hit information is available after 25.6μs for a favorable L1 trigger decision. The Belle readout system takes a time of 50-100 μs depending upon the sub-detector occupancy for a high beam current. The level-1.5 (L1.5) [47] trigger is implemented to reject the beam-gas events in which the interaction of the charged track with SVD is far away from the nominal interaction point. Thus, the L1.5 trigger significantly decreases the readout dead time by rejecting the beam-gas backgrounds.

2.4.2 Level-3 Trigger System

The Level-3 (L3) trigger system is a software trigger implementing a fast track-finding algorithm. L3 rejects the events having no tracks with a z-impact parameter (closest point of approach to the interaction point along the beam axis) less than 5 cm and total energy deposition in ECL less than 3 GeV. These conditions select the hadronic events with high efficiency $> 99\%$ while rejecting the 50% - 60% of L1 events. Events passing the L3 trigger are saved as raw data.

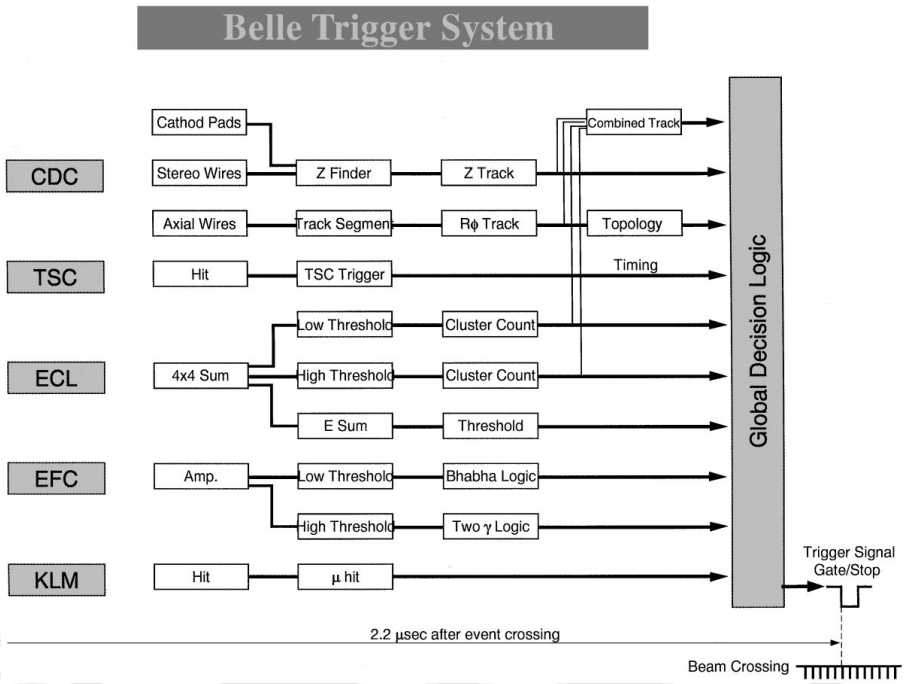

Figure 2.18: Schematic view of the Belle L1 trigger system.

2.4.3 Data Acquisition System

Events passing the L1 trigger are processed at the data acquisition system (DAQ). The DAQ system is divided into seven subsystems running in parallel to satisfy the data transfer rate of 500 Hz with a deadtime fraction of less than 10%. The charge accumulated on the capacitors as signal hits from most sub-detectors (except KLM and SVD) is converted into time pulses using a Q-to-T converter, which the TDC reads out. SVD and KLM use the flash ADC and direct TDC readout. Each subsystem handles the data from a particular sub-detector. An event builder, which adds the information chronologically, combines the data from each subsystem to construct a single event record, and its output is transferred to the online computer farm, where the L3 software trigger is employed to select the collision events. Then data is sent to the mass storage system via optical fibers at a maximum rate of 15 MB/s. An overview of the Belle DAQ is shown in Figure 2.19 and is discussed in detail in [2].

Level-4 Trigger

Level-4 (L4) offline software trigger [48] allows events with at least one good charged track, where a charged track is considered good if:

1. Transverse momentum, $|P_t| > 300$ MeV/c.

2. The closest approach of a charged track near the IP requires $|dr| < 1$ cm, and $|dz| < 4$ cm in the cylindrical coordinate system.

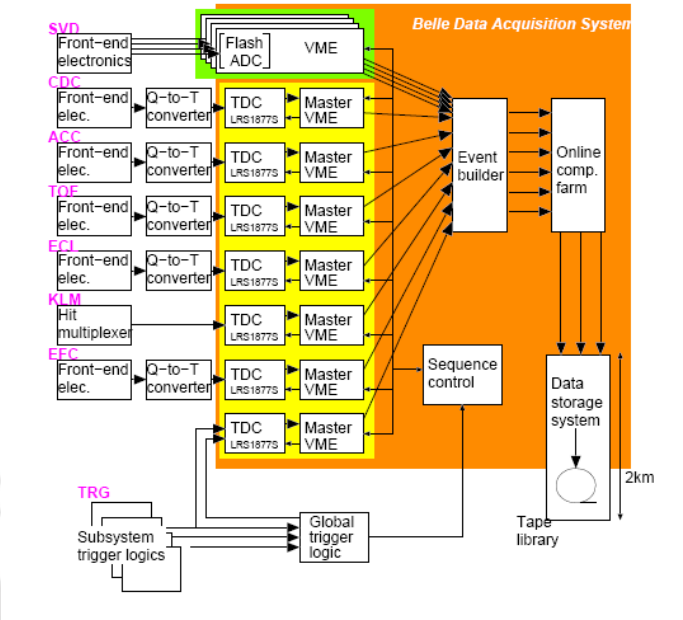

Figure 2.19: Overview of the Belle DAQ system

The Bhabha, two-photons, and low multiplicity events are saved if the additional trigger outputs are fired. The L4 trigger surpasses only 21.1% of the earlier hardware-level triggered events. Most of the rejected events constitute the beam background, thus, reducing the data storage and computational resource usage for the physics analyses. The L4 trigger is almost 100% efficient for the hadronic events. This is worth emphasizing that data rejected by the L3 trigger is recorded nowhere. In contrast, the events rejected at the L4 trigger exist in the L3 output as raw data.

2.4.4 Physics Data and the Software for Data Processing

Determining the momentum, energy, and PID associated with the dedicated sub-detectors from the raw data during the physics analysis would add extra load to the computational resources. Therefore, raw data is further processed to store in a suitable format. For that, tracks of the charged particles are reconstructed from the hits measured by the CDC, and associated hits to each track are sought in the SVD, ACC, TOF, ECL, and KLM to estimate the corresponding energy deposition and extrapolate the trajectory. Further, a helix is fitted to the charged track to determine the momentum and vertices, and the track is extrapolated to the PID systems to search for the associated information. ECL and KLM hits having no association with the charged tracks are considered neutral particle signatures, e.g., photons and K_L mesons. Energy information and/or flight direction are determined from these hits of the neutral particles. Finally, every relevant information for the neutral and charged particles, including the momenta, energy, PID likelihoods, and other information pertinent to the event, for example, the beam and experiment-related data, is stored in data summary tapes (DSTs) in the PANTHER file format

suitable for the data analysis [49, 50]. Data is further categorized according to the physics-specific processes, e.g., hadronic, Bhabhas, $\gamma\gamma$, $\mu^+\mu^-$, etc., and stored in mini-data storage tapes (MDSTs). This categorization is called skimming. The next chapter will discuss the Hadron-$B(J/\psi)$ skimming, which selects the hadronic B events decaying into J/ψ mode. The typical size of a hadronic event saved in MDST is 30 kB which includes only the information needed for physics analysis. The analyses are performed in a C++ framework called the Belle Analysis Software Framework (BASF). The BASF is also used in data processing by DAQ, Monte Carlo (MC) data generation, and event reconstruction for individual physics analysts. A detailed description of BASF can be found somewhere else in [51]. The MC data generation, its importance, and event reconstruction are discussed in detail in the next chapter.

2.5 Summary

This chapter briefly discussed the KEKB accelerator, physics events in e^+e^- collision at $\Upsilon(5S)$ resonance, the Belle detector, and the trigger systems and DAQ for the data collection. The next chapter will discuss the analysis strategy and event reconstruction specific to $B_s^0 \to J/\psi\pi^0$ decay.

Chapter 3

Signal Reconstruction and Event Selection

3.1 Introduction

We adopt a "blind" analysis procedure in which selection criteria and observable parameterization for the $B_s^0 \to J/\psi\pi^0$ signals are determined using the simulated data. $B_s^0 \to J/\psi\pi^0$ is a rare decay with an expectation of few events in the Belle dataset. Determining the event selection cuts or the parameters defining the signal box based on the actual data could bias the measurement toward the experimenter's preconception value. Further, such biases could not be quantified to estimate a systematic uncertainty in the measurement, and the high-energy experiments are costlier to reproduce the results. Therefore, in this method, optimized selection criteria for the signal events and probability distributions function (PDF) parameterization for the signal extraction are decided based on the Monte Carlo (MC) data. An experimenter can look at the actual data after the analysis completion. The salient points of the analysis strategy are as follows:

- We identify the electron and muon tracks and evaluate the four-momenta with the corresponding hypothesis. Four momenta of oppositely charged lepton candidates are added to reconstruct the J/ψ candidates in the electron and muon sectors, where J/ψ decays with a partial width of 11.93% [1]. Similarly, ECL clusters with no associated CDC tracks are identified as photons to reconstruct the $\pi^0 \to \gamma\gamma$ candidates, where the branching fraction for π^0 decaying in two photons is 98.83% [1]. Selected J/ψ and π^0 candidates are combined kinematically to reconstruct the $B_s^0 \to J/\psi\pi^0$ events. Finally, we compute the PDF for the observable distributions to extract the signals.

- A random combination of final state particles from the backgrounds can reconstruct the B_s^0 candidate. The selection criteria are determined to suppress the backgrounds maximally while retaining the optimum signal selection efficiency. The distribution shapes from various sources and the corresponding

expected contributions are computed using large background MC samples before unblinding data.

- We estimate the bias in signal extraction using MC toys. The estimated bias will be assigned as the systematic uncertainty in the signal extraction.
- We study the $B_d^0 \to J/\psi\pi^0$ at $\Upsilon(4S)$ resonance to check the discrepancy in simulated and recorded data and the correctness of the event selection algorithm.
- After the completion of the analysis using the MC data, the actual data is unboxed, and systematics from the various known sources are computed. Finally, we report a branching fraction measurement or the upper limit based on the significance of the observed signals.

The following sections discuss the MC data generation, the Belle dataset and skimming, $B_s^0 \to J/\psi\pi^0$ event reconstruction, and the background pre-identification. The following chapters will discuss the signal and background PDF parameterization procedure, bias estimation in signal extraction based on the MC samples, simulated and actual data difference estimation using the control sample, and extraction of signals from the actual data.

3.2 MC Generation

This section discusses the MC generation of signal events in detail. We further describe the MC backgrounds and categorize them according to their origin.

3.2.1 Signal MC

Within the Belle framework, the generator 'EvtGen' [52] generates MC events according to the provided decay file, which instructs the particular decay to happen. We include the three $\Upsilon(5S) \to B_s^{0(*)}\bar{B}_s^{0(*)}$ decay modes for generating the B_s^0-meson pairs with production fractions measured most precisely in [37]; $f_{B_s^{0*}\bar{B}_s^{0*}} = (87.0\pm1.7)\%$, $f_{B_s^0\bar{B}_s^{0*}} = (7.3\pm1.4)\%$, and remaining for the $\Upsilon(5S) \to B_s^{0*}\bar{B}_s^{0*}$, $B_s^0\bar{B}_s^{0*}$ or the charge conjugated pair, and $B_s^0\bar{B}_s^0$ respectively. The decay models used for different decay modes listed in Table 3.1 are as follows:

- **PHSP:** Generates events according to the available generic phase space to n-bodies (n = 2 for the two body decay). All spins of the initial and final state particles are averaged.
- **VSS:** Decays the Vector into a pair of scalar mesons.
- **VSP_PWAVE:** Decays the vector to a scalar meson and a photon.
- **SVS:** Decays the scalar into a vector and scalar mesons.

- **VLL:** Decays a vector meson into a pair of charged leptons.
- **PHOTOS:** Incorporates the radiative effects of the final state charged particles.

The decay file is given in Appendix A.

Next, 'Geant3' [53] simulates the generated events over the detector configuration. The experimental-dependent beam background is overlayed to the generated events, and the IP profile near the interaction region is smeared during the simulation to mimic the actual data. Simulated events are stored in a format (MDST files) similar to the actual data. A sequential workflow of the event generation procedure is given in Figure 3.1. We have generated the separate signal samples of e and μ sectors, each having 100,000 experimental-dependent MC events. Either B_s^0 or its charge-conjugate decays to the mode of interest in an event with equal chances, allowing another strange-B meson to decay generically.

Decay Table	
Decay mode	Decay Model
$\Upsilon(5S) \to B_s^{0*}\bar{B}_s^{0*}$	PHSP
$\Upsilon(5S) \to B_s^0\bar{B}_s^{0*}$ + cc	PHSP
$\Upsilon(5S) \to B_s^0\bar{B}_s^0$	VSS
$B_s^{0*} \to B_s^0\gamma$	VSP_PWAVE
$B_s^0 \to J/\psi\ \pi^0$	SVS
$J/\psi \to \mu^+\mu^-$	VLL + PHOTOS
$J/\psi \to e^+e^-$	VLL + PHOTOS
$\pi^0 \to \gamma\gamma$	PHSP

Table 3.1: Decay model used for MC signal event generation.

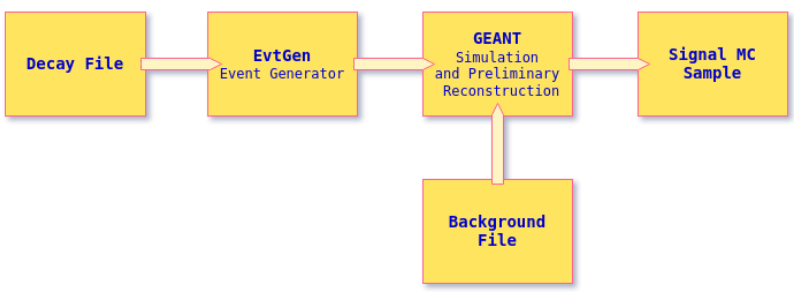

Figure 3.1: Sequentially steps followed in generating the MC samples.

3.2.2 Background MC

As discussed in the classification of hadronic event production at $\Upsilon(5S)$ resonance, in Figure 2.3, the contribution from the following backgrounds are categorized as:

- **Continuum**
  $e^+e^- \to q\bar{q}$, where $q = u,\ d,\ s,$ and c quarks.

- **bsbs**
  $e^+e^- \to \Upsilon(5S) \to B_s^{0(*)}\bar{B}_s^{0(*)}$ generic decay.

- **non-bsbs**
  $e^+e^- \to \Upsilon(5S) \to B^{(*)}\bar{B}^{(*)}$, $B^{(*)}\bar{B}^{(*)}\pi$, and $B\bar{B}\pi\pi$ generic decay; where B represents the B_d^0 and its charged-conjugate and $B^{\pm}$ mesons.

We have analyzed the six streams of dedicated MC data generated by the production team in Belle to study these backgrounds. Each stream has the number of events equivalent to the actual recorded, having a total luminosity of 121.4 fb^{-1}.

3.3 Event Selection and Reconstruction

We select the events passing the L4 trigger to reject the beam-related background, as mentioned in section 2.4.3. We filter the B meson events using the Hadron-$B(J/\psi)$ skimming; a detailed description is given in the following subsection.

3.3.1 Hadron-$B(J/\psi)$ Skimming

e^+e^- collisions at $\Upsilon(5S)$ result in the Bhabha scattering, two-photon, lepton-pair ($\mu^+\mu^-$ and $\tau^+\tau^-$), and $q\bar{q}$ other than the $b\bar{b}$ production. The Hadron-B criteria select the B-meson and continuum events with an efficiency of 99% and 84% while rejecting the non-hadronic components by more than 95%. Hadron-B skimming consists of the following loose requirements:

- **Track multiplicity**
  A B meson event must have at least three good tracks having transverse momentum P_t >100 MeV/c and satisfying the closest point of approach to the IP of $|dr| < 2.0$ cm $|dz| < 4.0$ cm in the plane perpendicular to the beam axis and along the z-axis, respectively. The track multiplicity requirement suppresses the retaining of fake events from the beam-induced background.

- **Event Primary Vertex**
  The best primary vertex for an event is constructed by feeding the good tracks into the track-fitter, 'kFitter'. The radial and longitudinal spread of the vertex around the IP is required to be within PrimeR< 1.5 cm and |PrimeZ| < 3.5 cm, further reducing the beam background.

- **Calorimeter Energy Sum ($E_{\mathbf{sum}}$)**
  ECL clusters with no track matching in CDC and having a threshold energy of 100 MeV are identified as good photons. The energy sum of the good clusters, $E_{\rm sum}$, is required to satisfy $0.18 < E_{\rm sum}/\sqrt{s} < 0.8$.

- **Visible Energy of the Tracks and Photons ($E_{\rm vis}$)**
  The energy sum of good clusters and good tracks momenta with a π-mass hypothesis, $E_{\rm vis}$, is required to be $> 0.2\sqrt{s}$. Conditions of $E_{\rm sum}$ and $E_{\rm vis}$ suppress the two photons and Bhabha events.

- **Momentum Balance**
  The total sum of longitudinal momentum of the good tracks and photons is balanced around zero by requiring the $|\sum p_z| < 0.5\sqrt{s}$.

- **Calorimeter Cluster Multiplicity (nECL)**
  ECL clusters produced in the QED events have shallow angles. For that, the number of ECL clusters is required to be > 1 within the fiducial volume of $-0.7 < \cos\theta < 0.9$.

- **Conditional Calorimeter Energy sum**
  A conditional cut on the heavy jet mass (HJM) is applied to regain the efficiency loss for the continuum events that fail to meet the $E_{\rm sum}$ criteria. Jets from the τ-pairs are relatively collimated than the $q\bar{q}$ because of the color charge for the latter. Therefore, the event is split into two hemispheres by a plane perpendicular to the thrust axis. The thrust axis is the unit vector along which the total projection of tracks momenta is maximum. The invariant mass of each hemisphere is calculated assuming the π tracks, and the heavier is selected as the HJM. We apply a conditional cut of $E_{\rm sum} > 0.18\sqrt{s}$ or HJM> 1.8 GeV/c^2.

- **Conditional Normalized Heavy Jet Mass**
  The HJM requirement suppresses the τ-pair events significantly but has a shift in the MC and data distributions, causing an unpredictable efficiency loss in the B meson events. In contrast, due to the strong correlation and the similar shift for the $E_{\rm vis}$, the difference cancels for the ratio HJM/$E_{\rm vis}$. Therefore, a conditional cut on the HJM/$E_{\rm vis}$ ratio is employed to regain the continuum events inconsistent with the τ-pair events, as HJM/$E_{\rm vis} > 0.25$ or HJM> 1.8 GeV/c^2.

- **Average Cluster Energy**
  The QED events with one of the electrons in the ECL gap will fulfill the nECL condition. However, the depositing cluster has the energy of at least a few GeV. Therefore, we remove such events by cutting the average cluster energy, $E_{\rm sum}$/nECL < 1.0 GeV.

Since the signal mode involves the J/ψ meson as one of the daughters, we employ loose selection criteria for the charmonium state. We consider an event with at least one combination of oppositely charged tracks with momentum $p > 0.8$ GeV/c and invariant mass between $2.4 - 4.0$ GeV/c^2. The charged tracks are reconstructed assuming the $\pi^{\pm}$ hypothesis. We employ hadron-$B(J/\psi)$ skimming before the $B^0_s \to J/\psi\pi^0$ event reconstruction, which is thoroughly discussed in the following subsections.

3.3.2 Charged Track Selection and Lepton Identification

We select the charged particles through the track information in the SVD and CDC detectors. A helix is fitted to the induced signals in detectors, and the distance of the closest approach to the IP on the transverse plane and along the longitudinal axis, i.e., dr and dz, are calculated. We expect the charged tracks from signal events to emerge from the IP as the mean lifetimes of B_s^0 and J/ψ mesons are very short. We employ a loose cut on the impact parameters of $|dr| < 0.5$ cm and $|dz| < 3.0$ cm to select the good charged tracks. The electron and muon tracks are identified as:

e-Identification

Electrons are distinguished [54] from the other charged particles, e.g., muons and charged hadrons, through their interactions in the CDC, ECL, and ACC sub-detectors. The differences in the energy deposition and evolution of electromagnetic and hadronic showers induced by electrons and charged hadrons are exploited to distinguish them. Also, the difference in velocities of electrons and hadrons of the same momenta discriminates them in the low-momentum range. Electron (L_e) and non-electron ($L_{\bar{e}}$) likelihoods for each of the following discriminants are calculated based on the PDFs constructed using the real and MC data:

- The position of a charged track extrapolated to the ECL and energy cluster position measured by the ECL are matched as the position resolution for the electron shower is considerably smaller than for the hadrons. Further, the matching is required to accurately calculate the ratio E/p of energy deposition in the ECL and the track's momentum measured by the CDC of a charged particle, which has substantial discriminating power. Quantitatively, it is estimated by the quality of fit, defined as $\chi^2 \equiv \left(\frac{\Delta\theta}{\sigma_{\Delta\theta}}\right)^2 + \left(\frac{\Delta\phi}{\sigma_{\Delta\phi}}\right)^2$, where the differences $\Delta\theta$ and $\Delta\phi$ are the miss-match in the θ and ϕ directions. The resolutions $\sigma_{\Delta(\theta,\phi)}$ are the widths obtained by fitting the $\Delta\theta$ and $\Delta\phi$ distributions with the Gaussian distribution.

- The expected E/p ratio for electrons is typically higher than the charged hadrons in the $E > 0.5$ GeV energy region.

- Transverse evolution is quantitatively calculated by the ratio of energy deposition in 3×3 and 5×5 arrays of crystals surrounding the crystal at the center of the shower, E_9/E_{25}. Since the electromagnetic cluster evolves faster than the hadronic, measured in material depth, hadrons will have a widespread E_9/E_{25} distribution.

- The charged particle's energy loss dE/dx through the ionization of CDC gas is proportional to the β^{-2}. Therefore, electrons will lose more energy than the other charged particles of the given momentum.

- The threshold for electrons to produce Cherenkov radiations in the ACC is just a few MeV, whereas, for pions, it varies from 0.5 - 1.0 GeV/c depending

upon the refractive index. The light yield of the aerogel radiator is used as the discriminant to calculate the likelihood using PDFs calculated from the MC distributions.

Likelihoods from each discriminant are combined to get the electron ID ($e_{\rm ID}$), as:

$$e_{\rm ID} = \frac{\prod_i L_e^i}{\prod_i L_e^i + \prod_i L_{\bar{e}}^i} \tag{3.1}$$

where i runs over each discriminant. $e_{\rm ID}$ does not give the probability but is essential for discriminating the electrons and other charged particles.

μ-Identification

Muons are identified [55] from the information in KLM and tracking detectors. The tracks of charged particles are extrapolated to the KLM detector assuming the charged π hypothesis and matched to hits in the glass-electrode RPCs, where the hits are signal induced on the orthogonal readout strips by the streamer that forms in the RPC gas gap along the passing charged particle's trajectory. Tracks with no nearby associated hits are exempted from the μ-candidature. While remaining tracks are extrapolated with the pion hypothesis, assuming no hadronic interaction with the material. In contrast to pions, muons will penetrate deeper or escape the detector as they do not interact hadronically with the iron sheets. So, the difference between the outermost RPC layer number crossed by the extrapolated track and the layer with the associated hits must be no more than five. The remaining tracks are re-extrapolated using the Kalman filtering technique with a muon track assumption. This technique steers the track to the next layer based on the feedback from associated hits in the preceding KLM layers accounting for the growth in transverse deviation due to multiple scattering, energy loss in ionization, and this steering of the re-extrapolated tracks. The muon-likelihood ratio is calculated using PDFs for the expected and measured range difference and the quality fit (χ^2) of the transverse deviations of all hits associated with the re-extrapolated track.

Lepton ID Requirements

Figure 3.2 shows the area-normalized distributions of electron and muon-likelihood ratios in signal and background MC samples. Note that the background sample consists of one data stream of the continuum, bsbs, and non-bsbs events. A primary peak near unity for both distributions indicates the particles of interest agreeing with the generated MC signal events, as shown with a black-colored line. The secondary peak near 0 is attributed to fake or poorly reconstructed IDs. We employ loose selection criteria of $e_{ID} > 0.01$ and $\mu_{ID} > 0.4$ to reject the contribution from the secondary peak in the background MC events. The required conditions select the correct leptons based on the MC truth information with an efficiency of 96.40% and 89.64% in the electron and muon sectors, respectively, where the efficiency is

the ratio of the number of correctly identified tracks to the actual tracks before the requirement.

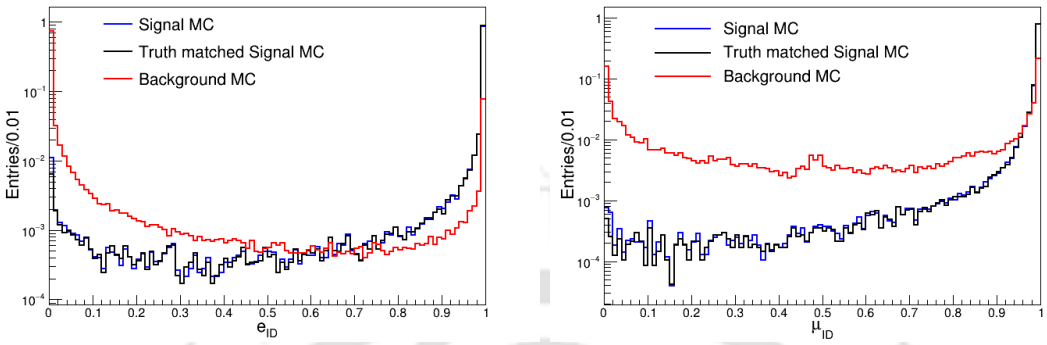

(a) (b)

Figure 3.2: The area-normalized distributions of the (a) electron and (b) muon likelihood ratio. Blue and red lines represent the MC distributions of signal and background samples, whereas the black line indicates the likelihood ratio for MC truth-matched signal tracks.

3.3.3 J/ψ Reconstruction

The four-momenta of oppositely charged lepton pairs of the same kind are added together to reconstruct the kinematics for the J/ψ candidates, e.g., the four-momenta and invariant masses. However, the electron channel loses radiative energy due to bremsstrahlung radiations of the final state particles. Therefore, we account for the photons in a conical region with an opening angle of 50 mrad along either charged particle's track. The angular requirement is justifiable from the distributions in Figure 3.3 for the signal MC, where the emerging angle between the charged track and

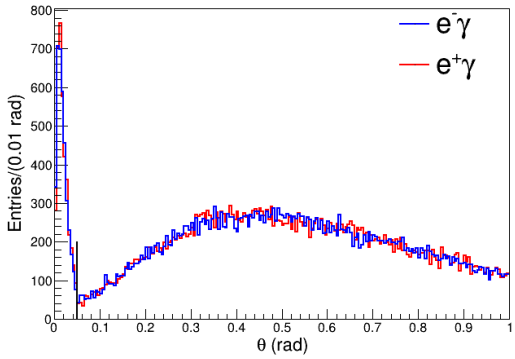

Figure 3.3: The angle distribution between an electron (positron) track and photon momenta for the signal MC, as shown in blue (red) color. Black-colored verticle line infers the requirement on an angle for the bremsstrahlung correction.

photons propagation directions are distributed. The E_9/E_{25} ratio is required to be greater than 0.75 to suppress the miss-identification of neutral hadrons as photons.

The four-momentum for the two systems in μ and e sectors are computed as follows:

$$P^{\nu}_{\mu^+\mu^-} = P^{\nu}_{\mu^+} + P^{\nu}_{\mu^-}, \tag{3.2}$$

$$P^{\nu}_{e^+e^-(\gamma)} = P^{\nu}_{e^+} + P^{\nu}_{e^-} + (P^{\nu}_{\gamma}), \tag{3.3}$$

where $P^{\nu}_{\mu,e}$ are the four-momentum of electron and muon, and P^{ν}_{γ} is the four-momentum of bremsstrahlung correction if it matches the condition. Figure 3.4 shows the invariant mass distributions of the reconstructed J/ψ candidates in the electron and muon sectors. A comparatively long tail in the electron channel attributes to the radiative effects and poor reconstruction of the cluster energy because of the QED background in the ECL. The reconstructed J/ψ invariant masses $M_{\mu^+\mu^-}$ and $M_{e^+e^-(\gamma)}$ are required to satisfy -71 MeV/c^2 $< M_{\mu^+\mu^-} - m_{J/\psi} <$ $+42$ MeV/c^2 and -93 MeV/c^2 $< M_{e^+e^-(\gamma)} - m_{J/\psi} <$ $+56$ MeV/c^2, respectively, where the intervals correspond to $[-5\sigma, 3\sigma]$ region around the nominal J/ψ mass, $m_{J/\psi}$ [1]. The widths are determined by fitting the distributions using the Gaussian function with a long tail. Asymmetric mass-window cuts account for the radiative effects resulting in a tail toward the lower values of invariant masses.

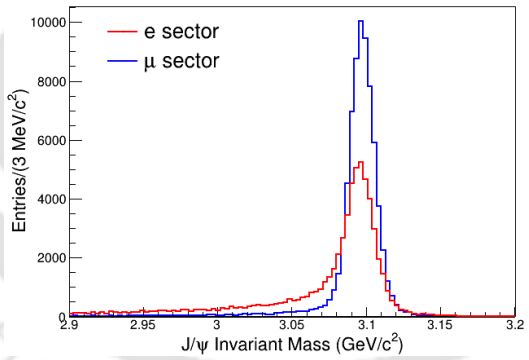

Figure 3.4: Invariant mass distributions of the signal MC J/ψ candidates. The red and blue histograms represent the invariant mass in the electron and muon sectors.

Further, we perform the mass and vertex constraint fits using 'kMassVertexFitter' to improve the momentum resolution. Since the mean lifetime of J/ψ is very short of order $\mathcal{O}(10^{-21})$, the vertex of two charged tracks is required at IP, whereas the mass is constrained to the nominal $m_{J/\psi}$ [1]. Figure 3.5 shows the fit quality (χ^2) distributions of mass-vertex constraint for the electron and muon sectors of the signal MC. As expected, the muon sector has comparatively better-fit quality because of the clean track reconstruction. We consider the reconstructed J/ψ satisfying the requirement of $\chi^2 < 60$ as good candidates. The mass window and constraint fit significantly suppress the continuum background due to its light-quark mesons composition.

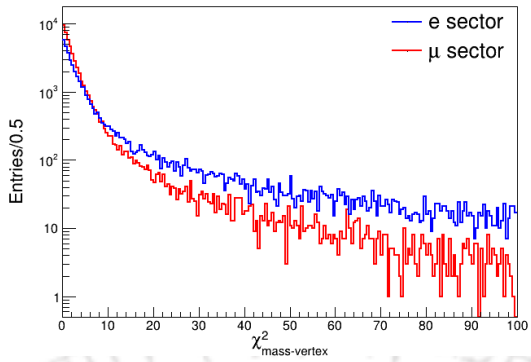

Figure 3.5: Fit quality (χ^2) distributions of the mass-vertex constraint for the J/ψ candidates in signal MC. The red and blue histograms represent the candidates in the electron and muon sectors.

3.3.4 π^0 Reconstruction

We use MDST_π^0 bank to select the π^0 candidates. ECL clusters not matched to any charged track are identified as photons candidates for the $\pi^0 \to \gamma\gamma$ reconstruction. The energy spectrum of the photon candidates in the lab frame varies with the polar angle due to the CM boost in the forward direction. Figure 3.6 shows the energy distribution of the first π^0 daughter (photon) in three parts of ECL: forward endcap (FE), barrel region (BR), and backward endcap (BE) covering the polar angle $12^\circ < \theta < 32^\circ$, $32^\circ < \theta < 130^\circ$, and $130^\circ < \theta < 154^\circ$, respectively. However, the QED background affects the reconstruction of the low-energy photons. Therefore, as the beam energy is boosted forward and π^0 carries most of the kinematic energy due to its lighter mass than the J/ψ, we require the photon candidates to have a minimum threshold energy of 50 and 100 MeV in the barrel and both end-cap regions. The $\gamma\gamma$ invariant mass, $M_{\gamma\gamma}$ is required to be within a loose window of 80 MeV/c^2 $< M_{\gamma\gamma} <$ 180 MeV/c^2. Further, the mass of the selected π^0 candidates is constrained to the nominal value, m_π^0 [1], to improve the momentum resolution.

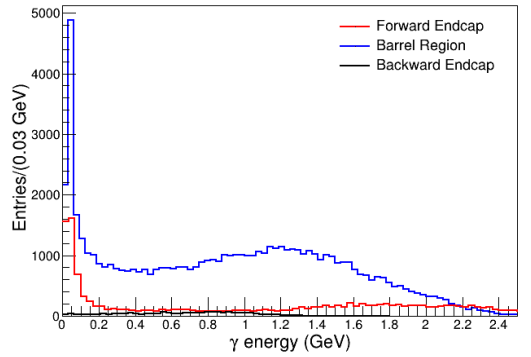

Figure 3.6: Photon energy distribution sampled from the signal MC. The red, blue, and black lines represent the photons in the FE, BR, and BE.

We select the π^0 candidates satisfying the requirement of $\chi^2 < 30$ on the fit quality to avoid the random combination of photons.

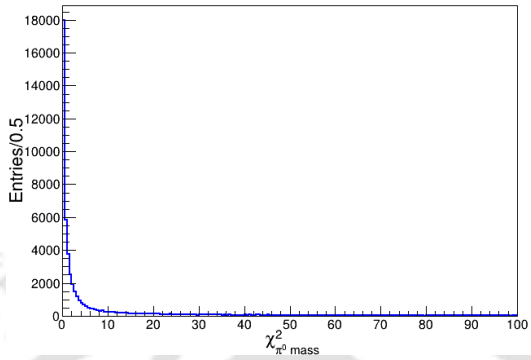

Figure 3.7: χ^2 distribution of the mass-constraint fit for the signal MC π^0 candidates.

3.3.5 B_s^0 Reconstruction

Four momenta of the selected J/ψ and π^0 candidates in an event are added to reconstruct the B_s^0 candidates. We compute the kinematical observables for the $B_s^0 \to J/\psi\pi^0$ event, the beam-constraint mass (M_{bc}) and energy difference (ΔE) as follows:

$$M_{\mathrm{bc}} = \left(\sqrt{{E_{\mathrm{beam}}}^2 - |\vec{p}_{B_s^0}|^2 c^2}\right)/c^2, \tag{3.4}$$

$$\Delta E = E_{B_s^0} - E_{\mathrm{beam}}, \tag{3.5}$$

where E_{beam} is the beam energy, $\vec{p}_{B_s^0}$ and $E_{B_s^0}$ are the momentum and energy of the B_s^0 candidates, all calculated in the CM frame.

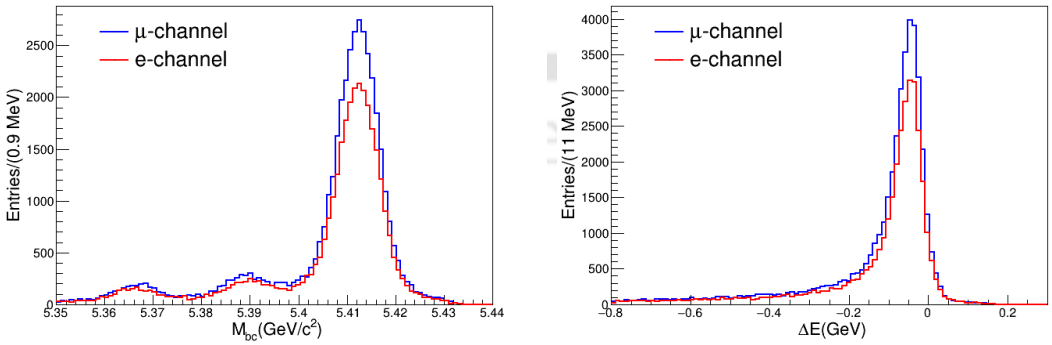

Figure 3.8: M_{bc} and ΔE distributions for the MC $B_s^0 \to J/\psi\pi^0$ signals.

Figure 3.8 shows the M_{bc} and ΔE distributions for the MC signal events. M_{bc} distribution has a primary peak around the nominal B_s^{0*} mass (≈ 5.41 GeV/c^2) attributing to the $\Upsilon(5S) \to B_s^{0*}\bar{B}_s^{0*}$ production. Middle and leftmost peaks attribute

to the $\Upsilon(5S) \to B_s^{0*}\bar{B}_s^0$ or its charge-conjugated (CC) pair and $B_s^0\bar{B}_s^0$ events, respectively. The relative height of the peaks are in accordance with their relative abundance, as given in equations 2.4 and 2.5. The distributions follow a Gaussian shape with a broader width and a long tail because of the leakage in energy reconstruction.

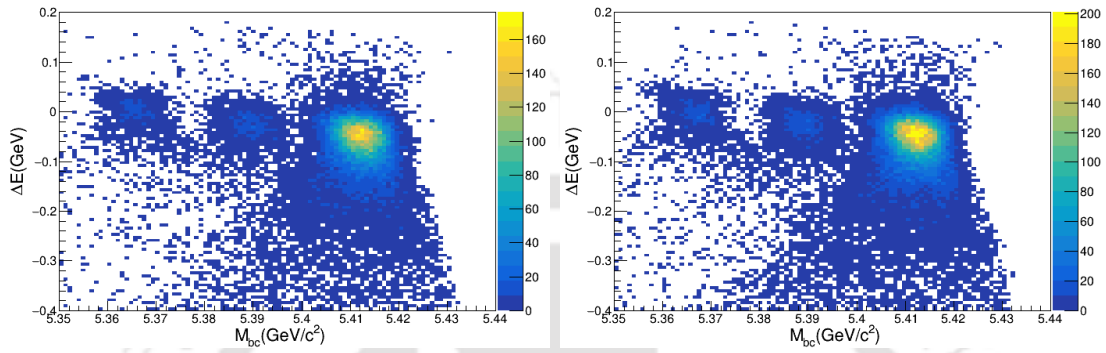

Figure 3.9: ΔE vs $M_{\rm bc}$ distributions for the signal MC data in (a) electron and (b) muon channels. An apparent negative slope for the central positions of the clusters is due to the energy loss in radiated photons.

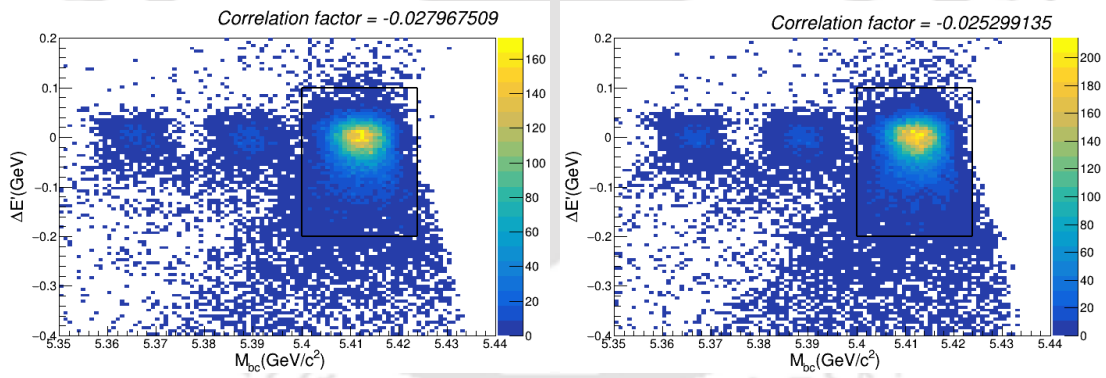

Figure 3.10: $\Delta E'$ vs $M_{\rm bc}$ distributions for the signal MC data in (a) electron and (b) muon channels. The box of dimensions $5.400 < M_{\rm bc} < 5.424$ GeV/c^2 and $-0.2 < \Delta E' < 0.1$ GeV represents the region around the prominent peak where the probability of finding the signal is enhanced.

Three $B_s^{0(*)}\bar{B}_s^{0(*)}$ production pairs have a slight difference in the ΔE means as the photon energy has not been accounted in $B_s^{0*} \to B_s^0\gamma$ decay. This results in a wide spread of the ΔE distribution. The shift in the ΔE means is evident from the scattered plots in Figure 3.9, which are of order -25 MeV and -50 MeV with respect to the position for $B_s^0\bar{B}_s^0$ decay mode. For the energy correction, we redefine ΔE as:

$$\Delta E' = \Delta E + (M_{\rm bc} - m_{B_s^0})c^2 \tag{3.6}$$

where, $m_{B_s^0} = 5366.7\ \mathrm{MeV}/c^2$ is the nominal B_s^0 mass [1]. The corrected distributions are given in figure 3.10. We further compute the linear correlation coefficient between the variables in a region $5.400 < M_{\mathrm{bc}} < 5.424\ \mathrm{GeV}/c^2$ and $-0.2 < \Delta E' < 0.1$ GeV. The correlation coefficient around the prominent peak is less than 3.0%.

A random combination of the final state particles in the continuum background can satisfy the selection criteria and construct a fake $B_s^0 \to J/\psi\pi^0$ event. However, the event topology of the hadron production in the CM frame, i.e., the momentum and directional distribution of the final state particles in a continuum event, differs from the hadronic $B\bar{B}$ event. As discussed in the following subsection, we utilize this difference in reducing such background.

3.3.6 Continuum Suppression

The absence of J/ψ in continuum events imposed with the narrow mass window and quality on the fit requirements have significantly suppressed the background. The electron-positron collisions in $\Upsilon(5S)$ rest frame have different phase spaces for $B_s^0\bar{B}_s^0$ and continuum events. The cascades of hadrons produced in $e^+e^- \to q\bar{q}$ form jets aligned back to back. In contrast, the propagation direction of the final state particles coming from strange B-meson is almost spherically symmetric in the CM frame, as the rest mass energy of $\Upsilon(5S)$ is a few 100 MeV above the $B_s^0\bar{B}_s^0$ production threshold. We utilize this difference to suppress the continuum background further.

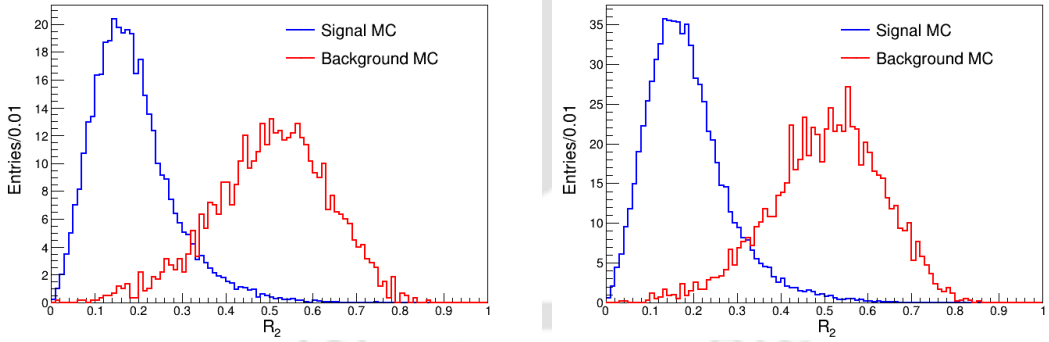

(a) (b)

Figure 3.11: R_2 distributions for the MC data in (a) electron and (b) muon sectors. The blue and red histograms represent the signal and continuum background data events.

We calculate the ratio of second to zeroth order Fox-Wolfram moments [56], known as the reduced Fox-Wolfram variable given by

$$R_2 = \frac{H_2}{H_0}. \tag{3.7}$$

The H_l is the l^{th} Fox-Wolfram moment defined as:

$$H_l = \sum_{i \neq j} |p_i||p_j| P_l(\cos(\theta_{ij})), \tag{3.8}$$

where p_i and p_j are the momentum of i^{th} and j^{th} final state charged particles with θ_{ij} angle in between; and $P_l(\cos\theta)$ is the l^{th} order Legendre polynomial. Figure 3.11 shows the R_2 distributions for the MC data in electron and muon sectors. The signal distributions are normalized to the selected continuum events in the equivalent MC data of luminosity 121.4 fb^{-1}. The difference in event topology is evident from the distributions.

Cut	Muon Sector		Electron Sector	
	Signal	Continuum	Signal	Continuum
$R_2 < 0.3$	11.0%	93.3%	10.9%	91.5%
$R_2 < 0.4$	3.1%	80.4%	3.1%	76.0%

Table 3.2: The percentage loss in the signal and background events for various conditions on R_2.

Table 3.2 lists the percentage loss of the signal and background events due to the various R_2 conditions. We have required a loose requirement of $R_2 < 0.4$ as it suppresses more than 75% of the continuum events with a signal loss of around 3%.

3.3.7 Best Candidate Selection

For further analysis, we consider the candidates having a reasonable $-0.2 < \Delta E' < 0.1$ GeV range. As mentioned before, we have allowed only strange-B meson or its conjugate to decay in the mode of interest while generating an event. Therefore, the number of reconstructed candidates per event, called multiplicity, should equal one for an ideal reconstruction.

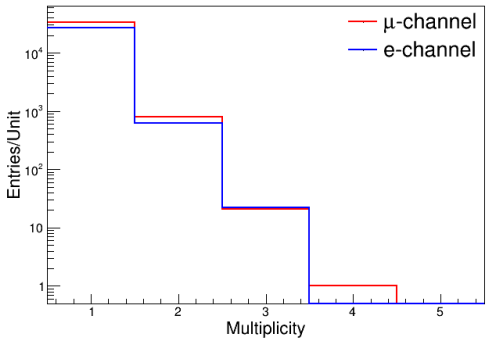

Figure 3.12: The number of selected $B_s^0 \to J/\psi\pi^0$ candidates per event. The blue and red histograms represent the electron and muon sectors.

Figure 3.12 shows the number of reconstructed candidates in an event after implying all the requirements. Approximately 2.3% of the events have higher multiplicity in electron and muon sectors, mainly because of multiple π^0 candidates. Therefore, we select the best candidates (BCS) based on the least χ^2 sum of the J/ψ and π^0 constraint fits. The χ^2 sum is defined as:

$$\sum \chi^2 = \chi^2_{J/\psi} + \chi^2_{\pi^0}, \tag{3.9}$$

where $\chi^2_{J/\psi}$ is the quality of mass-vertex constraint fit for the reconstructed J/ψ candidate and $\chi^2_{\pi^0}$ is the quality of constraint fit on the π^0 mass. The BCS efficiency in selecting a correct signal candidate is defined as:

$$\epsilon_{\text{BCS}} = \frac{\text{Number of truth-matched best selected candidates}}{\text{Number of events with multiple candidates}}, \tag{3.10}$$

which, based on the MC truth information, is estimated at 79.4% and 77.4% in electron and muon channels, respectively. Thus, BCS selects correctly reconstructed signals in more than 77% of the multiple-candidate events. The criteria used for the $B^0_s \to J/\psi\pi^0$ selection is briefly summarized in table 3.3, whereas figure 3.13 shows the signal MC distributions for M_{bc} and $\Delta E'$.

Variable	Requirement
Pre-selection criteria	
M_{bc}	> 5.35 GeV/c^2
$\Delta E'$	[-0.2, 0.1] GeV
Track selection and J/ψ reconstruction	
$\lvert dr\rvert$	< 0.5 cm
$\lvert dz\rvert$	< 3.0 cm
e_{ID}	> 0.01
μ_{ID}	> 0.4
$M_{e^+e^-(\gamma)} - m_{J/\psi}$	(-71, 42) MeV/c^2
$M_{\mu^+\mu^-} - m_{J/\psi}$	(-93, 56) MeV/c^2
$\chi^2_{J/\psi_{Mass-Vertex}}$	< 60
γ selection and π^0 reconstruction	
γ_{energy} in FE, BR, BE	$> 100, 50, 100$ MeV
$\chi^2_{M^0_\pi}$	< 30
Continuum suppression	
R_2	< 0.4
Events with multiple candidates	
BCS	Least $\sum_i^2 \chi^2_i$

Table 3.3: Requirements for the $B^0_s \to J/\psi\pi^0$ event selection.

We define the signal-enhanced region where the probability of a selected event as the signal is maximum, referred to as signal region (SR). We choose the SR around

the prominent peak of the $M_{\rm bc}$ distribution since it contributes to about 87% of the total signals and an asymmetric region for the $\Delta E'$ because of the long tail. The SR is defined as:

$$5.400 < M_{\rm bc}\ ({\rm GeV}/c^2)\ < 5.425 \quad \text{and} \quad -0.10 < \Delta E'\ ({\rm GeV})\ < 0.05. \tag{3.11}$$

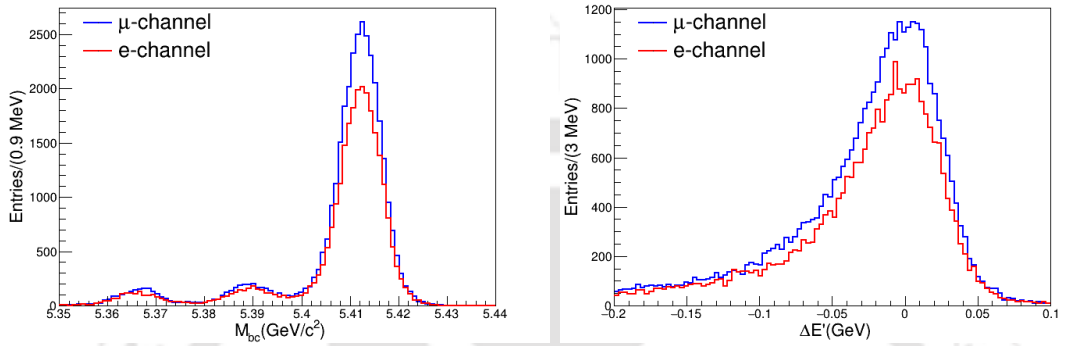

Figure 3.13: $M_{\rm bc}$ and $\Delta E'$ distributions for the MC $B_s^0 \to J/\psi\pi^0$ signals.

3.4 Signal Selection Efficiency

We compute the signal selection efficiency (ϵ) and the associated uncertainty as:

$$\epsilon = \frac{N_{\rm R}}{N} \tag{3.12}$$

$$\Delta\epsilon = \sqrt{\frac{\epsilon \times (1-\epsilon)}{N}} \tag{3.13}$$

where N and $N_{\rm R}$ are the number of generated and reconstructed $B_s^0 \to J/\psi\pi^0$ events. As mentioned, we have generated a signal sample of 100,000 MC events for each electron and muon mode. The event selection cuts, as mentioned in Table 3.3, select 27,582 and 34,458 signals in the electron and muon sectors with a respective efficiency of (27.58±0.14)% and (34.46±0.15)%. The combined efficiency of selecting the $B_s^0 \to J/\psi\pi^0$ events is estimated to be $(31.02 \pm 0.10)\%$, which includes both leptonic modes. As determined from the MC truth information, about 1.8% of the selected events have incorrectly reconstructed $B_s^0 \to J/\psi\pi^0$ candidates. In contrast, SR has signal miss-reconstruction of less than 1%.

3.5 Background Study

We run the same algorithm in six streams of MC background data consisting of continuum, bsbs, and non-bsbs to estimate the background contributions in selecting a candidate event. Each stream corresponds to the total integrated luminosity

of 121.4 fb^{-1} of experimental data. The random combinations of final state particles can pass the selection criteria and mimic the signal candidates. It is worth emphasizing that the combinatorial background in continuum has been rejected to a large extent as it consists of light quark mesons. Further, the requirement on reduced Fox-Wolfram variable of $R_2 < 0.4$ suppresses continuum events by more than 75% in both channels. Figure 3.14 shows the $M_{\rm bc}$ and $\Delta E'$ distributions using six streams of background MC. The distributions include both leptonic modes. As can be seen, the expected background is low and is dominated by the bsbs and non-bsbs backgrounds. Most events in two backgrounds have correctly reconstructed J/ψ, whereas a random combination of photons constitutes the fake $B_s^0 \to J/\psi\pi^0$ event.

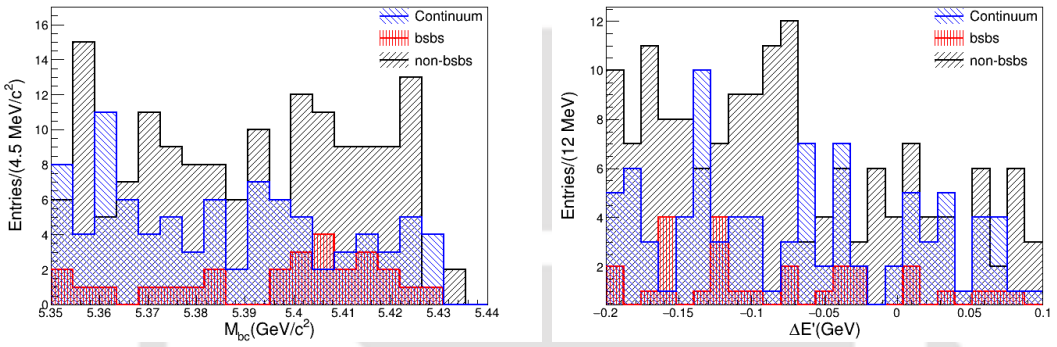

(a) (b)

Figure 3.14: Background distributions sampled from six streams of MC data: (a) $M_{\rm bc}$ and (b) $\Delta E'$. Blue, red, and black lines represent the continuum (left-slanting), bsbs (vertical), and non-bsbs (right-slanting) backgrounds.

	Continuum	$B_s^{0(*)}\bar{B}_s^{0(*)}$	non-$B_s^{0(*)}\bar{B}_s^{0(*)}$
μ-channel	6	5	15
e-channel	4	4	16

Table 3.4: Background contributions within the SR. Shown events are selected from six streams of MC data.

Table 3.4 shows the various background contributions in the SR using six streams of MC data. As can be seen, the non-bsbs dominate the background with a correctly reconstructed J/ψ. Therefore, a detailed study is required to understand these backgrounds with a larger sample. We have generated the dedicated MC samples to analyze further and parameterize the distribution shapes. For this, experimental dependent 20 and 10 million $b \to c\bar{c}q$ events are generated at $\Upsilon(5S)$ resonance involving the bsbs and non-bsbs backgrounds, respectively. Accordingly, both leptonic decays of J/ψ are considered [1]. The PDF parameterization of the background distributions is thoroughly discussed in the next chapter.

3.5.1 Charmonium decays of non-bsbs background

Firstly, we produce the following non-strange $B^{(*)}\bar{B}^{(*)}$ states at $\Upsilon(5S)$:

- $\Upsilon(5S) \to B^{+*}B^{-*}$, $B^{+*}B^{-}$, $B^{+}B^{-}$ (VSS), $B_d^{0*}\bar{B}_d^{0*}$, $B_d^{0*}\bar{B}_d^{0}$ and $B_d^{0}\bar{B}_d^{0}$ (VSS).
- $\Upsilon(5S) \to B^{+*}B^{-*}\pi^0$, $B^{*+}B^{-}\pi^0$, $B^{+}B^{-}\pi^0$, $B_d^{0*}\bar{B}_d^{0*}\pi^0$, $B_d^{0*}\bar{B}_d^{0}\pi^0$, and $B_d^{0}\bar{B}_d^{0}\pi^0$.
- $\Upsilon(5S) \to B_d^{0*}B^{-}\pi^{+}$, $B_d^{0}B^{*-}\pi^{+}$, $B_d^{0}B^{-}\pi^{+}$, and $B_d^{0*}B^{-*}\pi^{+}$.
- $\Upsilon(5S) \to (\Upsilon(4S) \to B^{+}\bar{B}^{-}$ (VSS), $B_d^{0}\bar{B}_d^{0}$ (VSS)$)\gamma$.

The charge conjugation is employed while generating the events. The $B\bar{B}$ pairs are produced using the model PHSP if not stated otherwise, as this analysis neither focuses on CP violation studies nor employs the tagging method for the other end. In contrast, as stated earlier, the VSS model generates decay for the vector to scalar-scalar mesons. An MC sample 100 times the actual $b \to c\bar{c}q$ decays of the charged and mixed B mesons at $\Upsilon(4S)$ resonance is officially available at Belle. We use these existing decay tables to generate the $B \to c\bar{c}X$ events, which contain all the known $b \to c\bar{c}q$ decays [1].

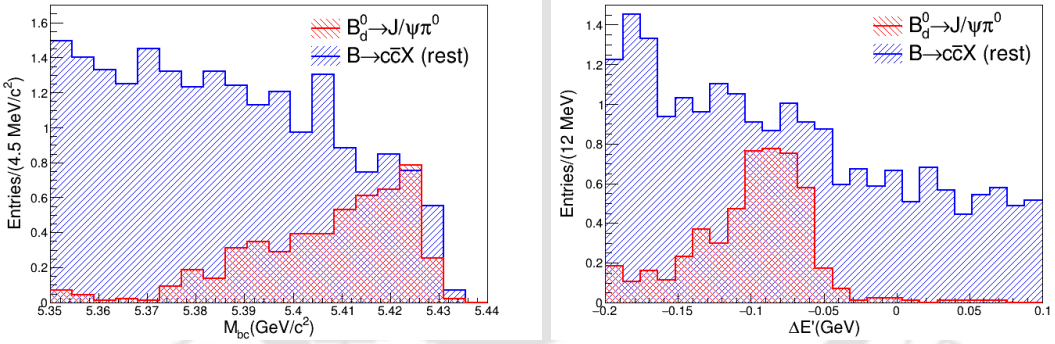

(a) (b)

Figure 3.15: (a) $M_{\rm bc}$ and (b) $\Delta E'$ distributions studied from an MC sample consisting of 10 million non-bsbs $b \to c\bar{c}q$ events. The distributions are scaled to the equivalent data luminosity. Red and blue histograms represent the selected candidates in $B_d^0 \to J/\psi\pi^0$ (right-slanting) and the other charmonium events (left-slanting).

Figure 3.15 shows the (a) $M_{\rm bc}$ and (b) $\Delta E'$ distributions of selected candidates in charmonium decays of B mesons studied from an MC sample of 10 million events. The distributions are normalized to the expected background events in the data luminosity. As can be seen, the background from $B_d^0 \to J/\psi\pi^0$ has a specific peaking structure in the candidate region of $M_{\rm bc}$ and $\Delta E'$. Therefore, we further generate 200,000 MC events to parameterize this background.

3.5.2 Charmonium decays of bsbs background

The $B_s^{0(*)}\bar{B}_s^{0(*)}$ pairs for the bsbs background at $\Upsilon(5S)$ resonance are generated similarly to the signal MC generation. We have generated 20 million events with the charmonium decay of B_s^0 mesons, following the measured branching fractions [1]. The decay modes and the corresponding models are listed in Table 3.5. An excited charmonium state from the B_s^0 meson decays to a J/ψ followed by the leptonic modes. The PHOTOS package incorporates the bremsstrahlung radiation effect associated with the final state charged particles.

Decay mode	Decay Model
$B_s^0 \to J/\psi\phi$	PHSP
$B_s^0 \to J/\psi\phi\phi$	PHSP
$B_s^0 \to J/\psi\eta$	SVS
$B_s^0 \to J/\psi\eta\prime$	SVS
$B_s^0 \to J/\psi K_s^0$	SVS
$B_s^0 \to J/\psi K^*(892)^0$	PHSP
$B_s^0 \to J/\psi\pi^+\pi^-$	PHOTOS + PHSP
$B_s^0 \to J/\psi f_0(1500)$	PHSP
$B_s^0 \to J/\psi K^+K^-$	PHOTOS + PHSP
$B_s^0 \to J/\psi K^0\pi^+\pi^- + cc$	PHOTOS + PHSP
$B_s^0 \to J/\psi\pi^+\pi^-\pi^+\pi^-$	PHOTOS + PHSP
$B_s^0 \to \psi(2S)\eta$	SVS
$B_s^0 \to \psi(2S)\eta\prime$	SVS
$B_s^0 \to \psi(2S)\pi^+\pi^-$	PHOTOS + PHSP
$B_s^0 \to \psi(2S)\phi$	PHSP
$B_s^0 \to \psi(2S)K^-\pi^+$	PHSP
$B_s^0 \to \psi(2S)K^*(892)^0$	PHSP
$B_s^0 \to \chi_{c1}\phi$	PHSP
$B_s^0 \to \chi_{c1}(3872)\phi$	PHSP

Table 3.5: Decay modes for the $B_s^0 \to c\bar{c}X$ background event generation.

Figure 3.16 shows distributions for $B_s^0 \to c\bar{c}X$ background studied from an MC sample of 20 million events. The distributed events are scaled to the expected events in the data. It is worth emphasizing that the tagged components exist at the generated level. The selected events have correctly reconstructed J/ψ more than 95% of the time, whereas a random combination of photons or a π^0 from the other end satisfies the $B_s^0 \to J/\psi\pi^0$ selection criteria. We will parameterize the PDFs for signal and background distributions in the next chapter.

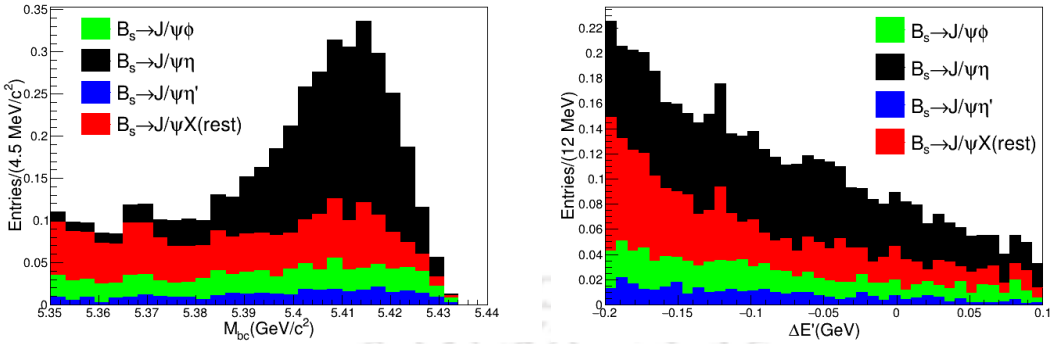

(a) (b)

Figure 3.16: Stacked distributions of $B_s \to c\bar{c}X$ background sampled from an MC data of 20M events: (a) $M_{\rm bc}$ and (b) $\Delta E'$. The distributions are scaled to the equivalent data luminosity. The colored filled histograms represent the selected candidates in $B_s^0 \to J/\psi\eta'$ (blue), $B_s^0 \to J/\psi\eta$ (black), $B_s^0 \to J/\psi\phi$ (green), and the other generated events with charmonium.

3.6 Summary

We have discussed the event reconstruction following the blind analysis procedure. A detailed description of the MC event generation, particle identification, $B_s^0 \to J/\psi\pi^0$ reconstruction and selection criteria determination using the MC data, and pre-estimation of the background components are provided in this chapter. We have also discussed the data skimming using the Hadron-B(J/ψ) criteria. The next chapter will discuss the signal and background PDF parameterization, the control sample study to check the correctness of the algorithm and MC versus data discrepancies, and the bias estimation in signal extraction.

Chapter 4

Maximum Likelihood Fit Analysis

4.1 Introduction

This chapter reviews the method used to extract the signal yield from the data and provides a detailed fit procedure for parameterizing the $M_{\rm bc}$ and $\Delta E'$ distributions of the signal and background events. Further, an analysis of the decay $B^0_d \to J/\psi\pi^0$ at $\Upsilon(4S)$ resonance is presented to validate the algorithm for event reconstruction and selection and to demonstrate the agreement between the MC simulated and actual data distributions. We also show the results of an investigation of the MC-simulated toy ensembles to estimate the fit bias in extracting the signal yield. In the last section of the chapter, we report the fit results for the selected $B^0_s \to J/\psi\pi^0$ candidates from the e^+e^- collision data.

4.2 Maximum Likelihood Method

Let us consider an experiment whose outcome is a continuous random variable x. The possible values of the variable x form an abstract space called the sample space Ω. The probability that the outcome of the measurement is in $[x, x+dx]$, is given by

$$\text{probability that the measurement } x \text{ to be in } [x, x+dx] = f(x;\theta)dx \qquad (4.1)$$

where the $f(x;\theta)$ is the probability distribution function (PDF), and the θ (or a vector of m parameters, $\boldsymbol{\theta} = \{\theta_1, \ldots, \theta_m\}$) is a parameter characterizing the behavior of the function. Now, suppose that the outcome of an experiment is a random vector of n continuous variables, $\boldsymbol{x} = (x_1, \ldots, x_n)$, and the measurement of $\boldsymbol{x}$ is repeated N times, measuring n values at each instant. The total sample from the entire experiment can be represented as $(x^1_1, \ldots, x^1_n), \ldots, (x^N_1, \ldots, x^N_n)$. The variables x^i_j can take any possible value in Ω. Further, each measurement of $\boldsymbol{x}$ is assumed to be independent. Under the assumption that the outcome of a measurement of $\boldsymbol{x}$ is distributed according to the PDF $f(x_1, \ldots, x_n; \boldsymbol{\theta})$ with the hypothesized values of parameters (actual values of the parameters are unknown), the probability that the

values of the first measurement of $\boldsymbol{x}$ to be in $[\boldsymbol{x}^1, \boldsymbol{x}^1 + d\boldsymbol{x}^1]$, the second one to be in $[\boldsymbol{x}^2, \boldsymbol{x}^2 + d\boldsymbol{x}^2]$, and so forth, is given by

$$\text{probability that, for all } i, \text{ the values } \boldsymbol{x}^i \text{ to be in } [\boldsymbol{x}^i, \boldsymbol{x}^i + d\boldsymbol{x}^i] = \prod_{i=1}^{N} f(x_1^i, \ldots, x_n^i; \boldsymbol{\theta}) dx_1^i \ldots dx_n^i. \tag{4.2}$$

For the assumed PDF, the probability will be maximum if the hypothesized values of the parameters are correct. Conversely, since dx_j^i is independent of parameters, therefore, for a given data sample, the values of the unknown parameters can be estimated for which the likelihood function (L), defined as

$$L(\boldsymbol{x}^1, \ldots, \boldsymbol{x}^N; \boldsymbol{\theta}) = \prod_{i=1}^{N} f(x_1^i, \ldots, x_n^i; \boldsymbol{\theta}), \tag{4.3}$$

is maximum. The solutions to the Equation 4.4 give the maximum likelihood (ML) estimators of unknown parameters,

$$\frac{\partial L(\boldsymbol{x}^1, \ldots, \boldsymbol{x}^N; \boldsymbol{\theta})}{\partial \theta_i} = 0, \tag{4.4}$$

where the estimators are represented with hats $\hat{\boldsymbol{\theta}} = \{\hat{\theta}_m, \ldots, \hat{\theta}_m\}$ to distinguish them from the actual values $(\theta_1, \ldots, \theta_m)$. The ML estimators which maximize the L also maximize the logarithmic of the L due to the monotonously increasing property of the logarithm function. Therefore, to make the computation more convenient where the multiplications turn into summations, the logarithmic of the likelihood function is maximized. The log-likelihood function is given as

$$\ln L(\boldsymbol{x}^1, \ldots, \boldsymbol{x}^N; \boldsymbol{\theta}) = \sum_{i=1}^{N} \ln f(x_1^i, \ldots, x_n^i; \boldsymbol{\theta}). \tag{4.5}$$

If the entire experiment with N measurements of the vector $\boldsymbol{x}$ is repeated a large number of times, then the estimate of the PDF parameters will follow the distributions. The mean and standard deviation of the distribution infer the actual value and uncertainty in estimating the parameter. For a given PDF and a set of N measurements, the uncertainty corresponding to an estimator is provided by the variance ($V[\hat{\theta}_j]$), defined as

$$V[\hat{\theta}_j] = \int \cdots \int (\theta_j - \hat{\theta}_j)^2 \prod_{i=1}^{N} f(x_1^i, \ldots, x_n^i; \boldsymbol{\theta}) dx_1^i \ldots dx_n^i, \tag{4.6}$$

where θ_j is the true value of the j^{th} parameter. The covariance of the different parameter estimators is defined as,

$$V[\hat{\theta}_{jk}] = \int \cdots \int (\theta_j - \hat{\theta}_j)(\theta_k - \hat{\theta}_k) \prod_{i=1}^{N} f(x_1^i, \ldots, x_n^i; \boldsymbol{\theta}) dx_1^i \ldots dx_n^i. \tag{4.7}$$

An ideal estimator must be consistent, unbiased, and efficient. The consistency of an estimator is defined in terms of the probability that for an infinitely large sample, the estimated value of a parameter must converge to the actual unknown value of the parameter, i.e.,

$$\forall \epsilon \lim_{N\to\infty} P(|\hat{\theta} - \theta| < \epsilon) = 1. \tag{4.8}$$

An estimator is said to be unbiased if the expected value of a parameter is equal to the actual value of the parameter. The bias b of an estimator is defined as,

$$b = E[\hat{\theta}] - \theta, \tag{4.9}$$

where $E[\hat{\theta}]$ is the expected value of parameter defined as,

$$E[\hat{\theta}] = \int \cdots \int \hat{\theta} \prod_{i=1}^{N} f(x_1^i, \ldots, x_n^i; \boldsymbol{\theta}) dx_1^i \ldots dx_n^i. \tag{4.10}$$

An estimator is efficient if its variance is equal to or less than the Cramér-Rao bound [57, 58] on the variance. In general, for large samples, the ML estimators satisfy all the properties. Further detail on the ML method can be found in the References [59, 60].

4.2.1 Extended Maximum Likelihood

Suppose that the N measurements of the vector $\boldsymbol{x}$ is also an outcome of the experiment; e.g., if the entire particle physics experiment consisting of N measurements is repeated a large number of times for equal intervals, then the outcome N will be Poisson distributed with a mean (μ) equal to the expected number of events. The likelihood function given by the equation 4.3 can be extended to include the parameter μ according to which the probability of N is distributed. The extended likelihood function is defined as

$$L(\boldsymbol{x}^1, \ldots, \boldsymbol{x}^N, N; \boldsymbol{\theta}, \mu) = \frac{\mu^N}{N!} e^{-\mu} \prod_{i=1}^{N} f(x_1^i, \ldots, x_n^i; \boldsymbol{\theta}), \tag{4.11}$$

where in general, μ can be a function of $\boldsymbol{\theta}$. The PDF for $\boldsymbol{x}$ is generally a combination of different components corresponding to different categories of events, e.g., the 'signal' and 'background' PDFs with the corresponding unknown estimates of μ_s and μ_b, respectively. The sum of μ_s and μ_b is equal to μ. The total PDF for $\boldsymbol{x}$ is expressed as

$$L(\boldsymbol{\theta}, \mu_s, \mu_b) = \frac{e^{-(\mu_s+\mu_b)}}{N!} \prod_{i=1}^{N} \left(\mu_s f_s(x_1^i, \ldots, x_n^i; \boldsymbol{\theta}) + \mu_b f_b(x_1^i, \ldots, x_n^i; \boldsymbol{\theta})\right), \tag{4.12}$$

where the notion of experimental outcomes is not represented explicitly for L, and f_s and f_b are the PDFs characterizing the signal and background events. Since N

is independent of the PDF parameters, the logarithm of the extended likelihood function, while dropping the term for N, is given by

$$\ln L(\boldsymbol{\theta}, \mu_s, \mu_b) = -\mu_s - \mu_b + \sum_{i=1}^{N} \left(\mu_s f_s(x_1^i, \ldots, x_n^i; \boldsymbol{\theta}) + \mu_b f_b(x_1^i, \ldots, x_n^i; \boldsymbol{\theta})\right). \quad (4.13)$$

The values of the μ_s and μ_b are estimated along with the other unknown parameters of the PDF using the ML estimators.

The analysis presented in this thesis uses the RooFit package [61] within the ROOT framework [62] to parameterize the distributions. The parameters and the corresponding statistical uncertainties are estimated by invoking the MINUIT package [63, 64], which implements the MIGRAD algorithm to find the parameter estimates for which the negative of the log-likelihood function given in the equation 4.13, is minimum and the MINOS algorithm to compute the uncertainties. We use the unbinned extended ML method to estimate the unknown parameters of the PDFs, where the unbinned data is used due to the limited statistics.

In the following sections, we discuss the PDF parameterization of the signal and background distributions of $M_{\rm bc}$ and $\Delta E'$ variables.

4.3 Signal PDF parameterization

As mentioned in the previous chapter, section 3.3.5, the linear correlation coefficient between the variables $M_{\rm bc}$ and $\Delta E'$ is less than 3%. Therefore, we implement a two-dimensional (2D) PDF fit procedure using an extended maximum likelihood method for the unbinned data. Individual PDFs for the $M_{\rm bc}$ and $\Delta E'$ variables are multiplied to obtain the 2D PDF.

We have generated large MC signal samples to parameterize the peaks attributed to the production modes of $\Upsilon(5S) \to B_s^0 \bar{B}_s^0$, $B_s^0 \bar{B}_s^{0*}$ or its CC pair and $B_s^{0*} \bar{B}_s^{0*}$. $M_{\rm bc}$ distributions from the first two production modes are fitted using the two Gaussian (G) functions with a common mean, where the projections of the 1D fit are shown in Figure 4.1. The bottom histograms are the pull distributions representing the quality of data fit. Table 4.1 lists the PDF parameters and the corresponding best-fit values using the MC data. The $M_{\rm bc}$ distribution of the signal candidates attributed to $B_s^{0*} \bar{B}_s^{0*}$ production is parameterized using a Crystal Ball (CB) function [65]. The function is briefly described in Appendix B. The final PDF for the signal $M_{\rm bc}$ distribution is determined by adding the CB component with the two Gaussian components using the measured fractions of $f_{B_s^{0*}\bar{B}_s^{0*}}$ and $f_{B_s^{0*}\bar{B}_s^{0}}$, as given in equations 2.4 and 2.5, respectively. $\Delta E'$ distribution for the signal is fitted with a combination of CB and G, sharing a common mean.

Figure 4.2 shows the 2D fit results of the selected $B_s^0 \to J/\psi\pi^0$ candidates in the signal MC data. The upper and lower rows show the distributions for the muon and electron sectors, respectively. In contrast, the fit results for the combined MC data are shown in Figure 4.3. PDF parameters for the leftmost and middle peaks of the $M_{\rm bc}$ distributions are fixed to the best-fit values, as listed in Table 4.1. Signal

Decay mode	Function	Parameter	Value (MC)
$\Upsilon(5S) \to B_s^0 \bar{B}_s^0$	1st Gaussian	Mean (MeV/c^2)	5366.28 ± 0.02
		Sigma (MeV/c^2)	3.43 ± 0.06
		Fraction	0.60 ± 0.02
	2nd Gaussian	Sigma (MeV/c^2)	7.43 ± 0.19
$\Upsilon(5S) \to B_s^0 \bar{B}_s^{0*}$ or CC	1st Gaussian	Mean (MeV/c^2)	5389.48 ± 0.02
		Sigma (MeV/c^2)	4.10 ± 0.05
		Fraction	0.75 ± 0.02
	2nd Gaussian	Sigma (MeV/c^2)	8.66 ± 0.22

Table 4.1: Fixed parameters for the composite signal PDF.

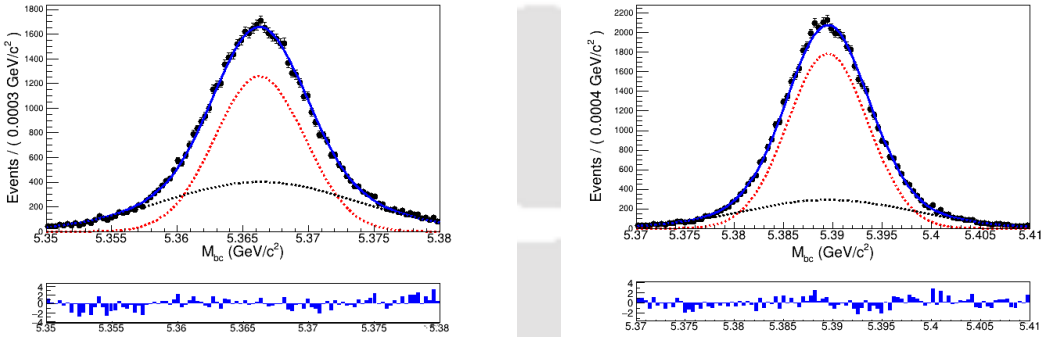

(a) (b)

Figure 4.1: Projections of the 1D fit to the $M_{\rm bc}$ distributions of the selected $B_s^0 \to J/\psi\pi^0$ candidates in MC data of (a) $\Upsilon(5S) \to B_s^0\bar{B}_s^0$ and (b) $\Upsilon(5S) \to B_s^0\bar{B}_s^{0*}$ (or CC) production modes. The points with error bars are the MC data, and the red and black dotted curves represent the Gaussian components of the total PDF (blue colored solid line). The bottom histograms are the pulled distributions per bin.

Var.	Function	Parameter	Value (μ-channel)	Value (e-channel)	Value (Both)
M_{bc}	CB	Mean (MeV/c^2)	5412.33 ± 0.03	5412.33 ± 0.03	5412.33 ± 0.02
		Sigma (MeV/c^2)	4.12 ± 0.02	4.15 ± 0.03	4.14 ± 0.02
$\Delta E'$	CB	Mean (MeV/c^2)	1.36 ± 0.76	0.13 ± 0.64	0.79 ± 0.51
		Sigma (MeV/c^2)	21.05 ± 0.96	21.06 ± 0.85	21.11 ± 0.65
	G	Sigma (MeV/c^2)	35.29 ± 2.70	32.90 ± 1.52	34.30 ± 1.50

Table 4.2: PDF parameter comparison among the muon, electron, and combined sectors.

PDF parameters for the electron and muon channels and the combined data are compared in Table 4.2. Shown uncertainties in the table are statistical only. As can be seen, the PDF parameter estimates agree among the three cases within the statistical uncertainties. Further, the expected background from the actual data is

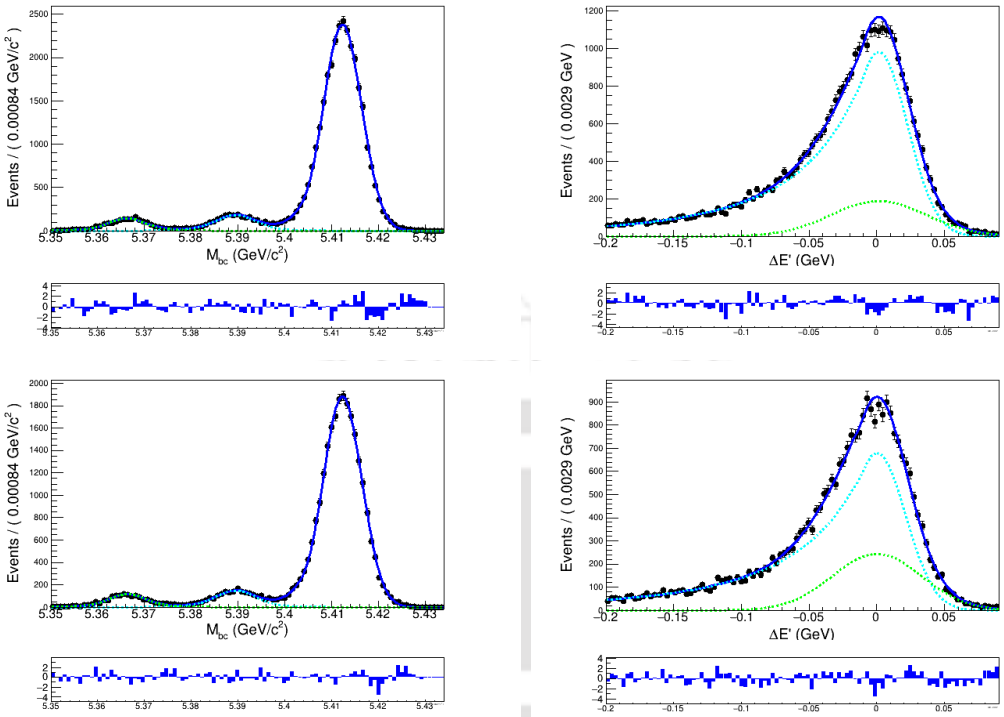

Figure 4.2: Projections of the 2D PDF (blue colored solid line) fit to the selected $B_s^0 \to J/\psi\pi^0$ candidates in signal MC data: muon-sector (upper row) and electron-sector (lower row). Points with error bars exhibit the $M_{\rm bc}$ (left) and $\Delta E'$ (right) distributions. A CB and two double G functions are used to fit the $M_{\rm bc}$ distributions. PDF components for the $\Delta E'$ distributions are shown using the cyan (CB) and green (G) dotted lines. The bottom histograms are distributions of the pull per bin.

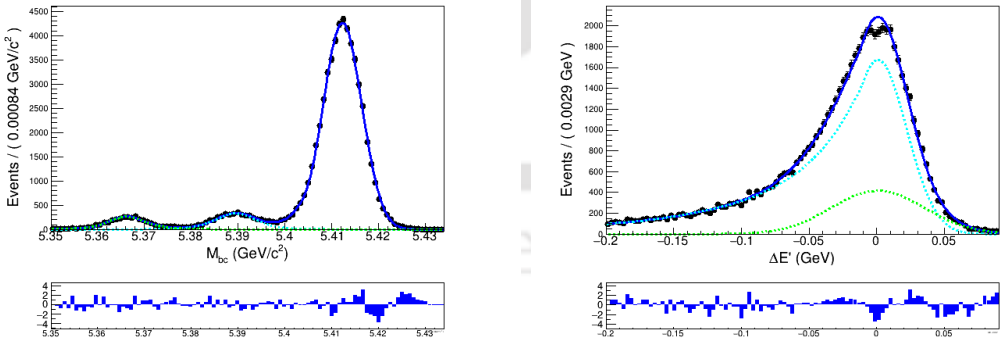

(a) (b)

Figure 4.3: Projections of the 2D PDF (solid blue colored line) fit to the combined signal MC candidates from electron and muon sectors: (a) $M_{\rm bc}$ and (b) $\Delta E'$ distributions. Points with error bars exhibit the MC data of combined electron and muon sectors. A CB and two double G functions are used to fit the $M_{\rm bc}$ distribution. PDF components for the $\Delta E'$ distribution are shown using the cyan (CB) and green (G) dotted lines. The bottom histograms are distributions of the pull per bin.

low, which is suitable for the rare decay analysis, but it has a disadvantage while parameterizing the background PDF due to the limited statistics. Therefore, we combine the $B_s^0 \to J/\psi\pi^0$ candidates from electron and muon sectors for further analysis.

4.4 Background PDF parameterization

The background events at $\Upsilon(5S)$ resonance satisfying the $B_s^0 \to J/\psi\pi^0$ selection criteria are divided into the following categories:

(a) Continuum,

(b) $B_d^0 \to J/\psi\pi^0$,

(c) non-bsbs excluding the $B_d^0 \to J/\psi\pi^0$ events, and

(d) bsbs.

Since the continuum and non-bsbs (excluding the $B_d^0 \to J/\psi\pi^0$ mode) have similar distributions, these events are fitted together to determine the shapes of combinatorial backgrounds. Contrary to this, the remaining types have dedicated PDFs, as illustrated in this section.

4.4.1 Background PDF for the combinatorial events

We use six streams of officially available $e^+e^- \to q\bar{q}$ ($q = u, d, s,$ and c) MC data to determine the shape of the continuum background. In contrast, a dedicated MC sample of 10 million events is used to parameterize the distributions from $B \to c\bar{c}X$ decays. This is worth mentioning that the $B_d^0 \to J/\psi\pi^0$ mode is treated separately. For the $M_{\rm bc}$ and $\Delta E'$ distributions, respectively, the ARGUS function [66] and first-order Chebyshev polynomial are used to fit the data. The functional form of the ARGUS and Cheychev polynomials are described in Appendix B. Figure 4.4 shows the results of the 2D fit to the distributions of selected candidates in the continuum (upper row) and $B \to c\bar{c}X$ (lower row) MC data. The endpoints of the ARGUS functions are fixed to 5.433 GeV/c^2, whereas the curvature of the ARGUS function and slope of the polynomial are floated. Since the background distributions can be fitted using similar PDFs and the parameters are floated to be determined during the fit, we add the two background components to obtain a single PDF. Figure 4.5 shows the 2D fit results to the distributions from combined MC data. The $B_d^0 \to J/\psi\pi^0$ mode is parameterized in the following subsection.

4.4.2 Background PDF for the $B_d^0 \to J/\psi\pi^0$ events

The non-bsbs background has distinctive distributions from the $B_d^0 \to J/\psi\pi^0$ events. We use the `RooHistPdf` class of the `RooFit` package, which implements a non-parametric PDF sampled from a multidimensional histogram, to model the $B_d^0 \to$

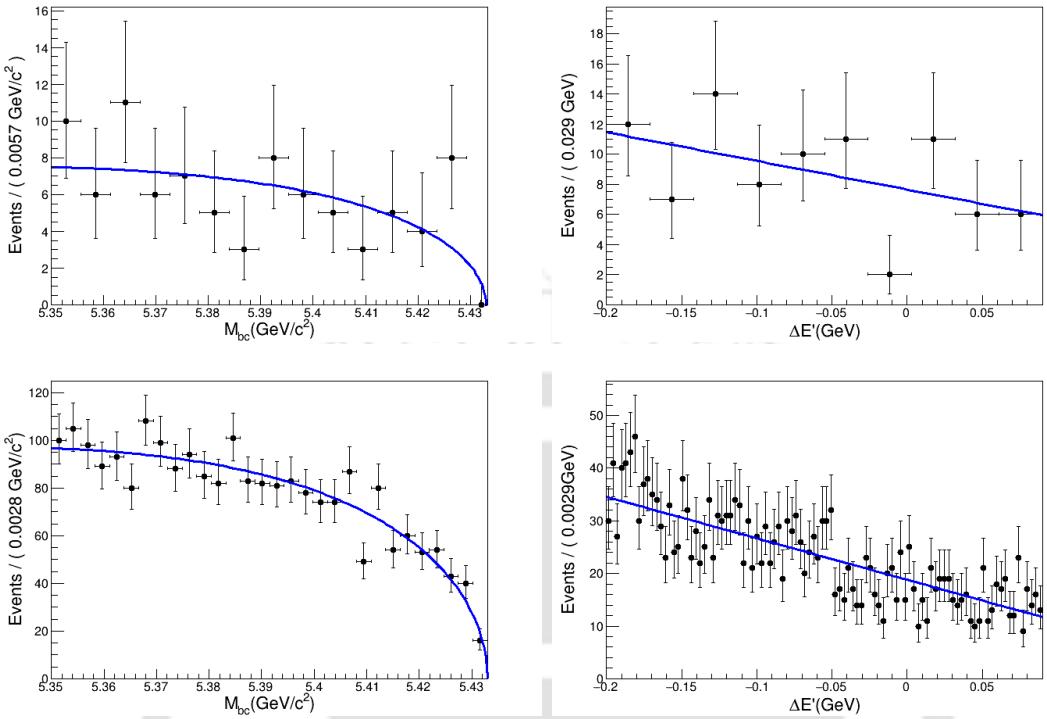

Figure 4.4: Projections of the 2D PDF fit to the distributions of the selected candidates from the MC samples consisting of six streams of the continuum (upper row) and 10 million $B \to c\bar{c}X$ events (lower row), where $B^0_d \to J/\psi\pi^0$ mode is excluded from the latter. Points with error bars are the MC data. Blue-colored solid lines represent the fitted ARGUS function for the $M_{\rm bc}$ (left) distributions and first-order Chebychev polynomial for the $\Delta E'$ (right) distributions.

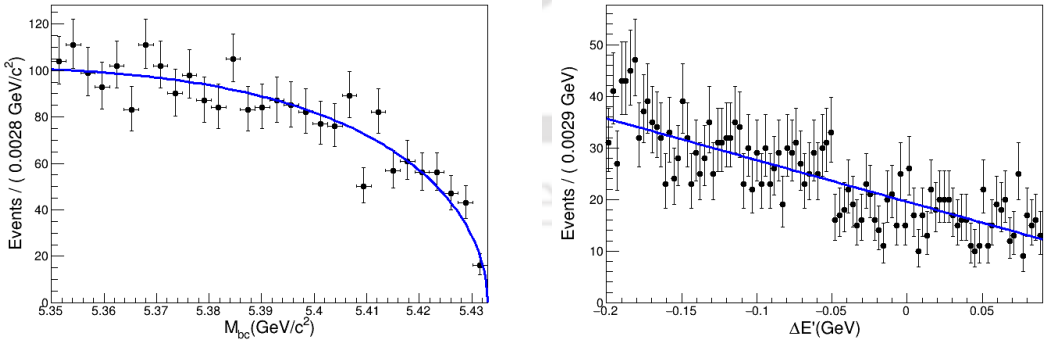

(a) (b)

Figure 4.5: Projections of the 2D PDF fit to the distributions of selected candidates from the combined MC data of continuum (six streams) and $B \to c\bar{c}X$ (10 million) events, where $B^0_d \to J/\psi\pi^0$ mode is excluded from the latter. Points with error bars are the MC data. Blue-colored solid lines represent the fitted ARGUS and first-order Chebychev polynomial for the $M_{\rm bc}$ (left) and $\Delta E'$ (right) distributions.

$J/\psi\pi^0$ events. Figure 4.6 shows the projections of the 2D fit results, where the histogram PDF is sampled from the MC data of 200,000 $B_d^0 \to J/\psi\pi^0$ events.

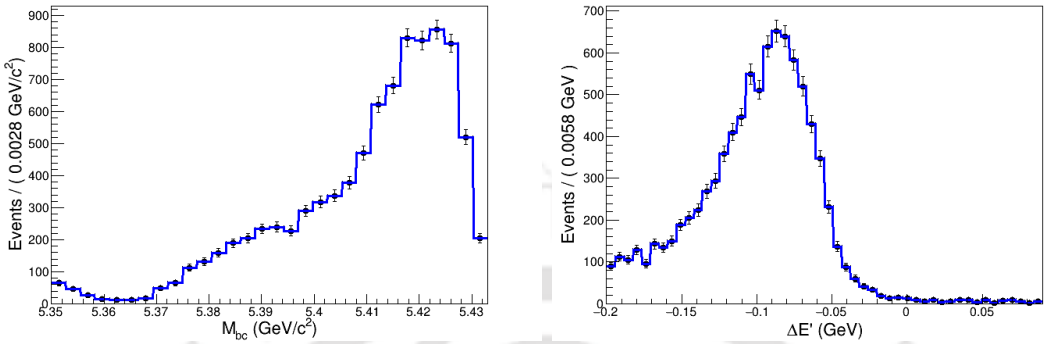

(a) (b)

Figure 4.6: Projections of the 2D non-parametric histogram PDF to the selected candidates in $B_d^0 \to J/\psi\pi^0$ MC data: (a) $M_{\rm bc}$ and (b) $\Delta E'$ distributions. Points with error bars are the MC data, whereas the blue-colored solid line represents the histogram PDF.

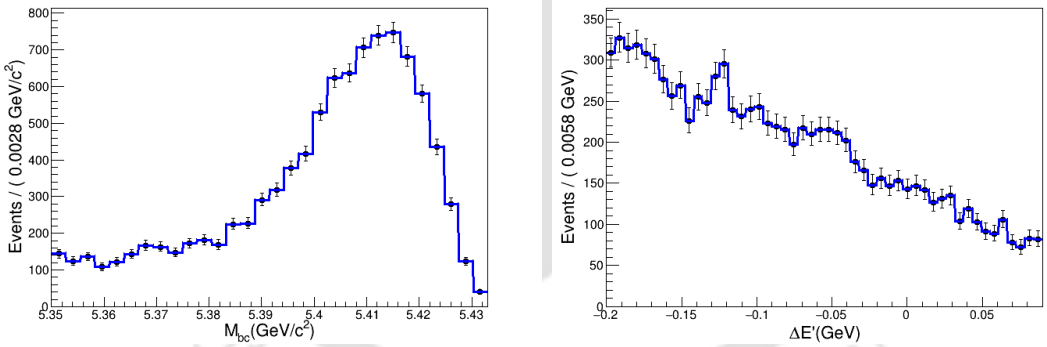

(a) (b)

Figure 4.7: Projections of the 2D non-parametric PDF to the selected candidates in $B_s^0 \to c\bar{c}X$ MC data: (a) $M_{\rm bc}$ and (b) $\Delta E'$ distributions. Points with error bars represent the MC data, whereas the blue-colored solid line represents the histogram PDF.

4.4.3 PDF parameterization of the bsbs background

As mentioned in the section 3.5.2, the bsbs background component is dominated by the $B_s^0 \to c\bar{c}X$ decays, where a correctly reconstructed J/ψ and a random combination of photons or a π^0 from the other end satisfy the $B_s^0 \to J/\psi\pi^0$ selection criteria. We model this background using a dedicated MC sample of 20 million $B_s^0 \to c\bar{c}X$

events and implement a 2D non-parametric histogram PDF. Figure 4.7 shows the projection of 2D fit to the distributions of selected candidates in the MC data.

4.5 Control Sample Study

So far, we discussed the parameterization of distributions for signal events using the simulated data. However, there can be a between data and MC, which needs to be estimated. Further, the algorithm used for selecting the signal candidates should be cross-checked. For this, we study the $B_d^0 \to J/\psi\pi^0$ at $\Upsilon(4S)$ as a control mode with the similar final state particles as of $B_s^0 \to J/\psi\pi^0$. The PDG average and the previous measurement of the branching fraction $\mathcal{B}(B_d^0 \to J/\psi\pi^0)$ at Belle experiment are $(1.66 \pm 0.10) \times 10^{-5}$[1] and $(1.62 \pm 0.11) \times 10^{-5}$[26], respectively, where the uncertainties are statistical only.

4.5.1 $B_d^0 \to J/\psi\pi^0$ Selection and PDF Parameterization using MC data

We have generated an extensive MC sample of 200,000 $B_d^0 \to J/\psi\pi^0$ events at $\Upsilon(4S)$ resonance. The data sample includes both the electron and muon sectors in equal proportion. Decay models used for generating the events are similar to the target analysis. Except for the $M_{\rm bc}$ requirement, the $B_d^0 \to J/\psi\pi^0$ candidates are selected based on the criterion given in Table 3.3. We define the $\Delta E'$ variable for the control sample as:

$$\Delta E' = \Delta E + M_{\rm bc} - m_{B_d^0}, \tag{4.14}$$

where $m_{B_d^0} = 5279.65$ MeV/c^2 is nominal mass of B_d^0 meson [1].

We then perform a 2D fit to the $M_{\rm bc}$ and $\Delta E'$ distributions of the selected B_d^0

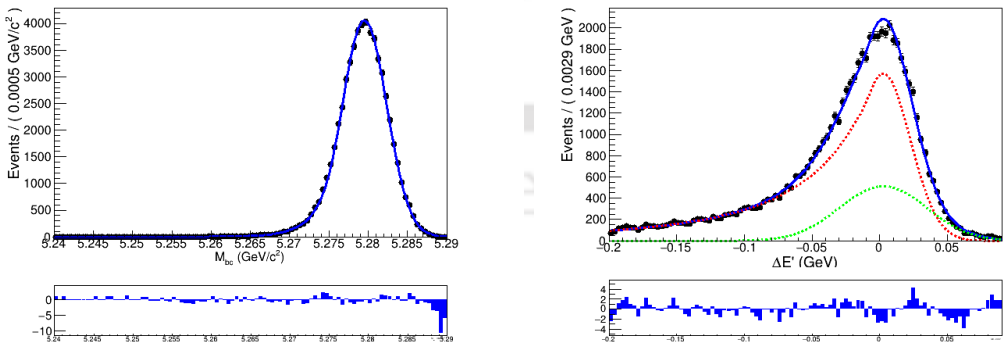

(a) (b)

Figure 4.8: Projections of the 2D fit to the distributions of selected candidates in the $B_d^0 \to J/\psi\pi^0$ MC data: (a) $M_{\rm bc}$ and (b) $\Delta E'$ distributions. Points with error bars are the MC data, whereas the solid blue line is the total PDF. Red and green colored dotted lines for $\Delta E'$ distribution represent the CB and G components, respectively.

candidates. The $M_{\rm bc}$ distribution of the signal events is fitted with a CB function, whereas the $\Delta E'$ distribution is fitted with a combination of CB and G functions with a common mean. Figure 4.8 shows the maximum unbinned likelihood fit results to the selected candidates in the $B^0_d \to J/\psi\pi^0$ MC data.

As we have seen earlier for the target mode, the dominant background is associated with the $B\bar{B}$ decays containing correctly reconstructed J/ψ, i.e., the $B \to c\bar{c}X$ decays. The reconstructed J/ψ candidate and a random combination of photons or π^0 from the other sources satisfy the $B^0_d \to J/\psi\pi^0$ selection criteria. To parameterize this background, we analyze an MC-simulated sample with 100 times more statistics than the expected $b \to c\bar{c}q$ events in data. The data sample is officially available at Belle. The $M_{\rm bc}$ and $\Delta E'$ distributions for such events are modeled using a non-parameterized 2D histogram PDF. Figure 4.9 shows the projections of the 2D fit results.

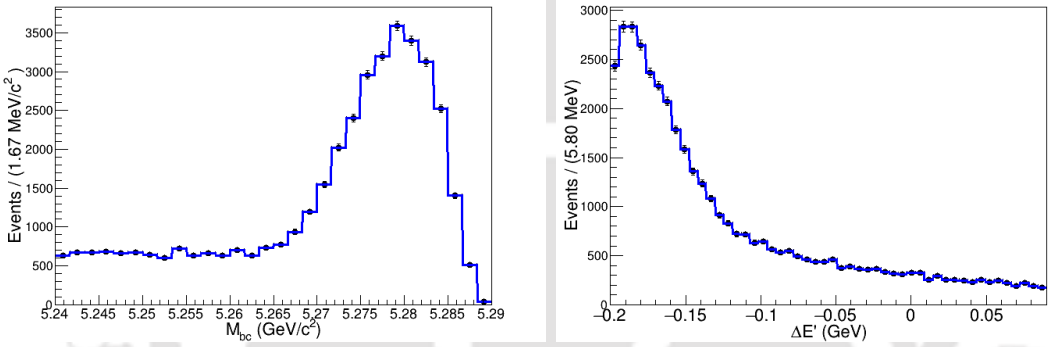

(a) (b)

Figure 4.9: Projections of the 2D PDF fit to the selected candidates in the MC simulated $B \to c\bar{c}X$ data: (a) $M_{\rm bc}$ and (b) $\Delta E'$ distributions. Points with error bars are the MC data, whereas the blue-colored solid line represents the fitted histogram PDF.

The remaining background in selecting the $B^0_d \to J/\psi\pi^0$ candidates is from the continuum production. For this background, we have analyzed an MC sample with six times more statistics than the actual data. The $M_{\rm bc}$ distribution of the continuum background is parameterized using an ARGUS function with an endpoint at 5.289 GeV/c^2, and the $\Delta E'$ distribution is fitted with a first-order Chebychev polynomial. Projections of the 2D PDF fit results to the MC simulated continuum background are shown in Figure 4.10.

4.5.2 Real Data Unblinding and the Correction Factors

We have selected the $B^0_d \to J/\psi\pi^0$ candidates from the actual e^+e^- collision data at $\Upsilon(4S)$ resonance based on the selection criteria as determined using the MC simulation. The data analyzed for this study corresponds to the total integrated luminosity of 570 fb^{-1}. We follow a 2D PDF fit procedure using an unbinned

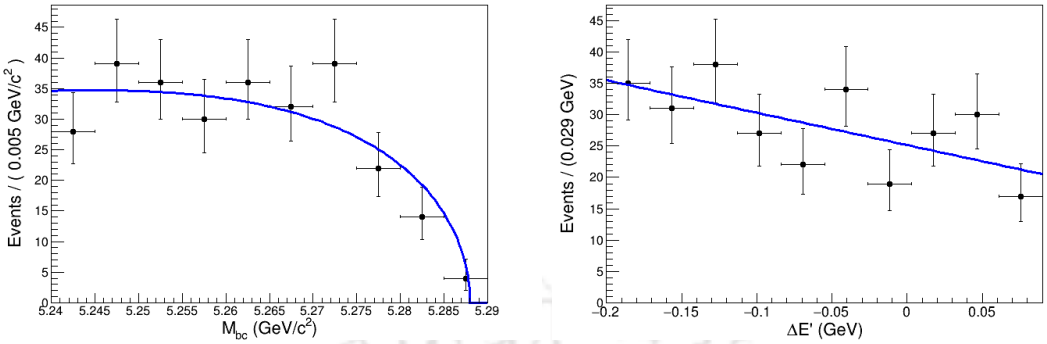

(a) (b)

Figure 4.10: Projection of the 2D PDF fit to the selected candidates in the MC simulated background consisting of six streams of continuum events: (a) $M_{\rm bc}$ and (b) $\Delta E'$ distributions. Points with error bars are the MC data. The blue-colored solid lines represent the fitted ARGUS function and first-order Chebychev polynomial for the $M_{\rm bc}$ and $\Delta E'$ distributions, respectively.

extended maximum likelihood method to extract the signal yield from the selected B^0_d candidates. The PDFs for the signal and background events are described in the previous subsection. The means and resolutions of the signal PDF and the signal and background yields are floated during the data fit. The power-law tail-end parameters of the CB functions are fixed to the estimated values using the MC simulated signal data. Figure 4.11 shows the fit results to the selected B^0_d candidates in the data. We have observed 369.0 ± 26.6 signal events with an efficiency of $(30.9 \pm 0.1)\%$, where the uncertainties are statistical only.

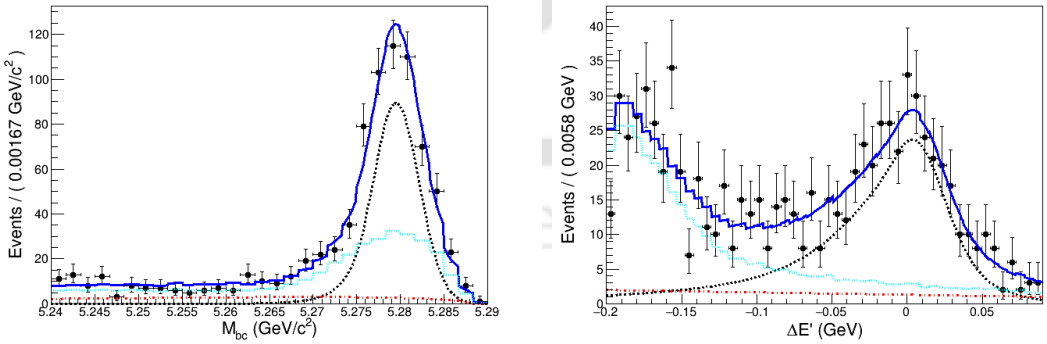

(a) (b)

Figure 4.11: Projections of the fit to selected $B^0_d \to J/\psi\pi^0$ events in the e^+e^- collision data having $(619.20 \pm 9.44)\times10^6$ $B\bar{B}$ mesons at $\Upsilon(4S)$ resonance: (a) $M_{\rm bc}$ and (b) $\Delta E'$ distributions. Black points with error bars represent the data. Dashed (black), dotted (cyan), dash-dotted (red), and solid (blue) lines are the signal, $b \to c\bar{c}q$, continuum, and total PDFs, respectively.

The branching fraction of $B^0_d \to J/\psi\pi^0$ is calculated from the observed signal yield ($Y_{\rm sig}$), as:

$$\mathcal{B}(B^0_d \to J/\psi\pi^0) = \frac{Y_{\rm sig}}{N_{B\bar{B}} \times \epsilon \times \mathcal{B}_{J/\psi} \times \mathcal{B}_{\pi^0}} \ , \tag{4.15}$$

where $N_{B\bar{B}} = (619.20 \pm 9.44) \times 10^6$ are the number of $B\bar{B}$ mesons; ϵ is the signal selection efficiency; $\mathcal{B}_{J/\psi}$ is the sum of $\mathcal{B}(J/\psi \to e^+e^-)$ and $\mathcal{B}(J/\psi \to \mu^+\mu^-)$[1]; and $\mathcal{B}_{\pi^0}$ is the branching fraction of $\pi^0 \to \gamma\gamma$[1]. We measure the branching fraction of $\mathcal{B}(B^0_d \to J/\psi\pi^0)$ to be $(1.63 \pm 0.13) \times 10^{-5}$, where the uncertainties in the $N_{B\bar{B}}$ and branching fraction measurement are statistical only. This result is in excellent agreement with the previous measurement by Belle [26] and the PDG average [1] within 1σ statistical uncertainty.

Table 4.3 lists the parameter values of the signal PDF estimated using the simulated and actual data. The slight discrepancies are computed as the shift in the means and the fudge factor for the widths, which are defined as:

$$\text{Shift in the mean} = \mu_{\rm data} - \mu_{\rm MC}, \tag{4.16}$$

$$\text{Fudge factor for the sigma} = \frac{\sigma_{\rm data}}{\sigma_{\rm MC}}. \tag{4.17}$$

The signal PDF parameters and the corresponding correction factors are given in Table 4.4. We have computed a common fudge factor for the widths corresponding to PDF components of the $\Delta E'$ distribution.

Variable	Function	Parameter	Value (MC)	Value(Data)
M_{bc}	Crystal Ball	Mean (MeV/c^2)	5279.53 ± 0.02	5279.6 ± 0.17
		Sigma (MeV/c^2)	2.85 ± 0.01	2.52 ± 0.15
$\Delta E'$	Crystal Ball	Mean (MeV)	2.53 ± 0.44	1.68 ± 2.92
		Sigma (MeV)	19.88 ± 0.55	20.71 ± 4.25
	Gaussian	Sigma (MeV)	31.95 ± 0.99	34.04 ± 8.85

Table 4.3: List of values for mean and sigma of the signal PDF.

Variable	Parameter	Correction Factor
M_{bc}	Shift in the mean (MeV/c^2)	0.07 ± 0.17
	Fudge factor for the sigma	0.89 ± 0.05
$\Delta E'$	Shift in the mean (MeV)	-0.94 ± 2.51
	Fudge factor for the sigma	1.05 ± 0.10

Table 4.4: Correction factors from the study of simulated and real data for $B^0_d \to J/\psi\pi^0$ decay at $\Upsilon(4S)$ resonance.

We find that the slight differences in the means and widths of the signal PDF are within the statistical uncertainties. The control sample study demonstrates excellent data and MC agreement in the signal PDF parameters and confirms the

correctness of the algorithm in selecting the signal events. The slight differences will be considered as a source of additional systematic uncertainty by varying the signal PDF parameters of the target analysis in accordance with the corresponding correction factors, as will be discussed in the next chapter.

4.6 Fit Validation using Toy MC

We perform a fit validation study using the MC-simulated toy ensembles. A stable fit model must extract the signal yield equal to the presence of actual signals in the data. A tendency to differ is estimated as a bias in the extracted signal yield. We estimate the fit bias using the ensembles corresponding to different assumptions of the number of signal events, each having 5000 identical toys. The toy signal events are selected randomly from the MC simulated $B_s^0 \to J/\psi\pi^0$ sample. In contrast, as determined by the MC simulation, the expected background of 45 events is extracted from the background PDFs described in section 4.4. The statistical fluctuations in the expected number of signal and background events are incorporated using the Poisson distribution. It is worth mentioning that of the total background events, the components $B_d^0 \to J/\psi\pi^0$, bsbs, and non-bsbs and continuum share the fixed fractions of 11.7%, 9.8%, and 78.5%, respectively. The percentages are computed using six streams of MC simulated data, as given in Appendix C.

The toy data is fitted with the 2D signal and background PDFs described in sections 4.3 and 4.4, respectively. The signal PDF parameters and endpoint of the ARGUS function are fixed to the best-fit values obtained using the MC simulated data, as listed in Table 4.5. The yields for the $B_d^0 \to J/\psi\pi^0$ and $B_s^0 \to c\bar{c}X$ PDFs are fixed to 5.17 ± 2.27 and 4.33 ± 2.08 events, respectively, as determined using six streams of MC data (see Appendix C). The yields for signal and combinatorial PDF and the parameters defining the ARGUS and Chebychev functions are floated during the fit. We fit the 2D PDF using the unbinned extended maximum likelihood method to each toy data, extracting the signal yield and computing the deviation from the actual signal events. The deviation ratio to the statistical uncertainty in the signal yield (σ_{Yield}), defined as the signal pull $\left(\frac{N_{\text{sig}}^{\text{Yield}} - N_{\text{sig}}^{\text{ensemble}}}{\sigma_{\text{Yield}}}\right)$, is used to quantify the fit bias; where $N_{\text{sig}}^{\text{Yield}}$ and $N_{\text{sig}}^{\text{ensemble}}$ are the extracted signal yield from the fit of a toy data and the mean number of input signals in each toy, respectively. Figure 4.12 shows the distributions of the extracted signal yield and signal pull from an ensemble having the input of an average of seven MC signals in each toy. The number is particular because of its correspondence to the estimated upper limit on the signal yield at 90% confidence level, as discussed in Chapter 6. We estimate a fit bias of $(5.5 \pm 1.5)\%$ using the entire range of distribution and assign a systematic uncertainty of $+0.23$ events, which is calculated by multiplying the fit bias by the statistical uncertainty in signal yield (width of the fitted yield distribution).

Figure 4.13 shows the linearity test for various input signals. A linear proportion with approximately a unit slope of the fitted signal yields with respect to the actual number of signal events demonstrates the stability of the fit model. A further

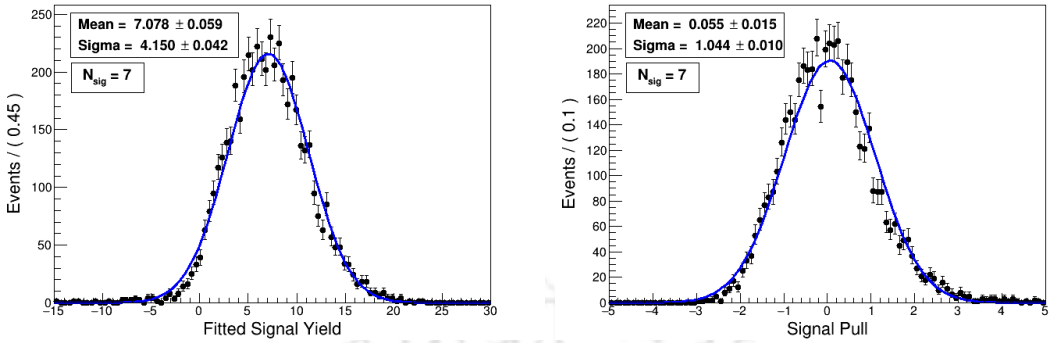

(a) (b)

Figure 4.12: Distributions of fitted signal yield and signal pull from an ensemble corresponding to an average of seven input signals.

description of the signal pull and fitted yield distributions is given in Appendix D.

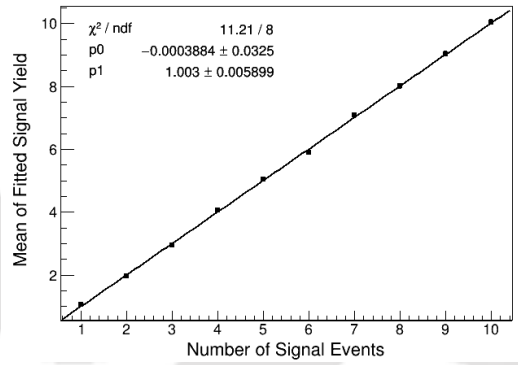

Figure 4.13: Mean of the fitted signal yields as a function of the actual number of signal events.

4.7 Real Data Unblinding

The $B_s^0 \to J/\psi\pi^0$ events from e^-e^+ collision data at $\Upsilon(5S)$ resonance are selected based on the criteria described in Table 3.3. We have analyzed the data corresponding to an integrated luminosity of 121.4 fb^{-1} to search for this decay. A 2D PDF based on the MC simulation, summarized in the previous section for the toy data, is used to extract the signal and background yields. The signal PDF parameters and the ARGUS function endpoint are fixed to the best-fit MC values, as listed in Table 4.5. The contributions of $B_d^0 \to J/\psi\pi^0$ and $B_s^0 \to c\bar{c}X$ PDFs are fixed to 5.17 ± 2.27 and 4.33 ± 2.08 events, respectively, as determined using six streams of MC data. The remaining parameters, which include the yields for the $B_s^0 \to J/\psi\pi^0$ signal and combinatorial background, and the curvature and slope of combinatorial PDF, are

Variable	$B_s^{0(*)}\bar{B}_s^{0(*)}$	Function	Parameter	MC Value
M_{bc}	$B_s^{0*}\bar{B}_s^{0*}$	CB	μ	5.412328 ± 0.000023
			σ	0.004135 ± 0.000018
			α	1.468 ± 0.048
			n	22 ± 16
			$f_{B_s^{0*}\bar{B}_s^{0*}}$	0.8701 ± 0.0016
	$B_s^{0*}\bar{B}_s^{0}$ or $B_s^{0}\bar{B}_s^{0*}$	Double-G with common mean	μ	5.389482 ± 0.000021
			σ (1st G)	0.004101 ± 0.000046
			σ (2nd G)	0.00866 ± 0.00022
			fraction (1st G)	0.748 ± 0.016
			$f_{B_s^{0*}\bar{B}_s^{0}}$	0.0748 ± 0.0014
	$B_s^{0}\bar{B}_s^{0}$	Double-G with common mean	μ	5.366281 ± 0.000020
			σ (1st G)	0.003428 ± 0.000056
			σ (2nd G)	0.00743 ± 0.00019
			fraction (1st G)	0.603 ± 0.021
	All	ARGUS	Endpoint	5.43272 ± 0.00023
$\Delta E'$	All	CB+G with common mean	μ	0.00079 ± 0.00051
			σ (CB)	0.02111 ± 0.00065
			α	0.450 ± 0.046
			n	3.63 ± 0.53
			σ (G)	0.0343 ± 0.0015
			fraction (CB)	0.802 ± 0.031
Events corresponding to $B_d^0 \to J/\psi\pi^0$ PDF				5.17 ± 2.27
Events corresponding to $B_s^0 \to c\bar{c}X$ PDF				4.33 ± 2.08

Table 4.5: List of the parameters fixed to best-fit values obtained from the MC simulation.

floated during the fit. The data is fitted using the unbinned extended maximum likelihood method. Figure 4.14 shows the fit results to the entire data set of e^+e^- collisions at $\Upsilon(5S)$ resonance. We obtain the yields for signal and combinatorial background of -0.01 ± 3.2 and 50.0 ± 4.0 events, respectively, where the uncertainties are statistical only. The negative signal yield is due to statistical fluctuations. The expected combinatorial background of 34.7 ± 5.9 events from the MC study exists within the 2.1 statistical uncertainty of the fitted yield, where the expected background is a normalized estimation of the six streams of MC data to the total integrated luminosity.

4.8 Summary

In this chapter, we have discussed the maximum likelihood fit method to estimate the PDF parameters and the PDF modeling of signal and background distributions. We have analyzed the $B_d^0 \to J/\psi\pi^0$ at $\Upsilon(4S)$ resonance as a control mode validating

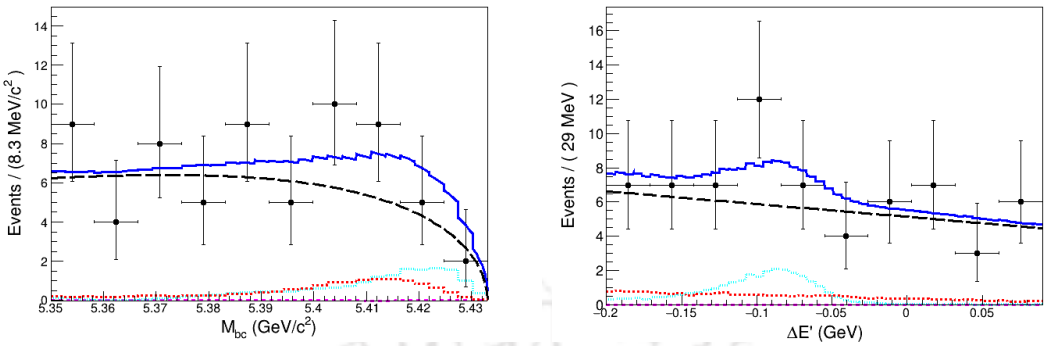

(a) (b)

Figure 4.14: Projections of the fit to selected $B_s^0 \to J/\psi\pi^0$ events in the 121.4 fb^{-1} of e^+e^- collision data at $\Upsilon(5S)$ resonance: (a) $M_{\rm bc}$ and (b) $\Delta E'$ distributions. Black points with error bars represent the data. Long-dashed (magenta), dashed (red), dotted (cyan), broken-line (black), and solid (blue) lines are the signal, $B_s^0 \to c\bar{c}X$, $B_d^0 \to J/\psi\pi^0$, a continuum with remaining $B \to c\bar{c}X$, and total PDFs, respectively.

the selection criteria. The slight discrepancy in the simulated and actual data from the control channel is considered an additional source of systematic uncertainty. Further, we have investigated the large MC toy ensembles to estimate the bias from the fitted PDF model. Finally, we have looked at the fit results of actual e^+e^- collision data and observed no $B_s^0 \to J/\psi\pi^0$ signal events. In the following chapters, we will discuss the various source of systematic uncertainties and the upper limit calculation on the branching fraction of $B_s^0 \to J/\psi\pi^0$.

Chapter 5

Systematic Uncertainties

5.1 Introduction

Measurement of a variable has uncertainties due to limited statistics, improper calibration of the instrument, and the procedure followed. In this analysis, the sources of uncertainties include PDF parameterization and biases, the discrepancy in the simulated and actual data, etc. The statistical uncertainty can be minimized by increasing the statistics whenever possible. Contrary to this, the uncertainties due to other sources are common to each measurement that repeated experiments cannot reduce. Therefore, it is essential to precisely estimate such uncertainties from all the sources while reporting a measurement. These uncertainties are known as systematic uncertainties. This chapter discusses the systematic uncertainty from all the known sources and assigns a total systematic uncertainty.

5.2 Sources of the Systematic Uncertainties

5.2.1 Charged Tracking Efficiency

Uncertainty from the charged track with momentum $P_t > 200$ MeV/c is calculated based on the ratio of data versus MC efficiencies of the partially reconstructed $D^{*+} \to D^0\pi^+$, $D^0 \to K^0_s\pi^+\pi^-$, and $K^0_s \to \pi^+\pi^-$ decays. A systematic uncertainty of 0.35% per track is assigned [67]. This analysis selects two charged tracks for the reconstruction of J/ψ. Therefore, a systematic uncertainty of 0.70% is assigned due to the tracking efficiency.

5.2.2 Lepton ID Efficiency

Systematics associated with the lepton identification is obtained from studying the two-photon process $\gamma\gamma \to l^+l^-$, which provides a large sample of electron and muon events [68]. An additional error from the hadronic environment effect on the data and MC efficiency is assigned using the inclusive $J/\psi \to l^+l^-$ events from B decays. Figure 5.1 shows the uncertainties in percentage for the different muon ID

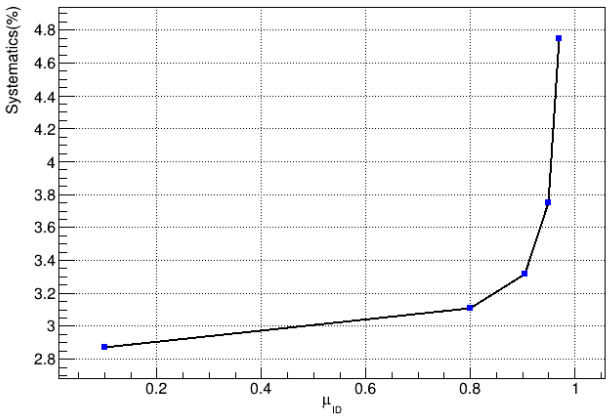

Figure 5.1: Systematic uncertainty (%) for the various $\mu_{\rm ID}$ requirements.

requirements calculated from the provided efficiency tables [69]. By interpolating the data points, we estimate a 2.95% uncertainty for the requirement of $\mu_{\rm ID} > 0.4$. The uncertainty due to electron identification is estimated to be 1.55%. We assign an average uncertainty of 2.25% per lepton due to the lepton identification, as the two sectors are not analyzed separately.

5.2.3 π^0 Reconstruction Efficiency

The uncertainty in the π^0 reconstruction is studied from $\tau^- \to \pi^0\pi^-\nu_\tau$ decays [70]. We assign a total systematic uncertainty of 2.2% from this source.

5.2.4 Mass-Vertex Constraint Fit Requirement of J/ψ

We estimate the uncertainty due to the goodness of mass-vertex constraint fit ($\chi^2_{\text{Mass-Vertex}}$) requirement to be less than 60 using the control channel $B^0_d \to J/\psi\pi^0$. The relative efficiencies of the condition in selecting the $B^0_d \to J/\psi\pi^0$ signal from the MC simulated and actual data at $\Upsilon(4S)$ resonance are found to be 0.9522 ± 0.0054 and 0.9736 ± 0.1058, respectively, where the uncertainties are statistical only. The deviation of the ratio of the data versus MC efficiencies (1.0225 ± 0.1088) from unity is evaluated as the associated systematic uncertainty. We assign an uncertainty of 2.25% due to the mass-vertex constraint fit requirement in J/ψ reconstruction.

5.2.5 Uncertainty due to the MC statistics

The signal selection efficiency of $(31.02 \pm 0.10)\%$ is determined in Section 3.4, where the uncertainty is statistical only. We assign the corresponding systematic uncertainty of 0.32% due to the limited MC statistics.

5.2.6 Uncertainty on $\mathcal{B}(J/\psi \to l^+l^-)$

We assign a 0.77% uncertainty due to the uncertainties on $J/\psi \to l^+l^-$ branching fraction measurements [1]. A total uncertainty is obtained by adding the fractional uncertainties in the individual modes in quadrature.

5.2.7 Uncertainty on $\mathcal{B}(\pi^0 \to \gamma\gamma)$

We assign an uncertainty of 0.03% from the measured branching fraction $\mathcal{B}(\pi^0 \to \gamma\gamma)$ of (98.823±0.034)% [1].

5.2.8 Uncertainty on the number of B_s^0 mesons

The total number of B_s^0 mesons is computed as

$$N(B_s^0) = 2 \times \mathcal{L}_{\rm int}^{\Upsilon(5S)} \times \sigma_{b\bar{b}}^{\Upsilon(5S)} \times f_s, \tag{5.1}$$

where, $\mathcal{L}_{\rm int}^{\Upsilon(5S)} = 121.4 \pm 1.6$ fb^{-1} is the total integrated luminosity; $\sigma_{b\bar{b}}^{\Upsilon(5S)} = 0.340 \pm 0.016$ nb is the $b\bar{b}$ production cross-section at $\Upsilon(5S)$ resonance [37]; and $f_s = \left(22.0^{+2.0}_{-2.1}\right)$ % is the $B_s^{0(*)}\bar{B}_s^{0(*)}$ production fraction of $b\bar{b}$ events [38]. We analyze $(18.16^{+1.87}_{-1.95}) \times 10^6$ B_s^0 decays to probe the $B_s^0 \to J/\psi\pi^0$ events and assign an uncertainty of $\left(^{+10.30}_{-10.74}\right)$%. A substantial component of this uncertainty is due to the statistical uncertainty of $\left(^{+9.09}_{-9.55}\right)$% in the measurement of the fraction f_s.

5.2.9 Uncertainty on the MC-based Fixed Background Yields

We estimate the systematic uncertainty on the MC-based fixed yields by incorporating the uncertainties on data luminosity, $B\bar{B}$ production fractions, measured branching fractions, etc., in addition to the total systematic uncertainty of 4.01% due to tracking and particle identification, reconstruction of the intermediate particles, and measured branching fractions of J/ψ and π^0, as discussed in the previous subsections.

(a) Fixed yield for the $B_d^0 \to J/\psi\pi^0$ component

We account for the uncertainties on the $\mathcal{L}_{\rm int}^{\Upsilon(5S)}$ (1.32%), $\sigma_{b\bar{b}}^{\Upsilon(5S)}$ (4.17%) [37], production fraction of $B\bar{B}X$ events at $\Upsilon(5S)$ resonance $\left(^{+3.54}_{-5.25}\right)$ % [1], and branching fraction measurement of $B_d^0 \to J/\psi\pi^0$ (6.02%) [1]. These uncertainties, along with the total uncertainty of 4.01% from particle identification and reconstruction, are added in quadrature, assigning a total systematic uncertainty of $\left(^{+9.42}_{-10.19}\right)$ %, which corresponds to an uncertainty of $\left(^{+0.49}_{-0.53}\right)$ events associated with the fixed yield of 5.17 $B_d^0 \to J/\psi\pi^0$ events. The yield for the $B_d^0 \to J/\psi\pi^0$ component based on the MC data is $5.17 \pm 2.27\ ^{+0.49}_{-0.53}$, where the first and second uncertainties are statistical and systematic, respectively.

(b) Fixed yield for the $B_s^0 \to c\bar{c}X$ component

We sum all the known branching fractions for $B_s^0 \to c\bar{c}X$ decays listed in particle data group (PDG) [1] and calculate the $\mathcal{B}(B_s^0 \to c\bar{c}X)$ to be $(5.73 \pm 0.22) \times 10^{-3}$. The percentage uncertainties associated with the number of $B_s^0\bar{B}_s^0$ mesons discussed in subsection 5.2.8 and $\mathcal{B}(B_s^0 \to c\bar{c}X)$ are $\binom{+10.30}{-10.74}\%$ and 3.84%, respectively. Further, accounting for the uncertainty on the identification and reconstruction of intermediate particles, we estimate the total systematic uncertainty of $\binom{+11.70}{-12.09}\%$ associated with an MC-based fixed background yield. The yield for $B_s^0 \to c\bar{c}X$ component is $4.33 \pm 2.08\ ^{+0.51}_{-0.52}$ events, where the first and second uncertainties are statistical and systematic, respectively.

5.2.10 Fit bias

The estimated fit bias in the signal pull extraction for an ensemble corresponding to the upper limit signal value is 0.055 ± 0.015, where the uncertainty is statistical only. It is worth mentioning that the signal pull is the ratio of the difference in the actual and fitted signal yield to the statistical uncertainty of the fitted signal yield. The systematic uncertainty associated with the fit bias is obtained by multiplying the pull bias of 0.055 and the width of the fitted signal yield distribution, as shown in Figure 4.12. We estimate the systematic uncertainty from bias to be +0.23 events.

5.2.11 Fixed parameters of the PDFs

As mentioned earlier, the signal PDF parameters, yields of $B_d^0 \to J/\psi\pi^0$ and $B_s^0 \to c\bar{c}X$ background PDFs, and the endpoint of the ARGUS functions are fixed to the MC estimates. Table 4.5 lists the fixed parameters and corresponding best-fit values. For an infinitely repeated parameter measurement, the actual value will likely be within the one-sigma interval around the mean of parameter estimate distribution. Therefore, the systematic uncertainty due to the uncertainty in the fixed parameter estimate is determined by varying the parameter value by the corresponding statistical uncertainty. Table 5.1 lists the signal yields by varying the parameter values by $\pm 1\sigma$ statistical uncertainty (except for the parameters marked with * and †). Systematic uncertainty due to the slight discrepancy in the simulated and actual data is evaluated by varying the mean and sigma by corresponding correction factors from the control sample. $M_{\rm bc}$ and $\Delta E'$ means are varied by ± 0.18 MeV/c^2 and ± 2.68 MeV, the square-rooted quadrature sum of correction factor and statistical uncertainty in the means. Systematics in widths is evaluated by smearing the σ with the corresponding fudge factor. Fractions $f_{B_s^{0*}\bar{B}_s^{0*}}$ and $f_{B_s^{0*}\bar{B}_s^{0}}$ are varied, accounting for the statistical uncertainties in measured values [37]. The systematic uncertainty due to the fixed yields for $B_d^0 \to J/\psi\pi^0$ and $B_s^0 \to c\bar{c}X$ PDFs are computed by varying the parameter estimates by ± 2.33 and ± 2.14 events, the quadratic sum of the corresponding statistical and systematic uncertainties, respectively. The deviation of the yields (ΔYield) from the central value of -0.01 events is determined independently for each parameter, estimating the associated systematic

uncertainty due to the fixed MC values. The uncertainties due to the fixed yields of $B_d^0 \to J/\psi\pi^0$ and $B_s^0 \to c\bar{c}X$ components are determined to be $^{+0.25}_{-0.31}$ and $^{+0.51}_{-0.69}$. We add the yield deviations in quadrature to evaluate the total uncertainty associated with PDF parameterization of $^{+0.67}_{-0.79}$ events.

Variable	$B_s^{0(*)}\bar{B}_s^{0(*)}$	Function	Parameter	Yield($+\sigma$)	Yield($-\sigma$)	ΔYield
M_{bc}	$B_s^{0*}\bar{B}_s^{0*}$	CB	μ^* (GeV/c^2)	-0.20 ± 3.10	0.20 ± 3.30	$^{+0.19}_{-0.21}$
			σ^* (GeV/c^2)	-0.20 ± 3.10		+0.19
			α	-0.05 ± 3.10	0.00 ± 3.20	$^{+0.04}_{-0.01}$
			n	-0.02 ± 3.20	0.10 ± 3.20	$^{+0.01}_{-0.11}$
			$f^{\dagger}_{B_s^{0*}\bar{B}_s^{0*}}$	0.00 ± 3.10	-0.03 ± 3.20	$^{+0.02}_{-0.01}$
	$B_s^{0*}\bar{B}_s^0$ or $B_s^0\bar{B}_s^{0*}$	Double-G with common mean	μ	-0.01 ± 3.20	-0.01 ± 3.20	$^{+0.00}_{-0.00}$
			σ (G$_1$) (GeV/c^2)	-0.01 ± 3.20	-0.01 ± 3.20	$^{+0.00}_{-0.00}$
			σ (G$_2$) (GeV/c^2)	-0.01 ± 3.20	-0.01 ± 3.20	$^{+0.00}_{-0.00}$
			fraction (G$_1$)	-0.01 ± 3.20	-0.01 ± 3.20	$^{+0.00}_{-0.00}$
			$f^{\dagger}_{B_s^{0*}\bar{B}_s^0}$	0.00 ± 3.20	-0.06 ± 3.10	$^{+0.05}_{-0.01}$
	$B_s^0\bar{B}_s^0$	Double-G with common mean	μ	-0.01 ± 3.20	-0.01 ± 3.20	$^{+0.00}_{-0.00}$
			σ (G$_1$) (GeV/c^2)	-0.01 ± 3.20	-0.01 ± 3.20	$^{+0.00}_{-0.00}$
			σ (G$_2$) (GeV/c^2)	-0.01 ± 3.20	-0.01 ± 3.20	$^{+0.00}_{-0.00}$
			fraction (G$_1$)	-0.01 ± 3.20	-0.01 ± 3.20	$^{+0.00}_{-0.00}$
	All	ARGUS	Endpoint (GeV/c^2)	0.00 ± 3.20	-0.05 ± 3.20	$^{+0.04}_{-0.01}$
$\Delta E'$	All	CB+G with common mean	μ^* (GeV)	-0.19 ± 3.20	0.20 ± 3.20	$^{+0.18}_{-0.21}$
			σ^* (CB) (GeV)	0.00 ± 3.10		-0.01
			α	-0.17 ± 3.10	0.20 ± 3.30	$^{+0.16}_{-0.21}$
			n	-0.06 ± 3.10	0.10 ± 3.20	$^{+0.05}_{-0.11}$
			σ^* (G) (GeV)	0.00 ± 3.20		-0.01
			fraction (CB)	0.00 ± 3.20	-0.03 ± 3.20	$^{+0.02}_{-0.01}$
Events corresponding to $B_d^0 \to J/\psi\pi^0$ PDF				-0.26 ± 3.10	0.30 ± 3.30	$^{+0.25}_{-0.31}$
Events corresponding to $B_s^0 \to c\bar{c}X$ PDF				-0.52 ± 3.10	0.60 ± 3.30	$^{+0.51}_{-0.61}$
Total systematic due to the fixed PDF parameters (events)						$^{+0.67}_{-0.79}$

Table 5.1: List of the parameters fixed to MC values to extract the $B_s^0 \to J/\psi\pi^0$ signals from the real data. Fixed values of the parameters marked with * and † are varied, accounting for the discrepancies in simulated and actual data using the control sample and experimentally measured uncertainties, respectively.

Further, the systematic uncertainties are categorized into two types: additive and multiplicative. Additive uncertainties reduce the significance of the observed signal peak and change the branching fraction; for example, uncertainties arise due to the fit procedure, which includes PDF parameterization and fit bias. In contrast, multiplicative uncertainties affect the branching fraction measurement through uncertainties in signal reconstruction efficiency, number of B_s^0 mesons, and $\mathcal{B}(J/\psi \to l^+l^-)$ and $\mathcal{B}(\pi^0 \to \gamma\gamma)$ measurements. Tables 5.2 and 5.3 list the various sources of the additive and multiplicative systematic uncertainties. Total systematic uncertainty

in each type is obtained by adding the individual uncertainties in quadrature.

Source	Uncertainty in Events
PDF Parametrization	$^{+0.67}_{-0.79}$
Fit Bias	$^{+0.23}_{-0.00}$
Total (quadratic sum)	$^{+0.71}_{-0.79}$

Table 5.2: Additive systematic uncertainties on $\mathcal{B}(B_s^0 \to J/\psi\pi^0)$.

Source	Uncertainty(%)
π^0 reconstruction	2.2
Tracking	2×0.35
Lepton-ID selection	2×2.25
MC statistics	0.32
Number of B_s^0 mesons	$^{+10.30}_{-10.74}$
$\mathcal{B}(J/\psi \to l^+l^-)$	0.77
$\mathcal{B}(\pi^0 \to \gamma\gamma)$	0.03
J/ψ mass-vertex fit $\chi^2 < 60$	2.25
Total (quadratic sum)	$^{+11.7}_{-12.1}$

Table 5.3: Multiplicative systematic uncertainties on $\mathcal{B}(B_s^0 \to J/\psi\pi^0)$.

5.3 Summary

In this chapter, we have discussed all the possible sources of additive and multiplicative systematic uncertainties in branching fraction measurement of $B_s^0 \to J/\psi\pi^0$. The values of all the systematic uncertainties are listed, and the total uncertainties are computed.

Chapter 6

Result and Conclusion

6.1 Introduction

This chapter presents the analysis results of the search for the decay $B_s^0 \to J/\psi\pi^0$ using all the collision data at $\Upsilon(5S)$ resonance from the Belle experiment. The dataset has a total integrated luminosity of 121.4 fb^{-1}. An upper limit (UL) on the branching fraction of $\mathcal{B}(B_s^0 \to J/\psi\pi^0)$ is reported as no signal is found.

6.2 Results

As we have seen in Section 4.7, the extracted signal yield from data fit is found to be -0.01 ± 3.2 events, where the uncertainty is statistical only. The negative yield is within the statistical uncertainty. In the absence of the physical value of signal yield, we calculate the UL on the branching fraction of $\mathcal{B}(B_s^0 \to J/\psi\pi^0)$ using the Bayesian approach [59]. The procedure pursued to estimate the UL on the signal yield in data is as follows:

1. We calculate the negative log of profile likelihood ratio, $-2\ln\left(\frac{\mathcal{L}_i}{\mathcal{L}_{\max}}\right)$, where $\mathcal{L}_i$ is the profile likelihood for a hypothesis of signal yield i and $\mathcal{L}_{\max}$ is the maximum likelihood of the data-fit. Figure 6.1(a) shows the distribution of the respective variable. Signal significance of the observed yield is given by $Z = \sqrt{-2\ln\left(\frac{\mathcal{L}_0}{\mathcal{L}_{\max}}\right)}$, where $\mathcal{L}_0$ is the likelihood of the fit with the background-only hypothesis. The signal significance is not reported as the yield is unphysical.

2. Further, the profile likelihood ratio is convoluted with a Gaussian function with a mean of zero and width equal to 0.8 events to incorporate the additive uncertainty in Table 5.2. The modified likelihood ratio is re-convoluted with a width proportional to the signals, where the total multiplicative systematic of 11.7%, shown in Table 5.3, is the proportionality constant. Figure 6.1(b) shows the distributions of profile likelihood and convoluted likelihood ratios.

3. We integrate the profile likelihood ratio ($\mathcal{L}_i/\mathcal{L}_{\max}$) over a range corresponding to physical values of the signal yield. The integration is performed from 0% to 90% of the total area under the likelihood curve to calculate a 90% confidence interval of the signal yield. The upper bound of the interval is estimated to be the 90% CL upper limit on the signal yield.

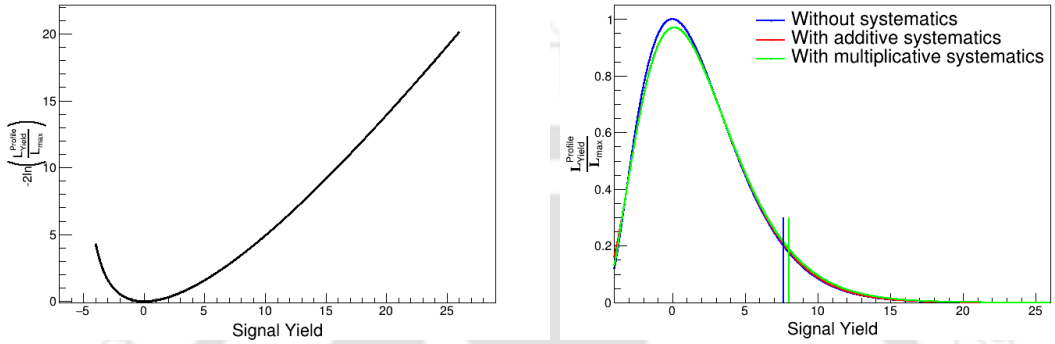

(a) (b)

Figure 6.1: (a) Two times the negative log of the profile likelihood ratio and (b) the profile likelihood ratio of the data fit for the range of signal hypotheses. The red (green) and blue colored distributions in (b) show the ratios with and without incorporating the additive (multiplicative) systematic uncertainties, whereas the vertical green and blue colored lines represent the corresponding 90% CL upper limits on the signal yields.

We estimate the UL on the signal yield of 8.03 and 7.64 events at 90% CL with and without incorporating the systematic uncertainties. It is worth mentioning that both additive and multiplicative uncertainties are included in the reported yield bound. The upper limit on the branching fraction is calculated as

$$\mathcal{B}(B_s^0 \to J/\psi\pi^0) = \frac{N_{\rm sig}^{\rm Yield}\ (\text{at } 90\%\ \text{CL})}{N_{B_s^0\bar{B}_s^0} \times \epsilon \times \mathcal{B}_{J/\psi} \times \mathcal{B}_{\pi^0}}, \tag{6.1}$$

where, $N_{\rm sig}^{\rm Yield}$ is the signal yield at 90% CL; $N_{B_s^0\bar{B}_s^0} = (18.16^{+1.87}_{-1.95}) \times 10^6$ is the number of $B_s^0\bar{B}_s^0$ mesons at $\Upsilon(5S)$ resonance; $\epsilon = 0.310 \pm 0.001$ is the signal reconstruction efficiency determined using the MC simulation; $\mathcal{B}_{J/\psi}$ is the sum of $\mathcal{B}(J/\psi \to \mu^+\mu^-)$ and $\mathcal{B}(J/\psi \to e^+e^-)$ [1]; and $\mathcal{B}_{\pi^0}$ is the branching fraction of $\pi^0 \to \gamma\gamma$ [1]. The resulting ULs with and without the systematics on $\mathcal{B}(B_s^0 \to J/\psi\pi^0)$ at 90% CL are summarized in Table 6.1.

The upper limit on the branching fraction $\mathcal{B}(B_s^0 \to J/\psi\pi^0)$ of 12.10×10^{-6} at 90% CL is an improvement by two orders of magnitude to the previous bound of 1.2×10^{-3} by L3 collaboration in 1997.

Branching fraction	UL at 90% CL
$\mathcal{B}(B_s^0 \to J/\psi\pi^0)$ without systematic	$< 11.51 \times 10^{-6}$
$\mathcal{B}(B_s^0 \to J/\psi\pi^0)$ with systematic	$< 12.10 \times 10^{-6}$

Table 6.1: Summary of the UL on $\mathcal{B}(B_s^0 \to J/\psi\pi^0)$ at 90% CL.

6.3 Summary and Conclusion

This thesis presents the search for the decay $B_s^0 \to J/\psi\pi^0$ at the Belle experiment. The analysis is performed using the 121.4 fb^{-1} of e^+e^- collision data at $\Upsilon(5S)$ resonance. We estimate a UL of 12.10×10^{-6} at 90% CL as no $B_s^0 \to J/\psi\pi^0$ signal is observed in the data-fit. The observed UL is an improvement by two orders of magnitude to the only existing upper bound by the L3 collaboration.

6.4 Outlook

As discussed in Chapter 1, the decays proceeding through the weak-annihilation topologies are predicted to be rare in the SM. The contributions of such amplitudes are assumed to have negligible counterparts in the theoretical computations. The decay $B_s^0 \to J/\psi\pi^0$ is supposed to be dominated by the $\eta - \pi^0$ mixing of $B_s^0 \to J/\psi\eta$ transition. The predicted branching fraction of $B_s^0 \to J/\psi\pi^0$ of order 4×10^{-6} is within the acceptable region of the measured UL. The precise measurement of this branching fraction can be performed at the Belle II experiment, a successor of the Belle experiment, which plans to collect approximately 5 ab^{-1} of data at $\Upsilon(5S)$ resonance in the near future. The LHCb collaboration may have difficulties in performing a similar search due to the limitations of isolating a single π^0 in the hadron calorimeter.

Appendix A

Decay File

Decay file for generating the $B_s^0 \to J/\psi\pi^0$ events. The sum of the branching fractions in a decay function, for example the `Decay Upsilon(5S)`, is normalized to unity.

```
Alias  MyB_s0        B_s0
Alias  MyB_s*0       B_s*0
Alias  Myanti-B_s0   anti-B_s0
Alias  Myanti-B_s*0  anti-B_s*0
Alias  MyJ/psi       J/psi
Alias  Mypi0         pi0

Decay Upsilon(5S)
0.057          MyB_s0       anti-B_s0          VSS;
0.0365         MyB_s*0      anti-B_s0          PHSP;
0.0365         MyB_s0       anti-B_s*0         PHSP;
0.870          MyB_s*0      anti-B_s*0         PHSP;

0.057          B_s0         Myanti-B_s0        VSS;
0.0365         B_s*0        Myanti-B_s0        PHSP;
0.0365         B_s0         Myanti-B_s*0       PHSP;
0.870          B_s*0        Myanti-B_s*0       PHSP;
Enddecay


Decay  MyB_s*0
1.0            MyB_s0       gamma              VSP_PWAVE;
Enddecay
```

```
Decay Myanti-B_s*0
1.0             Myanti-B_s0  gamma               VSP_PWAVE;
Enddecay


Decay MyB_s0
1.0             MyJ/psi      Mypi0                SVS;
Enddecay

Decay Myanti-B_s0
1.0             MyJ/psi      Mypi0                SVS;
Enddecay

#For the muon sector
Decay MyJ/psi
1.0             mu+          mu-                  PHOTOS      VLL;
Enddecay

#For the electron sector
Decay MyJ/psi
1.0             e+            e-                  PHOTOS      VLL;
Enddecay

Decay Mypi0
1.0             gamma        gamma                PHSP;
Enddecay

End
```

Appendix B

Probability Distribution Functions

B.1 Gaussian Distribution

A continuous random variable x will follow a Gaussian distribution if it obeys the function given by

$$f(x;\mu,\sigma) = \frac{1}{\sqrt{2\pi\sigma^2}} \exp\left(-\frac{(x-\mu)^2}{2\sigma^2}\right), \tag{B.1}$$

where μ and σ are the fixed parameters inferring the mean and standard deviation of the distribution for x.

B.2 Crystal Ball Function

The Crystal Ball (CB) function is a Gaussian distribution of a continuous random variable x with an asymmetric tail on either of the two sides; generally, a tail on the low side describes the frequency of the energy loss processes. The function is defined as

$$f(x;\mu,\sigma,n,\alpha) = N \begin{cases} \left(\frac{n}{|\alpha|}\right)^n \exp\left(\frac{-|\alpha|^2}{2}\right)\left(\frac{n}{|\alpha|} - |\alpha| - \frac{|x-\mu|}{\sigma}\right)^{-n}, & \text{if } \frac{x-\mu}{\sigma} \leq -\alpha \\ \exp\left(-\frac{(x-\mu)^2}{2\sigma^2}\right), & \text{otherwise.} \end{cases}, \tag{B.2}$$

where μ and σ are the mean and resolution of the Gaussian core, α is the threshold parameter in term of the σ, n is the power-law expansion parameter, and N is the normalization coefficient. The empirical form of the function was formulated by the Crystal Ball collaboration [65].

B.3 ARGUS function

The ARGUS function for a continuous random variable m is defined as

$$f(m; m_0, \xi) = \begin{cases} m\sqrt{1-\left(\frac{m}{m_0}\right)^2}\exp\left[\xi\left(1-\left(\frac{m}{m_0}\right)^2\right)\right], & \text{if } m < m_0 \\ 0, & \text{otherwise} \end{cases}, \tag{B.3}$$

where m_0 is the upper bound on the distribution of m and ξ is the curvature of the PDF. The function was first introduced by the ARGUS collaboration [66]. The ARGUS function is used significantly in the physics of B mesons to fit the invariant mass or $M_{\rm bc}$ distribution of the combinatorial background.

B.4 Chebychev Polynomial

The Chebychev polynomials [71] of the first kind ($T_n(x)$) are the solutions of the Chebychev differential equation given by

$$(1-x^2)\frac{d^2y}{dx^2} - x\frac{dy}{dx} + n^2 y = 0, \tag{B.4}$$

where $n = 0, 1, 2, \ldots$ are the integer numbers. The first few polynomials are as follows

$$T_0(x) = 1. \tag{B.5}$$
$$T_1(x) = x. \tag{B.6}$$
$$T_2(x) = 2x^2 - 1. \tag{B.7}$$
$$T_3(x) = 4x^3 - 3x. \tag{B.8}$$
$$T_4(x) = 8x^4 - 8x^2 + 1. \tag{B.9}$$
$$\vdots$$

All the polynomials can be determined recursively by

$$T_{n+1}(x) = 2xT_n(x) - T_{n-1}(x), \tag{B.10}$$

if any two consecutive polynomials are known. The Chebychev polynomials are orthogonal in the interval $x \in [-1, 1]$ and normalized that for all n, $T_n(1) = 1$. Any arbitrary polynomial of degree n can be written in terms of the Chebychev polynomials as

$$f(x; a_1, \ldots, a_n) = \frac{1}{N}\left[T_0(x) + \sum_{i=1}^{n} a_i T_i(x)\right], \tag{B.11}$$

where $T_i(x)$ is the $i^{\rm th}$ order Chebychev polynomial and a_i is the corresponding coefficient. Chebychev polynomials have better stability than ordinary polynomials due to the lower correlation between the coefficients [61].

Appendix C

Fit Results of the Background PDF components

Figures 4.5, 4.6, and 4.7 show the projections of background PDFs to large dedicated MC samples. This appendix presents the fit results of the background PDFs to six streams of MC data, as shown in Figure C.1. Selected candidates from the continuum and $B \to c\bar{c}X$ are fitted using the ARGUS and first-order Chebychev polynomial, whereas $B^0_d \to J/\psi\pi^0$ and $B^0_s \to c\bar{c}X$ are fitted using the histogram PDFs shown in Figures 4.6, and 4.7.

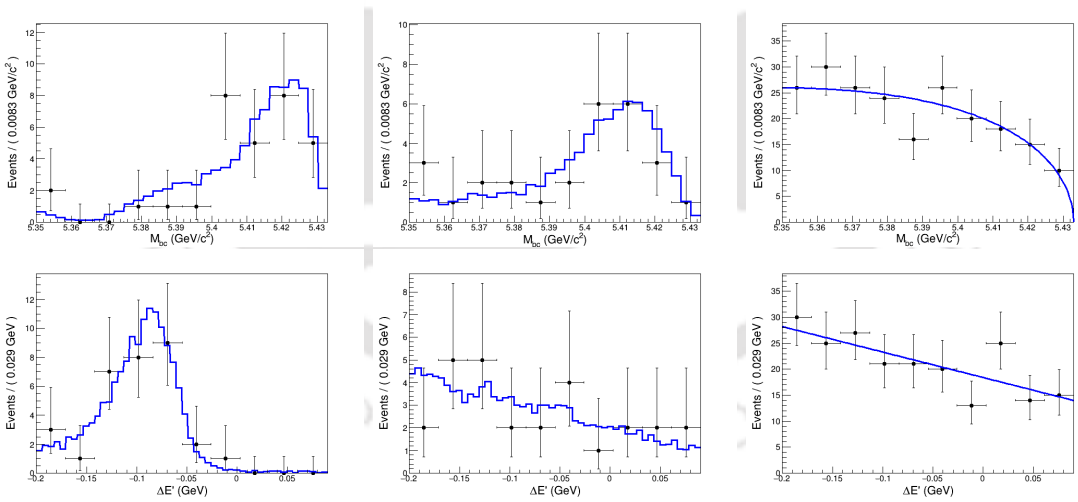

(a) (b) (c)

Figure C.1: Projections of the 2D fit to six streams of MC background data. The upper and lower distributions are of $M_{\rm bc}$ and $\Delta E'$. The fit results of $B^0_d \to J/\psi\pi^0$, $B^0_s \to c\bar{c}X$, and the continuum plus $B \to c\bar{c}X$ data are shown in columns (a), (b), and (c), respectively.

The background estimates from six streams of MC data are normalized to data luminosity, which is $\left(\frac{1}{6}\right)^{\rm th}$ of the given MC sample. The expected background for $B^0_d \to J/\psi\pi^0$, $B^0_s \to c\bar{c}X$, and the remaining are determined to be 5.17 ± 2.27,

4.33±2.08, and 34.67±5.89, respectively, where the uncertainties are statistical only determined considering that the expected events follow the Poisson distribution.

Appendix D

Ensemble Study: Signal Pull and Fitted Yield Distributions

Figures D.1 and D.2 show the distributions of signal pull and fitted signal yield extracted from the toy ensembles. The mean and width of the pull distributions are determined by fitting a Gaussian function in a range of approximately $\pm 2.5\sigma$ region around the no-bias case of the distribution. The average mean of the pull distributions is quantified as the fit bias associated with the fit model.

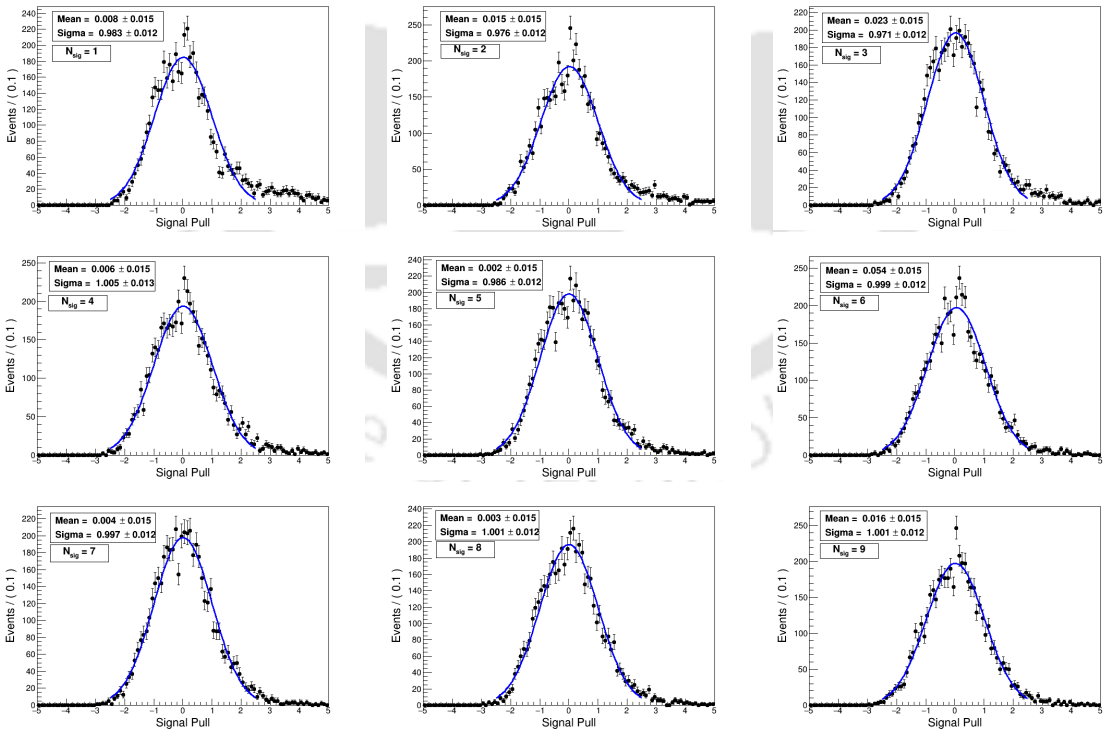

Figure D.1: Distributions of the signal pull. The blue-colored solid line represents the fitted Gaussian function. The text label in each distribution corresponds to a toy ensemble with a particular number of signal events.

Similarly, the signal yield distributions are fitted with a Gaussian function in a short range around the actual number of signal events. The long tail for distributions with fewer signals is attributed to the fitter instability due to low statistics of the toy data. A further insight is that we only have four free parameters to be determined by the maximum likelihood fit; The yields for signal and combinatorial background, the curvature of the ARGUS function, and the slope of the Chebychev polynomial. Toys for which the yields constitute the tail, the curvature is overestimated due to low statistics, and it is counterbalanced by the negatively large signal yields. This is evident from the scatter plots shown in Figure D.3. To show that this is purely a statistical effect, we performed the toy investigation with 200 background events. The fixed values of expected $B^0_d \to J/\psi\pi^0$ and $B^0_s \to c\bar{c}X$ backgrounds are normalized accordingly to 23 and 19 events, respectively. Figure D.4 shows the corresponding distributions. The signal yield and curvature converge to the expected values. The fitted signal yield and pull distributions from the ensembles with background statistics of 200 are shown in Figure D.5, where the distributions are perfectly Gaussian.

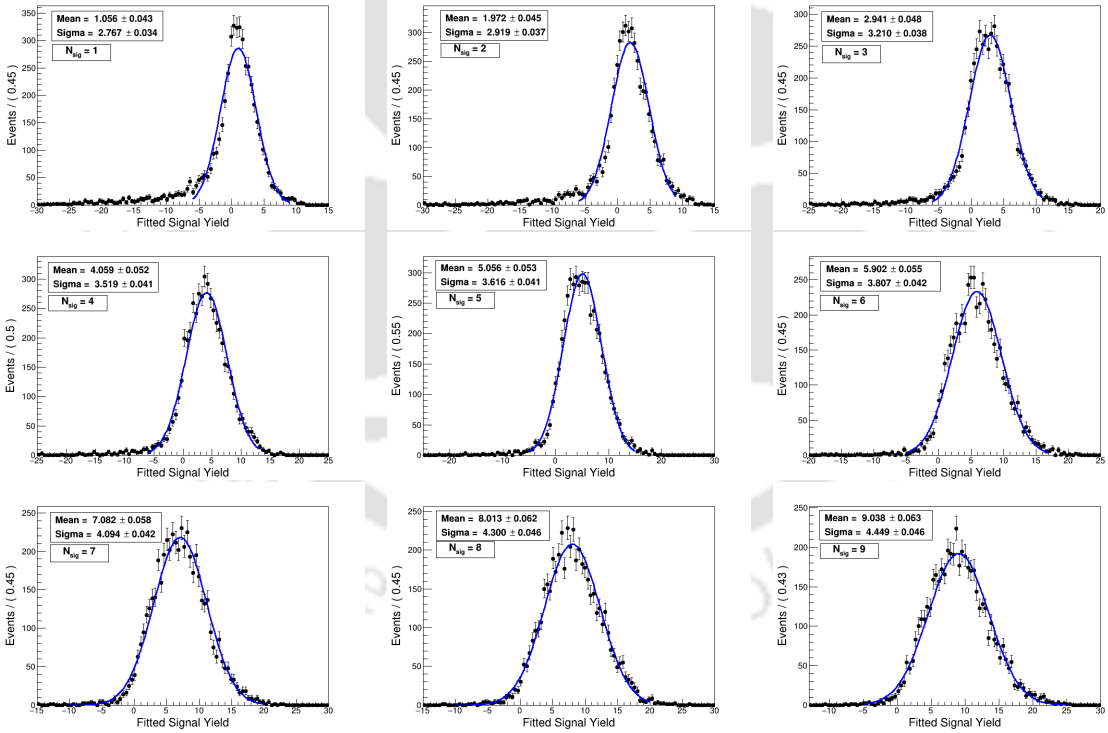

Figure D.2: Distributions of the fitted signal yield. The blue-colored solid line represents the fitted Gaussian function. The text label in each distribution corresponds to a toy ensemble with a particular number of signal events.

Contrary to this, the fitted yield for higher signals has no tail. The signal component of the PDF is fitted conveniently; consequently, the fluctuations in determining the curvature are highly suppressed. The statement is backed by the scattered plots shown in Figure D.6.

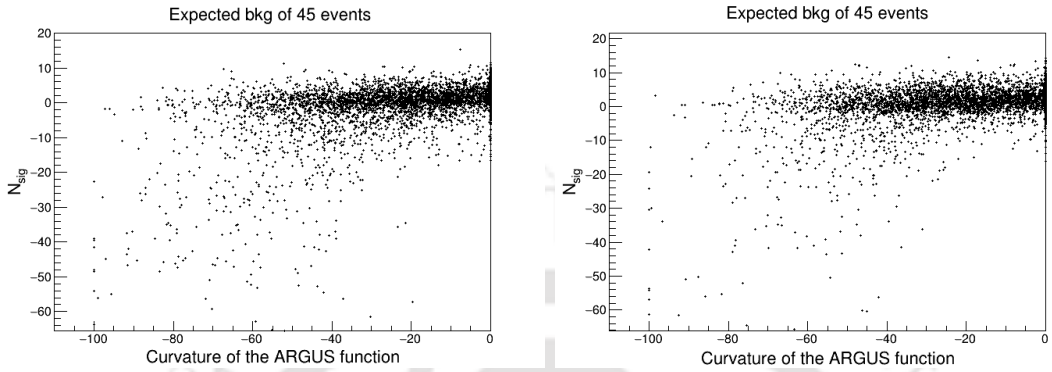

(a) (b)

Figure D.3: The fitted signal yield versus curvature of the ARGUS function extracted from the toy ensembles for (a) $N_{\text{sig}} = 1$ and (b) $N_{\text{sig}} = 2$. The expected background is considered to be 45 events.

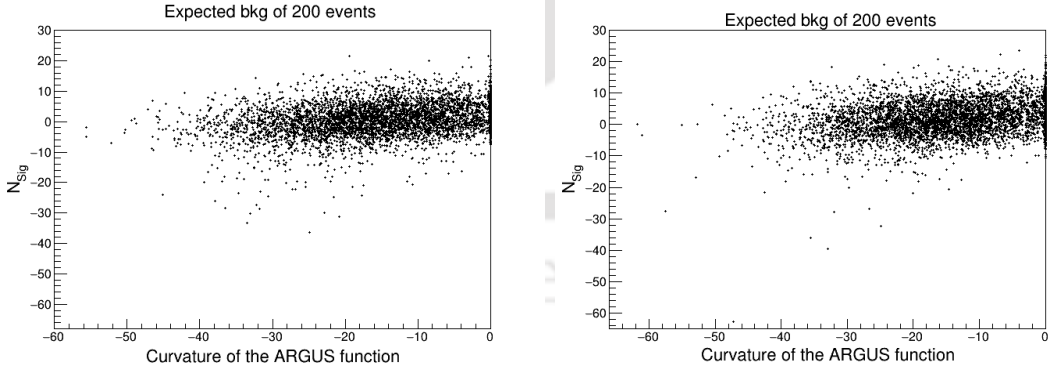

(a) (b)

Figure D.4: The fitted signal yield versus curvature of the ARGUS function extracted from the toy ensembles for (a) $N_{\text{sig}} = 1$ and (b) $N_{\text{sig}} = 2$. The expected background is considered to be 200 events.

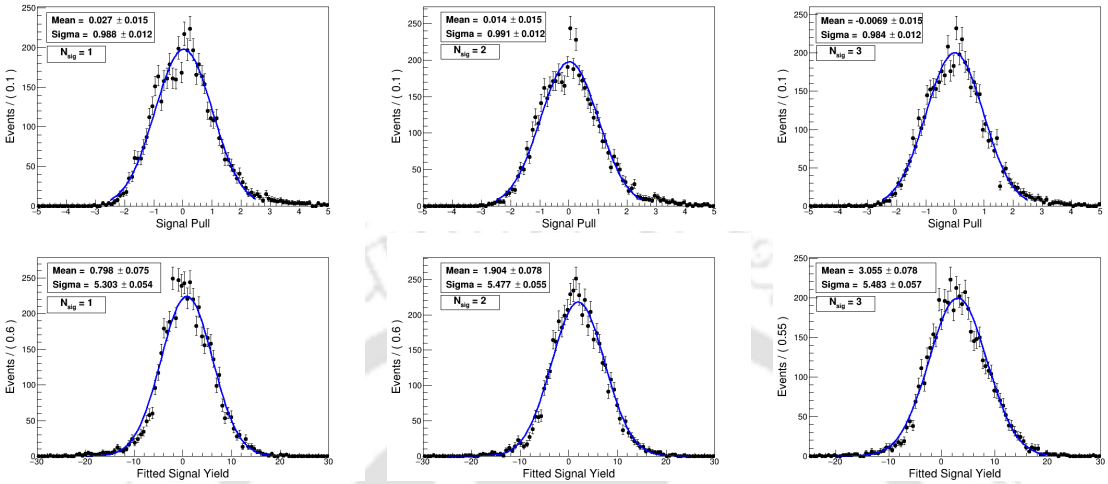

Figure D.5: Distributions of the signal pull (upper row) and fitted signal yield (lower row) extracted from the large ensembles corresponding to different assumptions of the signal events, as shown in text labels. The toy data under consideration has large background statistics of 200 events.

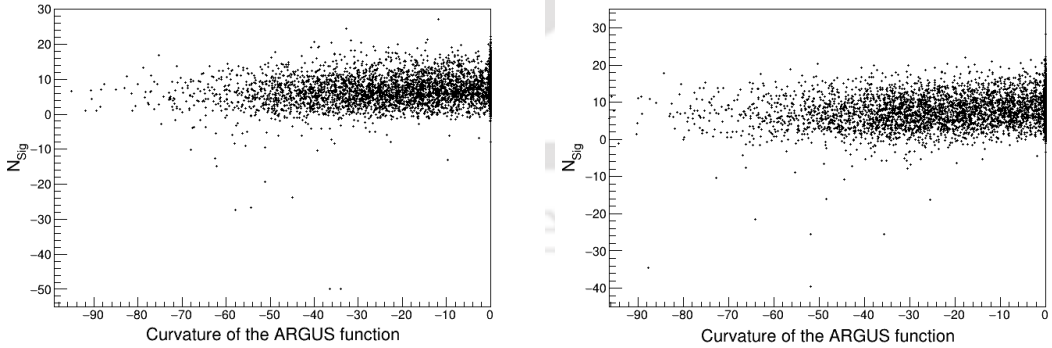

(a) (b)

Figure D.6: The fitted signal yield versus curvature of the ARGUS function extracted from the toy ensembles for (a) $N_{\text{sig}} = 7$ and (b) $N_{\text{sig}} = 8$. The expected background is considered to be 45 events.

Bibliography

[1] R. L. Workman *et al.*, "Review of Particle Physics," *PTEP*, vol. 2022, p. 083C01, 2022.

[2] A. Abashian *et al.*, "The Belle Detector," *Nucl. Instrum. Meth. A*, vol. 479, pp. 117–232, 2002.

[3] M. Thomson, *Modern particle physics*. New York: Cambridge University Press, 2013.

[4] G. L. Kane, *Modern Elementary Particle Physics*. Cambridge University Press, 2 2017.

[5] T. P. Cheng and L. F. Li, *Gauge Theory of Elementary Particle Physics*. Oxford, UK: Oxford University Press, 1984.

[6] L.-L. Chau and W.-Y. Keung, "Comments on the Parametrization of the Kobayashi-Maskawa Matrix," *Phys. Rev. Lett.*, vol. 53, p. 1802, 1984.

[7] L. Wolfenstein, "Parametrization of the Kobayashi-Maskawa Matrix," *Phys. Rev. Lett.*, vol. 51, p. 1945, 1983.

[8] A. J. Buras, M. E. Lautenbacher, and G. Ostermaier, "Waiting for the top quark mass, K+ —> pi+ neutrino anti-neutrino, B(s)0 - anti-B(s)0 mixing and CP asymmetries in B decays," *Phys. Rev. D*, vol. 50, pp. 3433–3446, 1994.

[9] J. Charles, A. Hocker, H. Lacker, S. Laplace, F. R. Le Diberder, J. Malcles, J. Ocariz, M. Pivk, and L. Roos, "CP violation and the CKM matrix: Assessing the impact of the asymmetric B factories," *Eur. Phys. J. C*, vol. 41, no. 1, pp. 1–131, 2005.

[10] S. L. Glashow, J. Iliopoulos, and L. Maiani, "Weak Interactions with Lepton-Hadron Symmetry," *Phys. Rev. D*, vol. 2, pp. 1285–1292, 1970.

[11] G. Buchalla, A. J. Buras, and M. E. Lautenbacher, "Weak decays beyond leading logarithms," *Rev. Mod. Phys.*, vol. 68, pp. 1125–1144, 1996.

[12] A. J. Buras, "Weak Hamiltonian, CP violation and rare decays," in *Les Houches Summer School in Theoretical Physics, Session 68: Probing the Standard Model of Particle Interactions*, pp. 281–539, 6 1998.

[13] A. J. Buras, "Theoretical review of B physics," *Nucl. Instrum. Meth. A*, vol. 368, pp. 1–20, 1995.

[14] C.-H. V. Chang and H.-n. Li, "Three - scale factorization theorem and effective field theory," *Phys. Rev. D*, vol. 55, pp. 5577–5580, 1997.

[15] T.-W. Yeh and H.-n. Li, "Factorization theorems, effective field theory, and nonleptonic heavy meson decays," *Phys. Rev. D*, vol. 56, pp. 1615–1631, 1997.

[16] A. Ali *et al.*, "Charmless non-leptonic B_s decays to PP, PV and VV final states in the pQCD approach," *Phys. Rev. D*, vol. 76, p. 074018, 2007.

[17] M. Beneke and M. Neubert, "QCD factorization for $B \to PP$ and $B \to PV$ decays," *Nucl. Phys. B*, vol. 675, pp. 333–415, 2003.

[18] J. Sun *et al.*, "Phenomenological analysis of charmless decays $B_s \to PP$, PV with QCD factorization," *Phys. Rev. D*, vol. 68, p. 054003, 2003.

[19] H. Y. Cheng and C. K. Chua, "QCD Factorization for Charmless Hadronic B_s Decays Revisited," *Phys. Rev. D*, vol. 80, p. 114026, 2009.

[20] H. Y. Cheng and C. K. Chua, "Revisiting Charmless Hadronic $B_{u,d}$ Decays in QCD Factorization," *Phys. Rev. D*, vol. 80, p. 114008, 2009.

[21] A. R. Williamson and J. Zupan, "Two body B decays with isosinglet final states in SCET," *Phys. Rev. D*, vol. 74, p. 014003, 2006. [Erratum: Phys.Rev.D 74, 03901 (2006)].

[22] M. Beneke, "Conceptual aspects of QCD factorization in hadronic B decays," *J. Phys. G*, vol. 27, pp. 1069–1080, 2001.

[23] M. B. Voloshin, "Charmonium," *Prog. Part. Nucl. Phys.*, vol. 61, pp. 455–511, 2008.

[24] Q. He *et al.*, "Observation of Upsilon(2S) —> eta Upsilon(1S) and search for related transitions," *Phys. Rev. Lett.*, vol. 101, p. 192001, 2008.

[25] M. Ablikim *et al.*, "Precision measurements of branching fractions for $\psi' \to \pi^0 J\psi$ and $\eta J\psi$," *Phys. Rev. D*, vol. 86, p. 092008, 2012.

[26] B. Pal *et al.*, "Measurement of the branching fraction and time-dependent CP asymmetry for $B^0 \to J/\psi\pi^0$ decays," *Phys. Rev.*, vol. D98, no. 11, p. 112008, 2018.

[27] S. Faller, M. Jung, R. Fleischer, and T. Mannel, "The Golden Modes B0 —> J/psi K(S,L) in the Era of Precision Flavour Physics," *Phys. Rev. D*, vol. 79, p. 014030, 2009.

[28] R. Aaij *et al.*, "Observation of the annihilation decay mode $B^0 \to K^+K^-$," *Phys. Rev. Lett.*, vol. 118, no. 8, p. 081801, 2017.

[29] S. Kurokawa and E. Kikutani, "Overview of the KEKB accelerators," *Nucl. Instrum. Meth.*, vol. A499, pp. 1–7, 2003.

[30] Y. Kimura, "Tristan: The Japanese Electron - Proton Colliding Beam Project," *Experientia*, vol. 40, p. 144, 1980.

[31] K. Akai *et al.*, "RF systems for the KEK B factory," *Nucl. Instrum. Meth. A*, vol. 499, pp. 45–65, 2003.

[32] H. Kichimi *et al.*, "KEKB Beam Collision Stability at the Picosecond Timing and Micron Position Resolution as observed with the Belle Detector," *JINST*, vol. 5, p. P03011, 2010.

[33] I. Abe *et al.*, "The KEKB injector linac," *Nucl. Instrum. Meth. A*, vol. 499, pp. 167–190, 2003.

[34] T. Abe *et al.*, "Achievements of KEKB," *PTEP*, vol. 2013, p. 03A001, 2013.

[35] R. B. Palmer, "Energy Scaling, Crab Crossing, and the Pair Problem," *eConf*, vol. C8806271, pp. 613–619, 1988.

[36] K. Oide and K. Yokoya, "The Crab Crossing Scheme for Storage Ring Colliders," *Phys. Rev. A*, vol. 40, pp. 315–316, 1989.

[37] S. Esen *et al.*, "Precise measurement of the branching fractions for $B_s \to D_s^{(*)+} D_s^{(*)-}$ and first measurement of the $D_s^{*+} D_s^{*-}$ polarization using e^+e^- collisions," *Phys. Rev. D*, vol. 87, no. 3, p. 031101, 2013.

[38] V. Zhukova *et al.*, "Measurement of the $e^+e^- \to B_s^0 \bar{B}_s^0 X$ cross section in the energy range from 10.63 to 11.02 GeV using inclusive D_s^+ and D^0 production," *JHEP*, vol. 08, p. 131, 2023.

[39] R. Abe *et al.*, "The new beampipe for the Belle experiment," *Nucl. Instrum. Meth. A*, vol. 535, pp. 558–561, 2004.

[40] Z. Natkaniec *et al.*, "Status of the Belle silicon vertex detector," *Nucl. Instrum. Meth. A*, vol. 560, pp. 1–4, 2006.

[41] R. Abe *et al.*, "BELLE/SVD2 status and performance," *Nucl. Instrum. Meth. A*, vol. 535, pp. 379–383, 2004.

[42] P. A. Cerenkov, "Visible radiation produced by electrons moving in a medium with velocities exceeding that of light," *Phys. Rev.*, vol. 52, pp. 378–379, 1937.

[43] K. Miyabayashi, "Belle electromagnetic calorimeter," *Nucl. Instrum. Meth. A*, vol. 494, pp. 298–302, 2002.

[44] R. Akhmetshin *et al.*, "Survey of the properties of BGO crystals for the extreme forward calorimeter at BELLE," *Nucl. Instrum. Meth. A*, vol. 455, pp. 324–328, 2000.

[45] A. Abashian *et al.*, "The K(L) / mu detector subsystem for the BELLE experiment at the KEK B factory," *Nucl. Instrum. Meth. A*, vol. 449, pp. 112–124, 2000.

[46] Y. Ushiroda, A. Mohapatra, H. Sakamoto, Y. Sakai, M. Nakao, Q. An, and Y. F. Wang, "Development of the central trigger system for the BELLE detector at the KEK B factory," *Nucl. Instrum. Meth. A*, vol. 438, pp. 460–471, 1999.

[47] T. Ziegler *et al.*, "The Belle trigger system with the new silicon vertex detector SVD2," *IEEE Trans. Nucl. Sci.*, vol. 51, pp. 1852–1856, 2004.

[48] M. Hanagaki *et al.*, "Level 4 Software Trigger at Belle," *Belle Internal Note 299*.

[49] S. Nagayama, "PANTHER Users guide, version 3.0," 1997.

[50] S. Nagayama, "Panther User's Manual, Reference manual, and Primer," *Belle Internal Note 130, 131, and 132*.

[51] R. Itoh, "BASF - BELLE AnalysiS Framework," in *9th International Conference on Computing in High-Energy and Nuclear Physics*, 4 1997.

[52] D. J. Lange, "The evtgen particle decay simulation package," *Nuclear Instruments and Methods in Physics Research Section A: Accelerators, Spectrometers, Detectors and Associated Equipment*, vol. 462, no. 1-2, pp. 152–155, 2001.

[53] S. Agostinelli, J. Allison, K. a. Amako, J. Apostolakis, H. Araujo, P. Arce, M. Asai, D. Axen, S. Banerjee, G. . Barrand, *et al.*, "Geant4—a simulation toolkit," *Nuclear instruments and methods in physics research section A: Accelerators, Spectrometers, Detectors and Associated Equipment*, vol. 506, no. 3, pp. 250–303, 2003.

[54] K. Hanagaki, H. Kakuno, H. Ikeda, T. Iijima, and T. Tsukamoto, "Electron identification in Belle," *Nucl. Instrum. Meth. A*, vol. 485, pp. 490–503, 2002.

[55] A. Abashian *et al.*, "Muon identification in the Belle experiment at KEKB," *Nucl. Instrum. Meth. A*, vol. 491, pp. 69–82, 2002.

[56] G. C. Fox and S. Wolfram, "Observables for the analysis of event shapes in e^+e^- annihilation and other processes," *Phys. Rev. Lett.*, vol. 41, pp. 1581–1585, Dec 1978.

[57] H. Cramér, "Mathematical methods of statistics, 1946," *Department of Mathematical SU*, 1946.

[58] C. R. Rao, "Information and the accuracy attainable in the estimation of statistical parameters," *Reson. J. Sci. Educ*, vol. 20, pp. 78–90, 1945.

[59] L. Lista, *Statistical Methods for Data Analysis in Particle Physics*, vol. 909. Springer, 2016.

[60] G. Cowan, *Statistical data analysis*. 1998.

[61] W. Verkerke and D. P. Kirkby, "The RooFit toolkit for data modeling," *eConf*, vol. C0303241, p. MOLT007, 2003.

[62] R. Brun and F. Rademakers, "ROOT: An object oriented data analysis framework," *Nucl. Instrum. Meth. A*, vol. 389, pp. 81–86, 1997.

[63] F. James, "MINUIT Function Minimization and Error Analysis: Reference Manual Version 94.1," 1994.

[64] F. James and M. Winkler, "MINUIT User's Guide," 6 2004.

[65] T. Skwarnicki, *A study of the radiative CASCADE transitions between the Upsilon-Prime and Upsilon resonances*. PhD thesis, Cracow, INP, 1986.

[66] H. Albrecht *et al.*, "Search for Hadronic $b \to u$ Decays," *Phys. Lett. B*, vol. 241, pp. 278–282, 1990.

[67] B. Bhuyan, "High P_t Tracking Efficiency Using Partially Reconstructed D^* Decays," *Belle Internal Note, BN 1165*.

[68] L. Hinz, "Lepton ID efficiency correction and systematic error," *Belle Internal Note, BN 954*.

[69] *https://belle.kek.jp/group/pid_joint/*.

[70] S. Ryu, "Study of π^0 efficiency using $\tau^- \to \pi^0\pi^-\nu_\tau$," *Belle Internal Note, BN 1224*.

[71] G. B. Arfken, F. E. Harris, and H. J. Weber, *Mathematical Methods for Physicists*. 2012.